LUDWIG-MAXIMILANS-UNIVERSITÄT

MASTER THESIS

Investigation of the Synchronized Particle Motion During Mode-Coupling Instability

Author:
Michael Haslauer

Supervisors:
Prof. Dr. Gregor Morfill
Dr. Christoph Räth

Munich, October 3, 2016

LUDWIG-MAXIMILANS-UNIVERSITÄT

MASTER ARBEIT

Untersuchung der synchronisierten Teilchenbewegung während der Mode-Coupling Instabilität

Autor:
Michael Haslauer

Betreuer:
Prof. Dr. Gregor Morfill
Dr. Christoph Räth

München den 3.Oktober 2016

Contents

Chapter 1

Introduction

Complex or dusty plasmas are low-temperature plasmas containing microparticles in addition to ions, electrons and neutral gas atoms of a plasma [29]. These microparticles are highly charged, since they collect up to 10^5 electron charges on their surface. Thus the microparticles show a strong Columb interaction. Under certain conditions these systems of strongly coupled microparticles can form so called *plasma crystals*[30]. For experiments under gravity these plasma crystals are 2 dimensional hexagonal crystalline structures formed by the mircorparticles. Such plasma crystals show a plasma specific melting mechanism called *mode-coupling instability* or MCI [13]. This MCI is a consequence of the effective "nonreciprocal" interactions of the microparticles. Nonreciprocal means that Newton's third law "actio = reactio" is violated if focusing on the microparticles. This is possible because the effective interactions of the microparticles are mediated by a nonequilibrium environment of flowing plasma ions [14].
In 2014 the observation of synchronized particle motion during such a mode-coupling instability induced melting of a 2 dimensional plasma crystal was reported [7]. Synchronization of periodic or oscillatory subsystems is a widespread phenomenon with examples in biology [8], neuroscience [27] , chemistry [16] and physics like frequency locked Josephson arrays [32], pedestrians on a bridge locking their gait [28] or the theoretically well described synchronization of metronomes[23, 31, 20]. What all these examples have in common is that they are somehow connected to the synchronization theory of nonlinear limit cycle oscillators proposed by Y.Kuramoto in 1984 [17]. Thus also the synchronization observed during the mode-coupling instability was assumed to be an example of such nonlinear synchronization since complex plasmas are strongly coupled nonlinear systems. This is however not the case as will be shown in this thesis. Instead the synchronization during MCI can be understood as purely linear phenomenon. As will be shown nonreciprocal interactions of the microparticles provide some mechanism of dominance causing the system to show synchronized motion. For reciprocal interaction this is not possible.

The structure of this thesis is the following.
In Chapter 2 the used model for the description of the plasma crystal and further definitions are presented. Special attention will be put on the impact of the effective nonreciprocal interactions on wave mode theory.
In Chapter 3 the mode-coupling instability or MCI is presented, since it provides the mechanism responsible for the observed synchronization.
In Chapter 4 the observed synchronization is investigated in detail. First the known facts are recapitulated. Afterwards it is shown that the synchronization phenomenon is completely captured by a linear version of the interaction forces. Finally it will be shown that all aspects of the synchronization can be explained in quantitative manner using the linear theory of the plasma crystal.

Chapter 2

Model System and Definitions

2.1 The Model System

For analytic and numeric proposes 2 dimensional plasma crystals are usually modeled by a so called *Yukawa/point-wake model*[26] or *point-like wake model* as it will be termed during this thesis. Since the synchronization process of interest was captured correctly by simulations [19] based on this *point-like wake model*, for this thesis it is sufficient to restrict the description on this model.

2.1.1 Point-Like Wake Model

Complex or dusty plasmas are weakly ionized gases containing micron-sized dust grains (e.g. for the experiments where the synchronization was observed melanin-formaldehyde particles with a diameter of approx. $10\mu m$ where used). After injection of the dust grains into the plasma they acquire a negative equilibrium charge due to absorption of the surrounding electrons and ions[25]. If building a 2D plasma crystal the micro-particles are confined in the so called *sheath* region, short distanced above a flat radio-frequency electrode where the averaged electric field is strong enough to compensate for gravity[25]. The same electric field levitating the negative charged micro particles against gravity naturally induces a strong flow of the positive ions into direction of gravity. Surrounded by this flow the micro particles act similar to lenses focusing the ion downstream in a close region below the particle. This effect results in a notable polarization of the ion cloud surrounding the dust particles and is often referred to as *plasma wake*[21]. The most common and easiest way to model this polarization is to add a point-like positive charge q at a fixed distance δ below the dust particle. In this picture the particle-particle interaction can be expressed as superposition of the particle-particle and particle-wake interaction. Both can be modeled by spherically symmetric Yukawa (Debey-Hückel) potentials with an effective screening length λ. Such that the potential of particle i moving in the field of particle j is given by [13]

$$\phi(\mathbf{r}_{ji}) = \frac{1}{4\pi\epsilon_0}\frac{Q}{r_{ji}}\exp\left(-\frac{r_{ji}}{\lambda}\right) + \frac{1}{4\pi\epsilon_0}\frac{q}{r_{wji}}\exp\left(-\frac{r_{wji}}{\lambda}\right) \tag{2.1}$$

and the corresponding force exerted on particle i from particle j is given by

$$\begin{aligned}\mathbf{F}(\mathbf{r}_{ji}) &= -Q\nabla_{\mathbf{r_{ji}}}\phi(\mathbf{r}_{ji}) = -Q\nabla_{\mathbf{r_{ji}}}\phi(\mathbf{r}_{ji}) \\ &= \frac{1}{4\pi\epsilon_0}\frac{Q^2}{r_{ji}^3}\,\exp\left(-\frac{r_{ji}}{\lambda}\right)\left(1+\frac{r_{ji}}{\lambda}\right)\mathbf{r}_{ji} + \frac{1}{4\pi\epsilon_0}\frac{qQ}{r_{wji}^3}\,\exp\left(-\frac{r_{wji}}{\lambda}\right)\left(1+\frac{r_{wji}}{\lambda}\right)\mathbf{r}_{wji}\end{aligned} \tag{2.2}$$

Where $Q<0$ is the grain particle charge, $q>0$, $q<|Q|$ the charge of the plasma wake,ϵ_0 is the vacuum permittivity, λ is the screening length of the Yukawa potential, $\mathbf{r}_{ji}=\mathbf{x}_i-\mathbf{x}_j$ is the vector pointing from dust particle j at absolute position $\mathbf{x}_j$ towards dust particle i at absolute position $\mathbf{x}_j$, $\mathbf{r}_{wji}=\mathbf{r}_{ji}+\delta\mathbf{e}_z$ is the vector pointing from the wake-position of particle j towards the dust particle i and r_{ji}, r_{wji} denote the modulus or length of $\mathbf{r}_{ji}$, $\mathbf{r}_{wji}$.

The force (Eq. 2.2) can be expressed in a more convenient way by defining

$$\mathbf{F}(\mathbf{r}_{ji}) = Qf(r_{ji})\mathbf{r}_{ji} + qf(r_{wji})\mathbf{r}_{wji}\,,\ \text{where}\ f(r)=\frac{1}{4\pi\epsilon_0}\frac{Q}{r^3}\exp\left(-\frac{r}{\lambda}\right)\left(1+\frac{r}{\lambda}\right) \tag{2.3}$$

It should be mentioned that within this "effective" model there is no interaction of the dust particle with it's own wake. Nevertheless it has proven to be a correct approximation if describing a 2 dimensional plasma crystal[13]. In consequence the interaction is non-reciprocal i.e. $-\mathbf{F}(\mathbf{r}_{ji}) \neq \mathbf{F}(-\mathbf{r}_{ji}) = \mathbf{F}(\mathbf{r}_{ij})$. Hence the force exerted on particle j from particle i is not as usual for reciprocal forces given by $-Q\nabla_{\mathbf{x_j}}\phi(\mathbf{r}_{ji})$ instead we have $\mathbf{F}_{ij} = -Q\nabla_{\mathbf{x_j}}\phi(-\mathbf{r}_{ji})$. This issue of non-reciprocal interactions and resulting consequences are addressed in the next part Sec. 2.1.2.

2.1.2 Non-Reciprocity and Consequences

As already mentioned within the point-like wake model the interaction between two particles is non-reciprocal, what means that Newton's third law *"actio = reactio"* is not valid anymore. Of course, Newton's third law is still valid for the whole particle plus environment system if each ion and electron is taken into account. However since our environment is representing a non-equilibrium state (flowing downwards) after integrating out the microscopic degrees of freedom the "action = reactio" symmetry can be broken for the effective interaction force describing the dust particle interaction on mesoscopic scale [14].

Violated Energy Conservation

A direct consequence of the non-reciprocal interaction force (Eq. 2.2) is that the energy of the system is not necessarily conserved. In the first moment it might be confusing that the interaction force can nevertheless be expressed as negative gradient of the potential

Eq. 2.1. Since this is generally a feature of conservative[1] forces this seems to be inconsistent, however it is not. The reason is that the potential Eq. 2.1 only describes the motion of particle i in the fixed field of particle j. Therefore as long as particle j is somehow fixed the motion of particle i is conservative. However as far as both particles move it is not possible to define a combined potential and the motion of the system becomes non-conservative. In the following this is exemplified for the case of two interacting particles.

Given two particles with position vectors $\mathbf{x_1}$, $\mathbf{x_2}$, masses m, and a distance defined by $\mathbf{r} = \mathbf{x_1} - \mathbf{x_2}$. The interaction force shall be defined by $\mathbf{F}(\mathbf{y})$, such that the force acting on particle 1 is given by $\mathbf{F_{21}}(\mathbf{x_1} - \mathbf{x_2}) = \mathbf{F}(\mathbf{r})$ and the force acting on particle 2 by $\mathbf{F_{12}}(\mathbf{x_2} - \mathbf{x_1}) = \mathbf{F}(-\mathbf{r})$. Further the force $\mathbf{F}(\mathbf{y})$ is assumed to be conservative i.e. $\nabla_\mathbf{y} \times \mathbf{F}(\mathbf{y}) = 0$, what implies[2] that there is a scalar potential $U^{pot}(\mathbf{y})$ such that $-\nabla_\mathbf{y} U^{pot}(\mathbf{y}) = \mathbf{F}(\mathbf{y})$.

Inserting now for particle 1, $\mathbf{y} = \mathbf{r} \rightarrow \nabla_\mathbf{y} = \nabla_\mathbf{r}$ and for particle 2, $\mathbf{y} = -\mathbf{r} \rightarrow \nabla_\mathbf{y} = -\nabla_\mathbf{r}$ one gets

$$-\nabla_\mathbf{r} U^{pot}(\mathbf{r}) = \mathbf{F}(\mathbf{r}), \qquad \nabla_\mathbf{r} U^{pot}(-\mathbf{r}) = \mathbf{F}(-\mathbf{r}) \tag{2.4}$$

For clarification of notation it may be mentioned that $\nabla_\mathbf{r} U^{pot}(-\mathbf{r}) = -\nabla_\mathbf{r} U^{pot}(\mathbf{r})|_{\mathbf{r}=-\mathbf{r}}$. In case of reciprocal interactions, i.e. $-\mathbf{F}(\mathbf{r}) = \mathbf{F}(-\mathbf{r})$, one has therefore

$$\nabla_\mathbf{r} U^{pot}(\mathbf{r}) = \nabla_\mathbf{r} U^{pot}(-\mathbf{r}) \tag{2.5}$$

whereas for the case of non-reciprocal interaction, i.e. $-\mathbf{F}(\mathbf{r}) \neq \mathbf{F}(-\mathbf{r})$, this is not true

$$\nabla_\mathbf{r} U^{pot}(\mathbf{r}) \neq \nabla_\mathbf{r} U^{pot}(-\mathbf{r}) \tag{2.6}$$

Calculating now the time derivative[3] of the total kinetic energy $T_1 + T_2$ where $T_i = \frac{m\dot{\mathbf{x}}_\mathbf{i}^2}{2}$ one gets by using Eq. 2.4

$$\dot{T}_1 + \dot{T}_2 = \mathbf{F}(\mathbf{r})\dot{\mathbf{x}}_\mathbf{1} + \mathbf{F}(-\mathbf{r})\dot{\mathbf{x}}_\mathbf{2} = -\nabla_\mathbf{r} U^{pot}(\mathbf{r})\dot{\mathbf{x}}_\mathbf{1} + \nabla_\mathbf{r} U^{pot}(-\mathbf{r})\dot{\mathbf{x}}_\mathbf{2} \tag{2.7}$$

Only one moving particle: Without loss of generality one cas assume particle 1 is moving while particle 2 is fixed. In this case we have $\dot{T}_2 = 0$, $\dot{\mathbf{x}}_\mathbf{2} = 0$ and $\dot{\mathbf{r}} = \dot{\mathbf{x}}_\mathbf{1}$ such that Eq. 2.7 gives

$$\dot{T}_1 = -\nabla_\mathbf{r} U^{pot}(\mathbf{r})\dot{\mathbf{x}}_\mathbf{1} = -\nabla_\mathbf{r} U^{pot}(\mathbf{r})\dot{\mathbf{r}} = -\dot{U}^{pot}(\mathbf{r}) \tag{2.8}$$

and therefore one can define the total energy $E_1 = T_1 + U^{pot}(\mathbf{r})$ which is conserved.

$$\dot{E}_1 = \dot{T}_1 + \dot{U}^{pot}(\mathbf{r}) = 0 \rightarrow E_1 = \text{const.} \tag{2.9}$$

[1] Conservative forces are forces where the force field can be expressed as negative gradient of a scalar potential U^{pot} which has units of energy. In this case the work done on a closed orbit is always zero and the energy of the system is constant or conserved, i.e. $E = E^{kin} + U^{pot} = \text{const.}$[9]

[2] $\nabla \times \mathbf{F} = 0$ is a necessary and sufficient criterion for the existence of a scalar potential U^{pot} such that the vector field $\mathbf{F}$ can be expressed as $-\nabla U^{pot} = \mathbf{F}$.[9]

[3] In classical mechanics the time derivative of the kinetic energy is always given by $\dot{T} = \mathbf{F}\dot{\mathbf{x}}$. This can be seen by multiplying the equations of motion by the velocity $\dot{\mathbf{x}}$: $(\mathbf{F})\,\dot{\mathbf{x}} = (m\ddot{\mathbf{x}})\,\dot{\mathbf{x}} = \frac{d}{dt}(\frac{1}{2}m\dot{\mathbf{x}}^2) = \dot{T}$.

This result is always true, even for the case of non-reciprocal interaction.

Both particles moving: The situation is however different if both particles are moving. In this case both particles contribute in Eq. 2.7 and one has to distinguish the reciprocal and non-reciprocal case.

For *reciprocal interactions* we can insert Eq. 2.5 ($\nabla_{\mathbf{r}} U^{pot}(\mathbf{r}) = \nabla_{\mathbf{r}} U^{pot}(-\mathbf{r})$) into Eq. 2.7 and get

$$\dot{T}_1 + \dot{T}_2 = -\nabla_{\mathbf{r}} U^{pot}(\mathbf{r})(\dot{\mathbf{x}}_\mathbf{1} - \dot{\mathbf{x}}_\mathbf{2}) = -\nabla_{\mathbf{r}} U^{pot}(\mathbf{r})\dot{\mathbf{r}} = -\dot{U}^{pot} \tag{2.10}$$

and therefor the total Energy $E = T_1 + T_2 + U^{pot}(\mathbf{r}) = \text{const}$ is conserved.

In contrast for *non-reciprocal interactions* this simplification is not possible because of Eq. 2.6. However it is possible to decompose the interaction into a reciprocal and non-reciprocal part according to

$$\nabla_{\mathbf{r}} U^{pot}(-\mathbf{r}) = \nabla_{\mathbf{r}} U^{pot}(\mathbf{r}) + \boldsymbol{\gamma}(\mathbf{r}) \tag{2.11}$$

where the non-reciprocal part is defined as

$$\boldsymbol{\gamma}(\mathbf{r}) = \nabla_{\mathbf{r}} U^{pot}(-\mathbf{r}) - \nabla_{\mathbf{r}} U^{pot}(\mathbf{r}) = \mathbf{F}(-\mathbf{r}) + \mathbf{F}(\mathbf{r}) \tag{2.12}$$

which is clearly zero for reciprocal interactions. Using this definition Eq. 2.7 becomes after some rearrangement, similar as done for the other cases, the following relation

$$\dot{T}_1 + \dot{T}_2 + \dot{U}^{pot} = \boldsymbol{\gamma}(\mathbf{r})\dot{\mathbf{x}}_\mathbf{2} \tag{2.13}$$

For closed trajectories one therefore has

$$\oint dt(\dot{T}_1 + \dot{T}_2) + \cancelto{0}{\oint dt\dot{U}^{pot}} = \oint dt\boldsymbol{\gamma}(\mathbf{r})\dot{\mathbf{x}}_\mathbf{2} \;\rightarrow\; \Delta T_1 + \Delta T_2 = \oint \mathbf{dx_2}\boldsymbol{\gamma}(\mathbf{r}) \tag{2.14}$$

This shows clearly that the energy of the system is not necessarily conserved for non-reciprocal interactions. Even on closed trajectories the work done by the particle with respect to the non-reciprocal part of the interaction force may be positive or negative.

2.1.3 Linearization of the Point-Like Wake Model

At some points it will be necessary to use a linearized version of the point-like wake model with respect to an equilibrium distance $\mathbf{R}_{ji} = \mathbf{X}_i - \mathbf{X}_j$ of the two particles i and j. Assuming small deviations $\mathbf{d}_i$ and $\mathbf{d}_j$ from their equilibrium positions $\mathbf{X}_i$ and $\mathbf{X}_j$ such that the current positions are given by $\mathbf{x}_i = \mathbf{X}_i + \mathbf{d}_i$ and $\mathbf{x}_i = \mathbf{X}_j + \mathbf{d}_j$ the force caused by particle j acting on particle i can be approximated by its first order multivariate Taylor expansion

$$\mathbf{F}(\mathbf{r}_{ji}) = Qf(r_{ji})\mathbf{r}_{ji} + qf(r_{wji})\mathbf{r}_{wji} \approx \mathbf{J}(\mathbf{R}_{ji})(\mathbf{d}_i - \mathbf{d}_j) \tag{2.15}$$

where $\mathbf{J}(\mathbf{R}_{ji})$ is the Jacobian matrix of $\mathbf{F}(\mathbf{r}_{ji})$ evaluated at $\mathbf{R}_{ji}$ and $f(r)$ is given by

$$f(r) = \frac{1}{4\pi\epsilon_0}\frac{Q}{r^3}\exp\left(-\frac{r}{\lambda}\right)\left(1+\frac{r}{\lambda}\right) \tag{2.16}$$

$Q < 0$ is the grain particle charge, $q > 0$, $q < |Q|$ the charge of the plasma wake,ϵ_0 is the vacuum permittivity, λ is the screening length of the Yukawa potential, $\mathbf{r}_{ji} = \mathbf{x}_i - \mathbf{x}_j$ is the vector pointing from dust particle j at absolute position $\mathbf{x}_j$ towards dust particle i at absolute position $\mathbf{x}_j$, $\mathbf{r}_{wji} = \mathbf{r}_{ji} + \delta\mathbf{e}_z$ is the vector pointing from the wake-position of particle j towards the dust particle i and r_{ji}, r_{wji} denote the modulus or length of $\mathbf{r}_{ji}$, $\mathbf{r}_{wji}$.

In general the elements of the Jacobian matrix are given by $J_{lm}(\mathbf{R}_{ji}) = dF_{x_l}(\mathbf{R}_{ji})/dx_m$ [1] for $l, m = 1, 2, 3$ and $(x_1, x_2, x_3) = (x, y, z)$. In order to find a convenient formulation of the Jacobian matrix it is helpfull to define the three functions $a(\mathbf{r})$, $b(\mathbf{r})$ and $c(\mathbf{r})$ by

$$a(\mathbf{r}) = h_1(\mathbf{r}) + \frac{q}{Q}h_1(\mathbf{r}_w), \quad b(\mathbf{r}) = h_2(\mathbf{r}) + \frac{q}{Q}h_2(\mathbf{r}_w), \quad c(\mathbf{r}) = \frac{q}{Q}h_2(\mathbf{r}_w) \tag{2.17}$$

where

$$\begin{aligned} h_1(\mathbf{r}) &= \left(\frac{\lambda}{r}\right)^3 \exp\left(-\frac{\lambda}{r}\right)\left(1+\frac{r}{\lambda}\right) \\ h_2(\mathbf{r}) &= -\left(\frac{\lambda}{r}\right)^3 \exp\left(-\frac{\lambda}{r}\right)\left[\left(\frac{r}{\lambda}\right)^2 + 3\left(1+\frac{r}{\lambda}\right)\right]\frac{1}{r^2} \end{aligned} \tag{2.18}$$

If further writing $\mathbf{R}$ in place of $\mathbf{R}_{ji}$ and a, b, c instead of $a(\mathbf{R}), b(\mathbf{R}), c(\mathbf{R})$ to avoid a confusing notation, the elements of the Jacobian matrix are given by

$$\begin{aligned} &\frac{dF_x}{dx} = \frac{Q^2}{\lambda^3}(a + R_x^2 b)\,, && \frac{dF_x}{dy} = \frac{Q^2}{\lambda^3}(R_y R_x b)\,, && \frac{dF_x}{dz} = \frac{Q^2}{\lambda^3}(R_z R_x b + R_x \delta c) \\ &\frac{dF_y}{dx} = \frac{Q^2}{\lambda^3}(R_y R_x b)\,, && \frac{dF_y}{dy} = \frac{Q^2}{\lambda^3}(a + R_y^2 b)\,, && \frac{dF_y}{dz} = \frac{Q^2}{\lambda^3}(R_z R_y b + R_y \delta c) \\ &\frac{dF_z}{dx} = \frac{dF_x}{dz}\,, && \frac{dF_z}{dy} = \frac{dF_z}{dy}\,, && \frac{dF_z}{dz} = \frac{Q^2}{\lambda^3}(a + R_z^2 b + 2R_z\delta c + \delta^2 c) \end{aligned} \tag{2.19}$$

for the case of $R_z = 0$, which will be the only case of interest, the Jacobian matrix is therefore given by

$$\mathbf{J}(\mathbf{R}) = \frac{Q^2}{\lambda^3}\begin{pmatrix} a + R_x^2 b & R_x R_y b & R_x \delta c \\ R_x R_y b & a + R_y^2 b & R_y \delta c \\ R_x \delta c & R_y \delta c & a + \delta^2 c \end{pmatrix} \tag{2.20}$$

2.1.4 Confinement Force

Since the dust particle interaction according to the point-like wake model is dominantly repulsive, the particles would not crystalize in a stable 2 dimensional lattice configuration

without proper confinement. A model for this confinement which was also used in the molecular dynamic simulations [19] and produced correct results is described in the following.
As convention it is assumed that the 2 dimensional monolayer of particles forming the plasma crystal constitutes the x-y plane. In contrast the z-axis is orthogonal to this plane.

On the one hand there is the in plane confinement which restricts the motion in the x-y plane containing the crystal. To model a possible anisotropic fashion two orthogonal axis of compression have to be distinguished. The first is characterized by the confinement parameter $\Omega_{||} = 2\pi f_{||}$ and acts on the axis which encloses the angle α with the positive x-axis (anticlockwise). The second acts perpendicular on α and is characterized by $\Omega_{\perp} = 2\pi f_{\perp}$ (m is the mass of the dust particles).
On the other hand there is a vertical out of plane confinement in the z-direction defined by $\Omega_z = 2\pi f_z$ which is approximately 140-150 times stronger[19] than the in plane confinement. Therefore it enforces a quasi 2 dimensional movement of the particles leading to the formation of a mono layer.

In order to decompose the confinement into a symmetric (s) and an asymmetric (a) component it is helpful to further define $\Omega_a = (\Omega_{||} - \Omega_{\perp})/2$ and $\Omega_s = (\Omega_{||} + \Omega_{\perp})/2$ such that we get

$$\mathbf{C}(\mathbf{x}_i) = \mathbf{C}_i^s + \mathbf{C}_i^a = -m \left[\begin{pmatrix} \Omega_s^2 x_i \\ \Omega_s^2 y_i \\ \Omega_z^2 z_i \end{pmatrix} + \begin{pmatrix} \Omega_a^2 (x_i cos(2\alpha) + y_i sin(2\alpha)) \\ \Omega_a^2 (x_i sin(2\alpha) - y_i cos(2\alpha)) \\ 0 \end{pmatrix} \right] \tag{2.21}$$

2.1.5 Equation of Motion

For a system of N particles exposed to the confinement described in Sec. 2.1.4 and interacting according to the *point-like wake model* (Sec. 2.1.1) the equation of motion for each particle i is given by

$$m\ddot{\mathbf{x}}_i = \mathbf{C}(\mathbf{x}_i) + \sum_{j \neq i} \mathbf{F}(\mathbf{r}_{ji}) \tag{2.22}$$

This equation describes the electrostatic interaction of the system. However to be realistic also the collisions with the neutral parts of the system are important. To be precise friction and thermal fluctuations have to be considered. This can be done as usual by adding friction and the corresponding *Langevin force* [22] what leads to

$$m\ddot{\mathbf{x}}_i + m\nu\dot{\mathbf{x}}_i = \mathbf{C}(\mathbf{x}_i) + \sum_{j \neq i} \mathbf{F}(\mathbf{r}_{ji}) + \mathbf{L}_i(t) \tag{2.23}$$

where ν is the friction parameter and each component $L_i^s(t)$ for $s = x, y, z$ of the Langevin force is characterised by $\langle L_i^s(t) \rangle = 0$, $\langle L_i^s(t) L_i^{\hat{s}}(t+\tau) \rangle = 2\nu m k_B T \delta(\tau) \delta_{s,\hat{s}}$. The average $\langle . \rangle$

is an ensemble average or an average over the values of the force for an fixed time step and no time average.

2.2 Dispersion Relation and Normal Modes

Assuming a system of particles (dust particles, atoms...) forming a stable crystal configuration characterized by Bravais lattice[4]. The interaction shall be given by the force $\mathbf{F}(\mathbf{x}_i - \mathbf{x}_j)$ where $\mathbf{x}_i$ denotes the 3 dimensional position of particle i. For the stable crystal configuration denoted by $\mathbf{X}_j$ the total force on each particle has to vanish, such that $\sum_{j\neq i} \mathbf{F}(\mathbf{X}_i - \mathbf{X}_j) = 0$. If solving the system for only small perturbations it should be sufficient to linearize the force around the equilibrium crystal configuration $\mathbf{X}_j$, such that the equation of motion for particle i is given by:

$$m\,\ddot{\mathbf{d}}_i = \sum_{j\neq i} \cancelto{0}{\mathbf{F}(\mathbf{R}_{ji})} + \sum_{j\neq i} \partial_{\mathbf{R_{ji}}}\mathbf{F}(\mathbf{R}_{ji})(\mathbf{d}_i - \mathbf{d}_j) = \sum_{j\neq i} \mathbf{J}(\mathbf{R}_{ji})(\mathbf{d}_i - \mathbf{d}_j) \tag{2.24}$$

where $\mathbf{R}_{ji} = \mathbf{X}_i - \mathbf{X}_j$ denotes the equilibrium distance, m is the particle mass, $\mathbf{d}_j$ are the small perturbations such that $\mathbf{x}_j = \mathbf{X}_j + \mathbf{d}_j$ and $\partial_{\mathbf{R_{ji}}}\mathbf{F}(\mathbf{R}_{ji}) = \mathbf{J}(\mathbf{R}_{ji})$ is the jacobian matrix of the interaction force evaluated at equilibrium distances $\mathbf{R}_{ji}$. For the case of an infinite crystal or periodic boundary conditions the equations are perfectly symmetric for each particle and we can solve the system by a plane wave ansatz[5] $\mathbf{d}_j(t) = \boldsymbol{\epsilon}\, \exp(-i\omega t + i\mathbf{k}\mathbf{X}_j)$. Inserting it into Eq. 2.24 yields the following eigenvalue problem

$$\omega^2\boldsymbol{\epsilon} = -\frac{1}{m}\sum_{j\neq i} \partial_{\mathbf{R_{ji}}}\mathbf{F}(\mathbf{R}_{ji})[1 - \exp(-i\mathbf{k}\mathbf{R}_{ji})]\,\boldsymbol{\epsilon} = \mathbf{D}(\mathbf{k})\boldsymbol{\epsilon} \tag{2.25}$$

which is independent on i because of the assumed lattice symmetry. Therefore solving the eigenvalue problem Eq. 2.25 solves the whole system simultaneously. The matrix $\mathbf{D}(\mathbf{k})$ is called *dynamical matrix* and the eigenvector $\boldsymbol{\epsilon}$ is referred to as *polarization vector* [2]. Because of the independence on i one can choose always $\mathbf{X}_i = 0$ such that $\mathbf{R}_{ji} = -\mathbf{X}_j$ and $\partial_{\mathbf{R}} = -\partial_{\mathbf{X_j}}$, therefore the dynamical matrix is in general given by

$$\mathbf{D}(\mathbf{k}) = \frac{1}{m}\sum_{\mathbf{X_j}\neq 0} \partial_{\mathbf{X_j}}\mathbf{F}(-\mathbf{X}_j)[1 - \exp(i\mathbf{k}\mathbf{X}_j)] \tag{2.26}$$

where the sum runs over all points of the Bravais lattice $\mathbf{X}_j$ except the origin. For clarification of notation it shall be mentioned that $\partial_{\mathbf{X_j}}\mathbf{F}(-\mathbf{X}_j) = -\mathbf{J}(-\mathbf{X}_j)$.
The dynamical matrix contains all information about the system (properties of the interparticle interaction and stable configuration) and can be seen as function of $\mathbf{k}$.

Using the fact that a Bravais lattice is by definition point symmetric it follows that for every point $\mathbf{X}_j$ it exists a second point $-\mathbf{X}_j$ which is also part of the lattice. Therefore

[4]For definition of the Bravais lattice look at appendix A.1

[5]See appendix A.3 for more information.

replacing $\mathbf{X}_j \to -\mathbf{X}_j$ and $\partial_{\mathbf{X_j}} \to -\partial_{\mathbf{X_j}}$ inside the sum has no impact on the result and one can rewrite Eq. 2.26 into

$$\mathbf{D}(\mathbf{k}) = \frac{1}{m}\left(\frac{1}{2}\sum_{\mathbf{X_j}\neq 0} \partial_{\mathbf{X_j}}\mathbf{F}(-\mathbf{X}_j)[1-\exp(i\mathbf{k}\mathbf{X}_j)] - \partial_{\mathbf{X_j}}\mathbf{F}(\mathbf{X}_j)[1-\exp(-i\mathbf{k}\mathbf{X}_j)]\right) \tag{2.27}$$

2.2.1 Reciprocal Interactions

For reciprocal interactions we have in general $\mathbf{F}(-\mathbf{X}_j) = -\mathbf{F}(\mathbf{X}_j)$ what automatically leads to $\partial_{\mathbf{X_j}}\mathbf{F}(-\mathbf{X}_j) = -\partial_{\mathbf{X_j}}\mathbf{F}(\mathbf{X}_j)$ such that the dynamical matrix becomes the following real matrix

$$\mathbf{D}(\mathbf{k}) = \frac{1}{m}\sum_{\mathbf{X_j}\neq 0} \partial_{\mathbf{X_j}}\mathbf{F}(\mathbf{X}_j)[\cos(\mathbf{k}\mathbf{X}_j)-1] = -\frac{2}{m}\sum_{\mathbf{X_j}\neq 0} \partial_{\mathbf{X_j}}\mathbf{F}(\mathbf{X}_j)\sin^2(\frac{1}{2}\mathbf{k}\mathbf{X}_j) \tag{2.28}$$

In the common case of conservative, reciprocal interactions the dynamical matrix is hence real and symmetric[6]. It has therefore[7] 3 orthogonal real eigenvectors $\boldsymbol{\epsilon}_s(\mathbf{k}) \in \mathbb{R}^{3\times 3}$ which can be normalized and 3 corresponding real eigenvalues $\lambda_s(\mathbf{k}) \in \mathbb{R}$ which fulfill

$$\mathbf{D}(\mathbf{k})\boldsymbol{\epsilon}_s(\mathbf{k}) = \lambda_s(\mathbf{k})\boldsymbol{\epsilon}_s(\mathbf{k}) = \omega^2\boldsymbol{\epsilon}_s(\mathbf{k})\,, \quad s = 1,2,3 \tag{2.29}$$

Solving Eq. 2.29 for all k one gets the *dispersion relation* which is a relation between the wave vector $\mathbf{k}$ and the frequency ω of the wave i.e. $\omega(\mathbf{k}) = f(\mathbf{k})$. Because of the 3 eigenvalues per $\mathbf{k}$ one gets three *branches* of allowed frequencies

$$\omega_s(\mathbf{k}) = \pm\sqrt{\lambda_s(\mathbf{k})}\,, \quad s = 1,2,3 \tag{2.30}$$

The two different signs reflect the 2 possible porpagation directions of the plane wave (compare appendix A.3).
The corresponding eigenvectors $\boldsymbol{\epsilon}_s(\mathbf{k})$ are called *polarization vectors* and give the axis of oscillation. The resulting solutions

$$\mathbf{d}(t,\mathbf{X}_i) = \boldsymbol{\epsilon}_s(\mathbf{k})\exp(i\omega_s(\mathbf{k})t + i\mathbf{k}\mathbf{X}_i)\,, \quad s = 1,2,3 \tag{2.31}$$

are called *normal modes*[8]

[6]The Jacobian ($\mathbf{J}$) of a conservative force is always symmetric. Because the elements of $\mathbf{J}$ are given by $J_{sl} = \partial_{x_s}\partial_{x_l}\phi = \partial_{x_l}\partial_{x_s}\phi = J_{ls}$ where ϕ is the potential of the conservative force.

[7]Standard linear algebra result. Every 3 dimensional real and symmetric matrix has three real eigenvalues. The corresponding eigenvectors can be chosen to be real [1].

[8]Normal modes are plane wave solutions derived in the way it is shown [2]. Normal modes are solutions where the whole system moves with the same frequency ω and a fixed, position dependent, phase relation given by the wave vector $\mathbf{k}$.

In case $\lambda_s(\mathbf{k}) > 0$ one has $\omega_s(\mathbf{k}) = \pm\sqrt{\lambda_s(\mathbf{k})} \in \mathbb{R}$ and therefore $\mathbf{d}_j(t) \propto \exp(\mp i\omega_s(\mathbf{k})t)$ represent stable oscillations whereas in case $\lambda_s(\mathbf{k}) < 0$ one has $\omega_s(\mathbf{k}) = \pm i\sqrt{||\lambda_s(\mathbf{k})||} \in \mathbb{C}$ and therefore $\mathbf{d}_j(t) \propto \exp(\mp\omega_s(\mathbf{k})t)$ would represent exponentially decaying/growing solutions. Therefore to form a stable crystal, $\lambda_s(\mathbf{k}) > 0$ hast to be true for every $\mathbf{k}$.

2.2.2 Nonreciprocal Interactions

For non-reciprocal interactions we have in general $\mathbf{F}(-\mathbf{X}_j) \neq -\mathbf{F}(\mathbf{X}_j)$. Identical to Sec. 2.1.2 one can separate the force into a reciprocal and the corresponding non-reciprocal part

$$\mathbf{F}(-\mathbf{X}_j) = -\mathbf{F}(\mathbf{X}_j) + \boldsymbol{\gamma}(\mathbf{X}_j)\,, \quad \boldsymbol{\gamma}(\mathbf{X}_j) = \mathbf{F}(-\mathbf{X}_j) + \mathbf{F}(\mathbf{X}_j) \tag{2.32}$$

where $\boldsymbol{\gamma}(\mathbf{X}_j)$ represents the nonreciprocal part of the interaction. This definition leads to $\partial_{\mathbf{X_j}}\mathbf{F}(-\mathbf{X}_j) = -\partial_{\mathbf{X_j}}\mathbf{F}(\mathbf{X}_j) + \partial_{\mathbf{X_j}}\boldsymbol{\gamma}(\mathbf{X}_j)$ such that the dynamical matrix Eq. 2.27 can be represented as

$$\begin{aligned}\mathbf{D}(\mathbf{k}) = &-\frac{2}{m}\sum_{\mathbf{X_j}\neq 0}\partial_{\mathbf{X_j}}\mathbf{F}(\mathbf{X}_j)\sin^2(\frac{1}{2}\mathbf{k}\mathbf{X}_j) \\ &+\frac{1}{m}\frac{1}{2}\sum_{\mathbf{X_j}\neq 0}\partial_{\mathbf{X_j}}\boldsymbol{\gamma}(\mathbf{X}_j)[1-\cos(\mathbf{k}\mathbf{X}_j) - i\sin(\mathbf{k}\mathbf{X}_j)]\end{aligned} \tag{2.33}$$

From definition Eq. 2.32 it is obvious that $\boldsymbol{\gamma}(\mathbf{X}_j) = \boldsymbol{\gamma}(-\mathbf{X}_j)$ and therefore $\partial_{\mathbf{X_j}}\boldsymbol{\gamma}(\mathbf{X}_j) = \partial_{\mathbf{X_j}}\boldsymbol{\gamma}(-\mathbf{X}_j)$ what determines the contribution from every $\mathbf{X}_s = \mathbf{Y}$ with its point symmetric counterpart $\mathbf{X}_l = -\mathbf{Y}$ to be antisymmetric[9] i.e. $-\partial_{\mathbf{X_s}}\boldsymbol{\gamma}(\mathbf{X}_s) = \partial_{\mathbf{X_l}}\boldsymbol{\gamma}(\mathbf{X}_l)$.
In consequence the sum over all $\partial_{\mathbf{X_j}}\boldsymbol{\gamma}(\mathbf{X}_j)[1-\cos(\mathbf{k}\mathbf{X}_j)]$ cancels out, since it is antisymmetric. In contrast the $\partial_{\mathbf{X_j}}\boldsymbol{\gamma}(\mathbf{X}_j)[i\sin(\mathbf{k}\mathbf{X}_j)]$ part contributes as it is symmetric. Such that the dynamical matrix can be written as

$$\mathbf{D}(\mathbf{k}) = -\frac{2}{m}\sum_{\mathbf{X_j}\neq 0}\partial_{\mathbf{X_j}}\mathbf{F}(\mathbf{X}_j)\sin^2(\frac{1}{2}\mathbf{k}\mathbf{X}_j) - i\frac{1}{m}\sum_{\mathbf{X_j}\neq 0}\frac{1}{2}\partial_{\mathbf{X_j}}\boldsymbol{\gamma}(\mathbf{X}_j)\sin(\mathbf{k}\mathbf{X}_j) \tag{2.34}$$

The dynamical matrix for the case of non-reciprocal interactions is therefore in general complex $\mathbf{D}(\mathbf{k}) \in \mathbb{C}^{3\times 3}$ and not necessarily hermitian. Hence the eigenvalues fulfilling

$$\mathbf{D}(\mathbf{k})\boldsymbol{\epsilon}_s(\mathbf{k}) = \lambda_s(\mathbf{k})\boldsymbol{\epsilon}_s(\mathbf{k}) = \tilde{\omega}^2\boldsymbol{\epsilon}_s(\mathbf{k})\,, \quad s = 1,2,3 \tag{2.35}$$

are in general complex $\lambda_s(k) \in \mathbb{C}$. Also the eigenvectors are complex $\boldsymbol{\epsilon}_s(\mathbf{k}) \in \mathbb{C}^3$ and not necessarily orthogonal. For convenience the complex frequency was introduced given by $\tilde{\omega} = \omega + ig$ with the real frequency ω and the growth rate g.

[9] This can easily seen by $\partial_{\mathbf{X_l}}\boldsymbol{\gamma}(\mathbf{X}_l) =^a -\partial_{\mathbf{Y}}\boldsymbol{\gamma}(-\mathbf{Y}) =^b -\partial_{\mathbf{Y}}\boldsymbol{\gamma}(\mathbf{Y}) =^c -\partial_{\mathbf{X_s}}\boldsymbol{\gamma}(\mathbf{X}_s)$ where $(a)\,\mathbf{X}_l = -\mathbf{Y} \to \partial_{\mathbf{X}l} = -\partial_{\mathbf{Y}}$, $(b)\,\boldsymbol{\gamma}(\mathbf{Y}) = \boldsymbol{\gamma}(-\mathbf{Y})$, $(c)\,\mathbf{X}_s = \mathbf{Y} \to \partial_{\mathbf{X_s}} = \partial_{\mathbf{Y}}$ was used in the given order.

Solving Eq. 2.35 for all $\mathbf{k}$ one gets in this case a complex dispersion relation with three branches given by

$$\tilde{\omega}_s(\mathbf{k}) = \pm\sqrt{\lambda_s(\mathbf{k})} = \pm\omega_s(\mathbf{k}) \pm i g_s(\mathbf{k})\,, \qquad s = 1,2,3 \tag{2.36}$$

and corresponding polarization vectors $\boldsymbol{\epsilon}_s(\mathbf{k})$.
Such that there are normal modes

$$\mathbf{d}(t, \mathbf{X}_i) = \boldsymbol{\epsilon}_s(\mathbf{k}) \exp(\pm g_s(\mathbf{k})t) \exp(\mp i\omega_s(\mathbf{k})t + i\mathbf{k}\mathbf{X}_i)\,, \qquad s = 1,2,3 \tag{2.37}$$

New Effects for Nonreciprocal Normal Modes

Elliptic polarization: Since it is not always possible to chose the polarization vectors $\boldsymbol{\epsilon}_s(\mathbf{k})$ to be real one may get a phase shift between the different dimensions what causes elliptic polarization[33]. This can easily be seen by writing every component of $\boldsymbol{\epsilon}$ using Euler's formula. $\boldsymbol{\epsilon} = (\epsilon_x, \epsilon_y, \epsilon_z)^T = (|\epsilon_x|e^{i\alpha_x}, |\epsilon_y|e^{i\alpha_y}, |\epsilon_z|e^{i\alpha_z})^T$. Focusing on the local oscillatory motion and assuming a normal mode $\mathbf{d}(t) \propto \boldsymbol{\epsilon}\exp(-i\omega t)$ the physical relevant real part of the trajectory can be written as

$$\mathbf{d}(t) = \mathrm{Re}\left\{ \begin{pmatrix} |\epsilon_x|e^{i\alpha_x} \\ |\epsilon_y|e^{i\alpha_y} \\ |\epsilon_z|e^{i\alpha_z} \end{pmatrix} \exp(-i\omega t) \right\} = \begin{pmatrix} |\epsilon_x|\cos(\alpha_x - \omega t) \\ |\epsilon_y|\cos(\alpha_y - \omega t) \\ |\epsilon_z|\cos(\alpha_z - \omega t) \end{pmatrix} \tag{2.38}$$

If it is not possible to chose $\boldsymbol{\epsilon}$ to be real $\alpha_{x,y,z}$ has to be different for at least two dimensions. Consequently the induced motion affects more than one linear independent spatial dimension and will form some kind of elliptical orbits [26].

Exponential growing/decaying oscillations: In case $\lambda_s(\mathbf{k}) \in \mathbb{R}$ one has the same situation as in the reciprocal case. However if $g_s(\mathbf{k})) \neq 0$ the solution is a oscillation with exponentially growing or decaying amplitude ($\mathbf{d}(t) \propto \exp(g_s(\mathbf{k})t)\exp(-i\omega_s(\mathbf{k})t)$). This is not possible for the reciprocal case. If looking at both possible solutions $\tilde{\omega}_s(\mathbf{k}) = \pm\sqrt{\lambda_s(\mathbf{k})} = \pm\omega_s(\mathbf{k}) \pm i g_s(\mathbf{k})$ it is obvious that, if $g_s(\mathbf{k})) \neq 0$ there is always one exponentially growing and one exponential decaying solution no matter what sign $g_s(\mathbf{k})$ has. Obviously such solutions imply a growing energy of the system. This is possible since energy conservation is not valid for non-reciprocal interactions as clarified in Sec. 2.1.2.

Preferred direction of wave propagation: The two possible solutions in Eq. 2.35 $\tilde{\omega}_s(\mathbf{k}) = \pm\sqrt{\lambda_s(\mathbf{k})} = \pm\omega_s(\mathbf{k}) \pm i g_s(\mathbf{k})$ reflect the two possible propagation directions of the normal mode. The corresponding plane waves show a position and time dependence according to $\mathbf{d}(t) \propto \exp(\mp i\omega_s(\mathbf{k})t + i\mathbf{k}\mathbf{X}_i)\exp(\pm g_s(\mathbf{k})t)$. If we denote the argument of the complex exponential function as phase Φ ($\exp(i\Phi)$), we see that for the positive solution the value of constant phase "$const = \Phi = -\omega_s(\mathbf{k})t + \mathbf{k}\mathbf{X}_i$" propagates in the direction of $\mathbf{k}$ with growth rate $+g_s(\mathbf{k})$ while for the negative solution we have "$const = \Phi = \omega_s(\mathbf{k})t + \mathbf{k}\mathbf{X}_i$" what indicates propagation in opposite direction of $\mathbf{k}$ with growth rate $-g_s(\mathbf{k})$. This shows that one propagation direction grows exponentially while the other directions decays. This reflects the broken symmetry of the non-reciprocal interaction.

2.2.3 Influence of Friction and Confinement

If the each particle i experiences a external confinement force $\mathbf{C}(\mathbf{x}_i)$ and the friction force $-m\nu\dot{\mathbf{x}}_i$ in addition to the particle interaction the equation of motion, linearized around a stable equilibrium configuration becomes

$$m\,\ddot{\mathbf{d}}_i + m\,\nu\dot{\mathbf{d}}_\mathbf{i} = \partial_{\mathbf{X_i}}\mathbf{C}(\mathbf{X}_i)\mathbf{d}_i + \sum_{j\neq i}\partial_{\mathbf{R_{ji}}}\mathbf{F}(\mathbf{R}_{ji})(\mathbf{d}_i - \mathbf{d}_j) \tag{2.39}$$

the same plane wave ansatz ($\mathbf{d}_j(t) = \boldsymbol{\epsilon}\,\exp(-i\tilde{\omega}t + i\mathbf{k}\mathbf{X}_j)$) using the complex frequency $\tilde{\omega} = \omega + ig$ leads to slightly modified eigenvalue equation

$$(\tilde{\omega}^2 + i\nu\tilde{\omega})\boldsymbol{\epsilon}(\mathbf{k}) = \left[\mathbf{D}(\mathbf{k}) - \frac{1}{m}\partial_{\mathbf{X_i}}\mathbf{C}(\mathbf{X}_i)\right]\boldsymbol{\epsilon}(\mathbf{k}) \tag{2.40}$$

where we have to solve for the eigenvalues $\lambda(\mathbf{k})_s$ and eigenvectors $\boldsymbol{\epsilon}_s(\mathbf{k})$ according to

$$\lambda_s(\mathbf{k})\boldsymbol{\epsilon}_s(\mathbf{k}) = -\frac{1}{m}\left[\mathbf{D}(\mathbf{k}) - \frac{1}{m}\partial_{\mathbf{X_i}}\mathbf{C}(\mathbf{X}_i)\right]\boldsymbol{\epsilon}_s(\mathbf{k})\,, \quad s = 1,2,3 \tag{2.41}$$

and after that solving $\tilde{\omega}_s^2(\mathbf{k}) + i\nu\tilde{\omega}_s(\mathbf{k}) = \lambda_s(\mathbf{k})$ to get the dispersion relation.

As can be seen the eigenvalue calculation is independent on ν. Therefore it is often convenient to define $\Omega_s^2(\mathbf{k}) = \tilde{\omega}_s^2(\mathbf{k}) + i\nu\tilde{\omega}_s(\mathbf{k})$ solve for $\Omega_s^2(\mathbf{k}) = \lambda_s(\mathbf{k})$ and after that consider the influence of ν. If writing $\lambda_s(\mathbf{k}) = \lambda_s^{Re}(\mathbf{k}) + i\lambda_s^{Im}(\mathbf{k})$ the solutions of $\tilde{\omega} = \omega + ig$ for the relevant case $\lambda_s^{Re}(\mathbf{k}) > \nu^2/4$ are given by

$$\begin{aligned}
\omega_s^{\pm}(\mathbf{k}) &= \pm\sqrt{\frac{1}{2}\left([\lambda_s^{Re}(\mathbf{k}) - \nu^2/4] + \sqrt{[\lambda_s^{Re}(\mathbf{k}) - \nu^2/4]^2 + \lambda_s^{Im}(\mathbf{k})^2}\right)} \\
g_s^{\pm}(\mathbf{k}) &= \frac{\lambda_s^{Im}(\mathbf{k})}{2\omega_s^{\pm}(\mathbf{k})} - \frac{\nu}{2}
\end{aligned} \tag{2.42}$$

In case of approximately weak friction, i.e. $\mathrm{Re}(\Omega_s(\mathbf{k}) >> \nu$ one can use the simple relation $\tilde{\omega}_s^{\pm}(\mathbf{k}) \approx \Omega_s^{\pm}(\mathbf{k}) - i\nu/2$.

Since the real frequency $\omega_s^{\pm}(\mathbf{k})$ in any case shows only a switching sign for the tow possible mathematical solutions it shall be expressed as $\omega_s^{\pm}(\mathbf{k}) = \pm\omega_s(\mathbf{k})$ for the growth rate this simple relation is only possible in case of vanishing friction $\nu = 0$. Thus the two mathematical solutions of the equation $(\tilde{\omega}^2 + i\nu\tilde{\omega}) = \lambda_s(\mathbf{k})$ shall be denoted as

$$\tilde{\omega}_s^{\pm}(\mathbf{k}) = \pm\omega_s(\mathbf{k}) + ig_s^{\pm}(\mathbf{k}) \tag{2.43}$$

During this thesis in most cases the complex frequency will be referred to as

$$\tilde{\omega}(\mathbf{k}) = \omega_s(\mathbf{k}) + ig_s(\mathbf{k}) \tag{2.44}$$

In this cases the solutions with positive real frequency $\tilde{\omega}_s^{+}(\mathbf{k})$ was used.

2.2.4 General Solution of the Linear System

To sum up for any allowed $\mathbf{k}$-vector we have 3 pairs of solutions $\tilde{\omega}_s^{\pm}(\mathbf{k}) = \pm\omega_s(\mathbf{k}) + ig_s^{\pm}(\mathbf{k})$ for the three branches $s = 1, 2, 3$. In principle the negative solutions can be constructed out of the positive ones (for $\nu = 0$ only the sign is switched). What is not surprising since both solutions only reflect the two possible propagation directions of the normal mode. However if we want construct a solution as superposition of all found solutions in the most general way we have to treat both propagation directions as independent solutions.
In the following the dependence on $\mathbf{k}$ is now written as subscript to avoid confusing notation, i.e. $\tilde{\omega}_{s,\mathbf{k}}^{+} = \omega_{s,\mathbf{k}} + ig_{s,\mathbf{k}}^{+}$ and $\tilde{\omega}_{s,\mathbf{k}}^{-} = -\omega_{s,\mathbf{k}} + ig_{s,\mathbf{k}}^{-}$. With this convention the most general linear superposition of all plane waves solving the linear system can be written as

$$\mathbf{d}(\mathbf{X}_i, t) = \sum_{\mathbf{k}\in 1.BZ} \exp(i\mathbf{k}\mathbf{X}_i) \sum_{s=1}^{3} \boldsymbol{\epsilon}_{s,\mathbf{k}} \left[A_{s,\mathbf{k}} \exp(g_{s,\mathbf{k}}^{+} t - i\omega_{s,\mathbf{k}} t) + B_{s,\mathbf{k}} \exp(g_{s,\mathbf{k}}^{-} t + i\omega_{s,\mathbf{k}} t) \right] \tag{2.45}$$

where $A_{s,\mathbf{k}}$, $B_{s,\mathbf{k}}$ denote complex constants and the sum runs over all allowed $\mathbf{k}$-vectors of the 1st Brillouin zone.
Even if normal modes represent very special solutions of collective motion, its linear superposition can solve the system for arbitrary initial conditions.[10]
Given initial positions $\mathbf{d}_0(\mathbf{X}_i)$ and velocities $\mathbf{v}_0(\mathbf{X}_i)$ one can demand that these conditions are provided by the solution given in Eq. 2.49 for $t = 0$ without loss of generality. If this is true the system is solved for any time.
The corresponding constants $A_{s,\mathbf{k}}$, $B_{s,\mathbf{k}}$ can be found by representing the initial conditions

[10] In case of the infinite crystal or periodic boundary conditions. Since this assumptions are necessary to obtain the plain wave normal mode solutions.

by its discrete Fourier transformation. As shown in appendix A.4 this representation is given as

$$\begin{aligned}\mathbf{d}_0(\mathbf{X}_i) &= \sum_{\mathbf{k}} \tilde{\mathbf{d}}_0(\mathbf{k}) \exp(i\mathbf{k}\mathbf{X}_i), \text{ with } \tilde{\mathbf{d}}_0(\mathbf{k}) = \frac{1}{N}\sum_{\mathbf{X}_i} \mathbf{d}_0(\mathbf{X}_i)\exp(-i\mathbf{k}\mathbf{X}_i) \\ \mathbf{v}_0(\mathbf{X}_i) &= \sum_{\mathbf{k}} \tilde{\mathbf{v}}_0(\mathbf{k}) \exp(i\mathbf{k}\mathbf{X}_i), \text{ with } \tilde{\mathbf{v}}_0(\mathbf{k}) = \frac{1}{N}\sum_{\mathbf{X}_i} \mathbf{v}_0(\mathbf{X}_i)\exp(-i\mathbf{k}\mathbf{X}_i)\end{aligned} \tag{2.46}$$

where the sum over $\mathbf{k}$ includes all $\mathbf{k}$-vectors allowed according to periodic boundary conditions. Comparing now $\mathbf{d}(\mathbf{X}_i, t=0)$ and $\dot{\mathbf{d}}(\mathbf{X}_i, t=0)$ it is obvious that the initial conditions are fulfilled for $t=0$ if the following relations are true

$$\begin{aligned}\tilde{\mathbf{d}}_0(\mathbf{k}) &= \sum_{s=1}^{3} \boldsymbol{\epsilon}_{s,\mathbf{k}}[A_{s,\mathbf{k}} + B_{s,\mathbf{k}}] = \mathbf{T}\boldsymbol{\alpha} \\ \tilde{\mathbf{v}}_0(\mathbf{k}) &= \sum_{s=1}^{3} \boldsymbol{\epsilon}_{s,\mathbf{k}}[A_{s,\mathbf{k}}(g^{+}_{s,\mathbf{k}} - i\omega_{s,\mathbf{k}}) + B_{s,\mathbf{k}}(g^{-}_{s,\mathbf{k}} + i\omega_{s,\mathbf{k}})] = \mathbf{T}\boldsymbol{\beta}\end{aligned} \tag{2.47}$$

with the matrix $\mathbf{T} = (\boldsymbol{\epsilon}_{1,\mathbf{k}}, \boldsymbol{\epsilon}_{2,\mathbf{k}}, \boldsymbol{\epsilon}_{3,\mathbf{k}})$ and the two vectors $\boldsymbol{\alpha} = (A_{1,\mathbf{k}} + B_{1,\mathbf{k}}, ...)^T$ and $\boldsymbol{\beta} = (A_{1,\mathbf{k}}(g^{+}_{1,\mathbf{k}} - i\omega_{1,\mathbf{k}}) + B_{1,\mathbf{k}}(g^{-}_{1,\mathbf{k}} + i\omega_{1,\mathbf{k}}), ...)^T$. This system of linear equations is solvable if $\mathbf{T}$ has full rank [1], i.e. the different $\boldsymbol{\epsilon}_{s,\mathbf{k}}$ are linear independent. This is always given as long as the eigenvalues are mutually different[1].

This shows that one may think of the crystal motion as superposition of all possible normal modes and propagation directions. Since strictly spoken, normal modes are solutions of the infinite or periodic crystal this picture may be valid as long as boundary effects are negligible.

Special Properties of Real Solutions

The written superposition of normal modes includes also complex solutions. However since we describe physical real oscillations $\mathbf{d}(t) \in \mathbb{R}^3$ this implies some restrictions on the possible solutions. Which will briefly discussed in the following.
Since also the initial conditions are real ($\mathbf{d}_0(\mathbf{X}_i) \in \mathbb{R}^3$) we have for the Fourier transformed initial conditions

$$\sum_{s=1}^{3} \boldsymbol{\epsilon}_{s,\mathbf{k}}[A_{s,\mathbf{k}} + B_{s,\mathbf{k}}] = \tilde{\mathbf{d}}_0(\mathbf{k}) = \overline{\tilde{\mathbf{d}}_0(-\mathbf{k})} = \sum_{s=1}^{3} \boldsymbol{\epsilon}_{s,-\mathbf{k}}[A_{s,-\mathbf{k}} + B_{s,-\mathbf{k}}] \tag{2.48}$$

where the overline denotes the complex conjugate. In addition we know for the dynamical matrix holds $\mathbf{D}(\mathbf{k}) = \overline{\mathbf{D}(-\mathbf{k})}$ what implies $\boldsymbol{\epsilon}_{s,\mathbf{k}} = \overline{\boldsymbol{\epsilon}_{s,-\mathbf{k}}}$ and $\lambda_{s,\mathbf{k}} = \overline{\lambda_{s,-\mathbf{k}}}$. This can directly be seen from the definition of the dynamical matrix (Eq. 2.34 on page 11).

Using Eq. 2.48 and $\boldsymbol{\epsilon}_{s,\mathbf{k}} = \overline{\boldsymbol{\epsilon}_{s,-\mathbf{k}}}$ it is obvious that $[A_{s,\mathbf{k}} + B_{s,\mathbf{k}}] = \overline{[A_{s,-\mathbf{k}} + B_{s,-\mathbf{k}}]}$. The relation $\lambda_{s,\mathbf{k}} = \overline{\lambda_{s,-\mathbf{k}}}$ directly implies [11] $\omega_{s,\mathbf{k}} = \omega_{s,-\mathbf{k}}$ and $g^+_{s,-\mathbf{k}} = g^-_{s,\mathbf{k}}$ or $g^-_{s,-\mathbf{k}} = g^+_{s,\mathbf{k}}$ respectively. With this information it is easy to show that the pairs of solution $(\tilde{\omega}^+_{s,\mathbf{k}}, \tilde{\omega}^-_{s,-\mathbf{k}})$ and $(\tilde{\omega}^+_{s,-\mathbf{k}}, \tilde{\omega}^-_{s,\mathbf{k}})$ are always complex conjugated solutions canceling out the imaginary part in the complex linear superposition (Eq. 2.49). Thus a real solution can be expressed by focusing only on the solutions with positive real frequency $\tilde{\omega}^+_{s,\mathbf{k}} = \omega_{s,\mathbf{k}} + ig^+_{s,\mathbf{k}}$ according to

$$\begin{aligned}\mathbf{d}(\mathbf{X}_i, t) &= \sum_{\mathbf{k}\in 1.BZ} 2\mathrm{Re}\left\{\sum_{s=1}^{3} \boldsymbol{\epsilon}_{s,\mathbf{k}} A_{s,\mathbf{k}} \exp(g^+_{s,\mathbf{k}} t) \exp(-i(\omega_{s,\mathbf{k}} t - \mathbf{k}\cdot\mathbf{X}_i))\right\} \\ &= \sum_{\mathbf{k}\in 1.BZ} \sum_{s=1}^{3} |A_{s,\mathbf{k}}| \begin{pmatrix} |\epsilon^x_{s,\mathbf{k}}| \cos(\omega_{s,\mathbf{k}} t - \mathbf{k}\cdot\mathbf{X}_i - \gamma^x_{s,\mathbf{k}} - \alpha_{s,\mathbf{k}})) \\ |\epsilon^y_{s,\mathbf{k}}| \cos(\omega_{s,\mathbf{k}} t - \mathbf{k}\cdot\mathbf{X}_i - \gamma^y_{s,\mathbf{k}} - \alpha_{s,\mathbf{k}})) \\ |\epsilon^z_{s,\mathbf{k}}| \cos(\omega_{s,\mathbf{k}} t - \mathbf{k}\cdot\mathbf{X}_i - \gamma^z_{s,\mathbf{k}} - \alpha_{s,\mathbf{k}})) \end{pmatrix} \exp(g^+_{s,\mathbf{k}} t)\end{aligned} \tag{2.49}$$

Where $\boldsymbol{\epsilon}_{s,\mathbf{k}} = (\epsilon^x_{s,\mathbf{k}}, \epsilon^y_{s,\mathbf{k}}, \epsilon^z_{s,\mathbf{k}})^T = (|\epsilon_x| e^{i\gamma^x_{s,\mathbf{k}}}, |\epsilon^y_{s,\mathbf{k}}| e^{i\gamma^y_{s,\mathbf{k}}}, |\epsilon^z_{s,\mathbf{k}}| e^{i\gamma^z_{s,\mathbf{k}}})^T$ and $A_{s,\mathbf{k}} = |A_{s,\mathbf{k}}| e^{i\alpha_{s,\mathbf{k}}}$. Obviously the formulation in terms of the complex exponential function is by far the more convenient one and will be used in most situations.

If using only the solutions with positive real frequency the direction of the $\mathbf{k}$-vector always is the propagation direction of the plane wave [12]. Since $g^+_{s,-\mathbf{k}} = g^-_{s,\mathbf{k}}$ this again shows that the plane wave resulting form an complex eigenvalue $\lambda_{s,\mathbf{k}}$ has a preferred propagation direction.

Dispersion Relation

As shown in the last part all physical information is captured by considering only positive real frequencies. Therefore if dispersion relations are calculated (i.e. $\tilde{\omega} = f(\mathbf{k})$) in upcoming parts only the positive solutions $\tilde{\omega}^+_{s,\mathbf{k}} = \omega_{s,\mathbf{k}} + ig^+_{s,\mathbf{k}}$ are shown.

2.3 Lattice Description

The real lattice of a plasma crystal shows defects and the particle distances are varying. However in order to calculate the dispersion relation and normal modes a perfect Bravais lattice is necessary. The plasma crystal of interest is normally approximated by the perfect 2D hexagonal Bravais lattice[35]. To take a possible anisotropic confinement into consideration it will be further necessary to describe a deformed hexagonal lattice.

[11] Compare the definition in Eq. 2.42 on page 13.
[12] Compare appendix A.3

2.3.1 The Perfect 2 Dimensional Hexagonal Lattice

If the lattice constant is denoted by Δ the 2-dimensional hexagonal Bravais lattice[13] can be described by the two primitive vectors

$$\mathbf{a}_1^* = \Delta \begin{pmatrix} 0 \\ 1 \end{pmatrix}, \mathbf{a}_2^* = \Delta \begin{pmatrix} \sqrt{3}/2 \\ 1/2 \end{pmatrix} \tag{2.50}$$

the corresponding reciprocal lattice[14] vectors $\mathbf{b}_1^*$, $\mathbf{b}_2^*$ are given by

$$\mathbf{b}_1^* = \frac{2\pi}{\Delta} \begin{pmatrix} -1/\sqrt{3} \\ 1 \end{pmatrix}, \mathbf{b}_2^* = \frac{2\pi}{\Delta} \begin{pmatrix} 2/\sqrt{3} \\ 0 \end{pmatrix} \tag{2.51}$$

The basis vectors of lattice and reciprocal lattice are mutually orthogonal what can be expressed by the relation $\mathbf{a}_i^* \cdot \mathbf{b}_j = 2\pi\delta_{ij}$. Where $\delta_{ij} = 1$ if $i = j$ and $\delta_{ij} = 0$ if $i \neq j$.

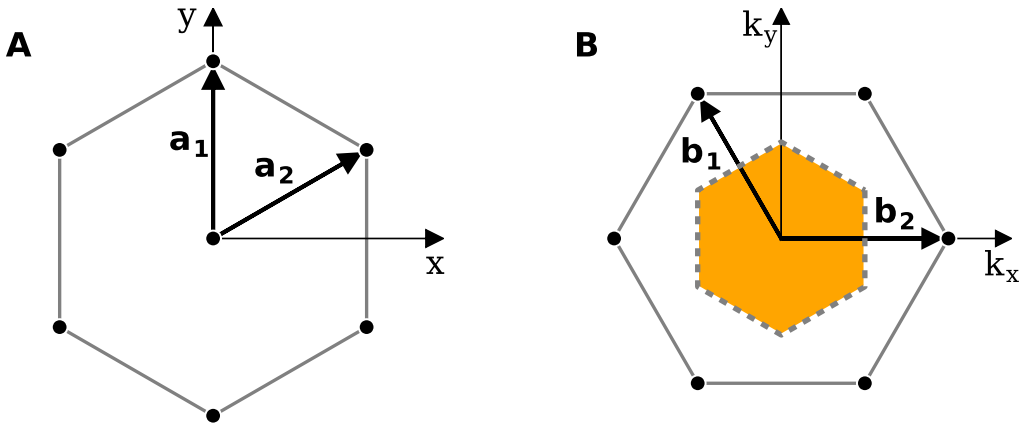

Figure 2.1: Perfect hexagonal lattice (A) and corresponding reciprocal lattice (B). The orange area is the 1st Brillouin Zone of the reciprocal lattice.

The hexagonal Bravais lattice are now all points in real-space defined through

$$\{\mathbf{x} \,|\, \mathbf{x}(n_1, n_2) = n_1\mathbf{a}_1^* + n_2\mathbf{a}_2^*, \;\; n_1, n_2 \in \mathbb{Z}\} \tag{2.52}$$

and the corresponding reciprocal lattice are all points in $\mathbf{k}$-space defined through

$$\{\mathbf{k} \,|\, \mathbf{k}(m_1, m_2) = m_1\mathbf{b}_1^* + m_2\mathbf{b}_2^*, \;\; m_1, m_2 \in \mathbb{Z}\} \tag{2.53}$$

[13]For definition of the Bravais lattice look at appendix A.1
[14]For definition of reciprocal lattice, real-space and k-space look at appendix A.2.

On Figure 2.1 the *1st Brillouin zone* of the reciprocal lattice is shown. It contains all relevant **k**-vectors of the reciprocal lattice. Since any wave vector from outside the 1st Brillouin zone can be replaced by a vector inside the 1st Brillouin zone which produces the absolute identical wave pattern. Consequently only vectors from inside the 1st Brillouin zone are physical relevant (see also appendix A.3).

2.3.2 Deformed 2 Dimensional Hexagonal Lattice

In general the deformation of a hexagonal lattice can be characterized in the following way [15].
Lets denote an arbitrary position of the hexagonal lattice by $\mathbf{x}^* = \mathbf{a}_1^* n + \mathbf{a}_2^* m$, where $n, m \in \mathbb{Z}$. The corresponding vector after deformation of the lattice shall be denoted by $\mathbf{x}$ and can given by

$$\mathbf{x} = \mathbf{T}\mathbf{R}\mathbf{x}^* \tag{2.54}$$

$\mathbf{R}$ denotes a rotation in the lattice plane an can be set to unity by proper rotation of the coordinate system without loss of generality. $\mathbf{T}$ is the deformation matrix which contains the relevant information about the deformation. $\mathbf{T}$ can be decomposed into a pure share component (denoted by p) and a simple share component (denoted by s)[18, 15]. The corresponding transformation matrices are given by

$$\mathbf{T}_p = \begin{pmatrix} \mu & 0 \\ 0 & \mu^{-1} \end{pmatrix}, \mathbf{T}_s = \begin{pmatrix} 1 & 0 \\ \tau & 0 \end{pmatrix} \tag{2.55}$$

Pure share characterized by the *contraction factor*[15] μ results in a asymmetric rescaling of the orthogonal coordinate axes which we denote as x and y direction. While the one direction is contradicted the other one is extended by the inverse factor.

Simple share is defined by the *strain* τ. The effect of simple share is a shift into the y direction for all lattice points depending linear on their x position ($\Delta y = \tau x$), such that τ can be interpreted as kind of slope in x direction. The effect is a constant shift for rows of same x in the y direction.
Note however that a combination of pure and simple share with given τ and μ is not commutative, since

$$\mathbf{T}_p \mathbf{T}_s = \begin{pmatrix} \mu & 0 \\ \mu^{-1}\tau & \mu^{-1} \end{pmatrix} \neq \begin{pmatrix} \mu & 0 \\ \mu\tau & \mu^{-1} \end{pmatrix} = \mathbf{T}_s \mathbf{T}_p \tag{2.56}$$

As one can see it is not commutative since the $\mathbf{T}_p \mathbf{T}_s$ order the simple share slope τ acts on the x component of the perfect lattice and is compressed by pure share afterwards while in the $\mathbf{T}_s \mathbf{T}_p$ order the simple share slope acts on the already pure share deformed x component. To avoid confusion and for simplicity the combined deformation matrix $\mathbf{T}$ is used given by

$$\mathbf{T} = \begin{pmatrix} \mu & 0 \\ m & \mu^{-1} \end{pmatrix} \tag{2.57}$$

[15] Terminology borrowed from [15].

where m is chosen giving the desired deformed lattice. During this thesis μ is denoted as *contraction factor* while m will be called *share slope*.

The deformation matrix for the reciprocal lattice denoted by $\mathbf{T}^b$ is connected [15] to the deformation matrix of the real lattice by $\mathbf{T}^b = (\mathbf{T^{-1}})^T$ and given by

$$\mathbf{T}^b = \begin{pmatrix} \mu^{-1} & -m \\ 0 & \mu \end{pmatrix} \tag{2.58}$$

To sum up we have primitive lattice vectors for the deformed real lattice denoted by $\mathbf{a}_1$, $\mathbf{a}_2$ and for the deformed reciprocal lattice denoted by $\mathbf{b}_1$, $\mathbf{b}_2$ defined by

$$\mathbf{a}_1 = \mathbf{T}\,\mathbf{a}_1^*,\ \mathbf{a}_2 = \mathbf{T}\,\mathbf{a}_1^*, \qquad \mathbf{b}_1 = \mathbf{T}^b\,\mathbf{b}_1^*,\ \mathbf{b}_2 = \mathbf{T}^b\,\mathbf{b}_1^*, \tag{2.59}$$

Chapter 3

Mode-Coupling Instability

The term *mode-coupling instability* or *MCI* describes a plasma-specific melting mechanism [6] of 2 dimensional plasma crystals. As described in Sec. 2.1.1 caused by the plasma wake, the effective interaction between the dust particles is nonreciprocal. Under proper conditions this makes the crystal system non-Hamiltonian and energy is continuously transferred from the ion flow to the crystal formed by the dust particles. Finally the heating destroys the order and causes the crystal melting. This wake-induced mechanism of plasma crystal melting was first described by Ivlev and Morfill [13], generalized for the 2D case by Zhdanov, Ivlev and Morfill [35]. They showed that this instability is triggered if two specific modes of the crystals dispersion relation cross. If this happens they couple and form a so called *hybrid mode* which shows exponential growth in kinetic energy. For that reason it is termed *mode-coupling instability*. In the following the aspects of the MCI relevant for this thesis are summarized.

3.1 Dispersion Relation of the 2D Plasma Crystal

For the calculation of the dispersion relation the plasma crystal has to be approximated by the corresponding perfect Bravais lattice described in Sec. refsec:lattice which reflects the general symmetry of the crystal. A direct consequence of the assumption of a perfect infinite or periodic lattice is that the horizontal confinement (i.e. the x- and y-component) must be set to zero to be consistent. Only the z-component is still necessary, such that the confinement becomes $\mathbf{C}(\mathbf{x}_i) = -\mathbf{e_z} m\Omega_z^2 z_i$ where $\mathbf{e_z}$ is the unit vector in z-direction.
The resulting equation of motion of particle i for an infinite or periodic perfect hexagonal crystal is therefore given by

$$m\ddot{\mathbf{x}}_i + m\nu\dot{\mathbf{x}}_i = -\mathbf{e_z} m\Omega_z^2 z_i + \sum_{j\neq i} \mathbf{F}(\mathbf{r}_{ji}) \tag{3.1}$$

where ν is the damping rate from neutral gas friction. The particle interaction $\mathbf{F}(\mathbf{r}_{ji})$ is given by the point-like wake model and therefore non-reciprocal. As shown in Sec. 2.2.3 to solve for the normal modes and dispersion relation one has to solve the eigenvalue equation

$$\lambda_s(\mathbf{k})\boldsymbol{\epsilon}_s(\mathbf{k}) = \left[\mathbf{D}(\mathbf{k}) - \frac{1}{m}\partial_{\mathbf{X_i}}\mathbf{C}(\mathbf{X}_i)\right]\boldsymbol{\epsilon}_s(\mathbf{k})\,, \quad s = 1,2,3 \tag{3.2}$$

3.1.1 Dynamical Matrix of the 2D Plasma Crystal

The dynamical matrix for the non-reciprocal interactions of the point-like wake model will be complex and non-hermitian as shown in Sec. 2.2.2.
For the case of a 2 dimensional lattice (in equilibrium) all particles occupy the same z-position which can be therefore set to zero without loss of generality. Using the linearized point-like wake model as defined in Sec. 2.1.3 the dynamical matrix has the general shape given by

$$\mathbf{D}(\mathbf{k}) = \begin{pmatrix} \alpha_x & \alpha_{xy} & i\sigma_x \\ \alpha_{xy} & \alpha_y & i\sigma_y \\ i\sigma_x & i\sigma_y & \alpha_z \end{pmatrix} \tag{3.3}$$

The components are determined by Jacobian matrix of the point-like wake force according to

$$\begin{aligned}
\alpha_x &= -\Omega_{DL}^2 2 \sum_{\mathbf{X}_j \neq 0} [a_j + x_j^2 b_j] \sin^2\left(\frac{1}{2}\mathbf{k}\mathbf{X}_j\right), \quad \alpha_{xy} = -\Omega_{DL}^2 2 \sum_{\mathbf{X}_j \neq 0} [y_j x_j b_j] \sin^2\left(\frac{1}{2}\mathbf{k}\mathbf{X}_j\right) \\
\alpha_y &= -\Omega_{DL}^2 2 \sum_{\mathbf{X}_j \neq 0} [a_j + y_j^2 b_j] \sin^2\left(\frac{1}{2}\mathbf{k}\mathbf{X}_j\right), \quad \sigma_x = -\Omega_{DL}^2 \delta \sum_{\mathbf{X}_j \neq 0} [x_j c_j] \sin\left(\mathbf{k}\mathbf{X}_j\right) \\
\alpha_z &= -\Omega_{DL}^2 2 \sum_{\mathbf{X}_j \neq 0} [a_j + \delta^2 b_j] \sin^2\left(\frac{1}{2}\mathbf{k}\mathbf{X}_j\right), \quad \sigma_y = -\Omega_{DL}^2 \delta \sum_{\mathbf{X}_j \neq 0} [y_j c_j] \sin\left(\mathbf{k}\mathbf{X}_j\right)
\end{aligned} \tag{3.4}$$

where the sum runs over all points of the equilibrium lattice $\mathbf{X}_j = (x_j, y_j, z_j)^T$. The functions $a_j = a(\mathbf{X_j})$, $b_j = b(\mathbf{X_j})$, $c_j = c(\mathbf{X_j})$ are the same as defined for the Jacobian matrix on page 6.
The dust lattice frequency scale is given as

$$\Omega_{DL}^2 = \frac{Q^2}{m\lambda^3} \tag{3.5}$$

with the dust particle charge Q and the screening length of the Yukawa potential λ and the particle mass m. It is often convenient to normalize the dynamical matrix by the dust lattice frequency scale. The sums in Eq. 3.4 are fully characterized by the exact lattice symmetry and three dimensionless parameters. One screening parameter $\kappa = \Delta/\lambda$ and the two wake parameters $\tilde{q} = |q/Q|$ and $\tilde{\delta} = \delta/\Delta$. With the lattice constant Δ the wake charge q and the wake charge distance δ.

3.1.2 Confinement and Dispersion Relation

The contribution of the confinement can be considered by renaming $\Omega_{conf}^2 = \Omega_z^2$ and replacing $\alpha_z \to \Omega_{conf}^2 + \alpha_z$ inside the dynamical matrix. In summary one has to solve the eigenvalue problem for the modified dynamical matrix $\tilde{\mathbf{D}}(\mathbf{k})$

$$\lambda_s(\mathbf{k})\boldsymbol{\epsilon}_s(\mathbf{k}) = \tilde{\mathbf{D}}(\mathbf{k})\boldsymbol{\epsilon}_s(\mathbf{k}), \text{ where } \tilde{\mathbf{D}}(\mathbf{k}) = \begin{pmatrix} \alpha_x & \alpha_{xy} & i\sigma_x \\ \alpha_{xy} & \alpha_y & i\sigma_y \\ i\sigma_x & i\sigma_y & \Omega_{conf}^2 + \alpha_z \end{pmatrix} \quad s = 1,2,3 \tag{3.6}$$

After that the dispersion relation is obtained by solving $\Omega_s(\mathbf{k}) = +\sqrt{\lambda_s(\mathbf{k})}$.
Taking also friction into consideration the final complex frequencies are are received from $\Omega_s^2(\mathbf{k}) = \tilde{\omega}_s(\mathbf{k})^2 + i\nu\tilde{\omega}_s(\mathbf{k}))$ according to Eq. 2.44.

3.2 Mode-Coupling Mechanism and Instability

3.2.1 Characteristic Polynomial and Terminology

Zhdanonv et al.[35] analysed the eigenvalue problem for the dynamical matrix $\tilde{\mathbf{D}}(\mathbf{k})$ given in Eq. 3.6 by considering the corresponding characteristic polynomial which is given by

$$(\Omega^2 - \Omega_{h+}^2)(\Omega^2 - \Omega_{h-}^2)(\Omega^2 - \Omega_v^2) + \Omega_{coup}^2(\Omega^2 - \Omega_{mix}^2) = 0 \tag{3.7}$$

where the used definitions are

$$\begin{aligned} \Omega_{h\pm}(\mathbf{k}) &= \sqrt{\alpha_h \pm \sqrt{\beta^2 + \alpha_{xy}^2}} \text{ with } \alpha_h = \frac{\alpha_x + \alpha_y}{2},\ \beta = \frac{\alpha_x - \alpha_y}{2} \\ \Omega_v(\mathbf{k}) &= \sqrt{\Omega_{conf}^2 + \alpha_z} \\ \Omega_{coup}^2(\mathbf{k}) &= \sigma_x^2 + \sigma_y^2 \\ \Omega_{mix}^2(\mathbf{k}) &= \alpha_h + \beta\frac{\sigma_y^2 - \sigma_x^2}{\sigma_x^2 + \sigma_y^2} - 2\alpha_{xy}\frac{\sigma_x\sigma_y}{\sigma_x^2 + \sigma_y^2} \end{aligned} \tag{3.8}$$

The coupling term $\Omega_{coup}^2 = \sigma_x^2 + \sigma_y^2 \propto \delta^2$ can be seen as wake mediated coupling for the three branches of normal modes $\Omega_{h\pm}, \Omega_v$ which solve the system for the case of vanishing coupling(i.e. $\delta = 0$).

For the not coupled situation the two "horizontal" modes $\Omega_{h\pm}$ represent a pair of *acoustic in-plane modes*[1]. Ω_{h+} shows *longitudinal* polarization (i.e. $\mathbf{k} \parallel \boldsymbol{\epsilon}_{h+}$) while Ω_{h-} is a *transversal* mode (i.e. $\mathbf{k} \perp \boldsymbol{\epsilon}_{h-}$). The "vertical" mode Ω_v is an *optical* mode and shows as well *transverse* polarization(i.e. $\mathbf{k} \perp \boldsymbol{\epsilon}_v$).

[1] Dispersion relations of crystals show two qualitatively different types of normal mode branches. Acoustic branches grow linearly for small $\mathbf{k}$ vectors i.e. $\omega(k)^{acoustic} = c_s k$ with the speed of sound c_s. While optic branches are typically nearly constant for small $\mathbf{k}$ vectors i.e. $\omega(k)^{optic} = \omega(k = 0) = const.$. For detailed information it is referenced to the standard literature [2].

All in all the not coupled crystal is described by the following picture. The motion inside the crystal plane is described by a superposition of all the acoustic normal modes while the motion orthogonal to the plane is completely decoupled and described by the optic normal modes.

3.2.2 The Coupling Mechanism

As shown in [35] because of the coupling some values of **k** will lead to complex, exponentially growing, solutions and corresponding instabilities while the other do not.
To understand qualitatively how this selection for unstable **k** values is working it is helpful to look at $(\Omega^2-\Omega_a^2)(\Omega^2-\Omega_b^2)(\Omega^2-\Omega_c^2)+\Omega_{coup}^4(\Omega^2-\Omega_{mix}^2)=0$ what leads to the valid relation

$$\Omega^2=\frac{\Omega_a^2+\Omega_b^2}{2}+\frac{1}{2}\sqrt{(\Omega_a^2-\Omega_b^2)^2-4\Omega_{coup}^2\frac{\Omega^2-\Omega_{mix}^2}{\Omega^2-\Omega_c^2}} \tag{3.9}$$

where $\Omega_a^2,\Omega_b^2,\Omega_c^2$ represent arbitrary arrangements of $\Omega_{h\pm}^2,\Omega_v^2$. Without loss of generality it is therefore sufficient to focus on the influence on Ω_a^2 by setting $\Omega^2=\Omega_a^2+\Delta$. Using further the definitions $s(\Delta)=(\Omega_a^2-\Omega_{mix}^2+\Delta)/(\Omega_a^2-\Omega_c^2+\Delta)$ and $\epsilon=4\Omega_{coup}^2/(\Omega_a^2-\Omega_b^2)^2$ Eq. 3.9 can be reformulated to give

$$\Omega^2=\frac{\Omega_a^2+\Omega_b^2}{2}+\frac{\Omega_a^2-\Omega_b^2}{2}\sqrt{1-\epsilon\,s(\Delta)} \tag{3.10}$$

Well separated branches: If now $\Omega_a^2,\Omega_b^2,\Omega_c^2$ are well separated in a sense that their differences are large compared to Ω_{coup}^2 (i.e. $|\Omega_a^2-\Omega_b^2|>>\Omega_{coup}^2$) we have $\epsilon<<1$. Further $s(\Delta)$ is of order 1 if Δ is small compared to the difference $|\Omega_a^2-\Omega_c^2|$, such that the square root can be approximated up to first order, what gives

$$\Omega^2=\Omega_a^2-\epsilon\,s(\Delta)\approx\Omega_a^2-\epsilon\,s(0)\rightarrow\Omega\approx\sqrt{\Omega_a^2-\epsilon\,s(0)} \tag{3.11}$$

where the approximation is consistent because of[2] $s(-\epsilon s(0))=s(0)+\mathcal{O}(\epsilon)$ for small ϵ.

This shows that for the case of well separated modes the influence of the coupling should be only a slight correction but qualitatively the modes should be comparable to the case of vanishing mode coupling.

Crossing branches: Now lets assume $\Omega_a^2\approx\Omega_b^2$. Ω_c^2 shall be separated from $\Omega_{a,b}^2$, in the sense that the distance is large compared to Ω_{coup}^2. In this situation we have $\epsilon=1$ if $(\Omega_a^2-\Omega_b^2)^2=4\Omega_{coup}^2$ and further $\epsilon>>1$ if $\Omega_b^2\rightarrow\Omega_a^2$.

[2] When solving the fix-point equation $\Delta_{n+1}=-\epsilon s(\Delta_n)$ this implies a correction of $\mathcal{O}(\epsilon^{n+1})$ for the nth step. The error of the approximation $\Delta_1=-\epsilon s(0)$ should be therefore of $\mathcal{O}(\epsilon^2)$ and hence $\frac{|\Delta_2-\Delta_1|}{|\Delta_1|}\approx\epsilon<<1$

The behavior of $\sqrt{1-\epsilon\, s(\Delta)}$ depends now critically on the sign of $\epsilon\, s(\Delta)$ if it approaches 1 from below ($|\epsilon\, s(\Delta)| \to 1^-$).

- For $s(\Delta) < 0$ there are still only real solutions however the corrections to the not coupled modes may be significant. Since this case is not of interest during this thesis, it is not further discussed.

- For $s(\Delta) > 0$ the solution and $s(\Delta)$ itself become complex. To be precise, since the characteristic polynomial (Eq. 3.7) has only real coefficients, a pair of complex conjugated solutions appears[3] (compare also Fig. 3.1). Assuming an comparable small imaginary part from Eq. 3.9 it can be seen that this solutions are roughly given by $\Omega^2 \approx \frac{\Omega_a^2+\Omega_b^2}{2} \pm i\Omega_{coup}\sqrt{|s(\Delta)|}$.
  This leads to the formation of a so called *hybrid mode* which can be obtained by solving for Ω and results in a pair of branches with identical real part and complex conjugate imaginary parts

$$\mathrm{Re}(\Omega_{hyb}) \approx \sqrt{\frac{1}{2}(\Omega_a^2+\Omega_b^2)}\,,\ \ \mathrm{Im}(\Omega_{hyb}) \approx \pm\frac{1}{2}\left(\frac{\Omega_{coup}\sqrt{|s(\Delta)|}}{\mathrm{Re}(\Omega_{hyb})}\right) \tag{3.12}$$

  For the case of comparable weak friction (i.e. $Re(\Omega_{hyb}) >> \nu$) one gets the complex frequency of the plane wave solutins $\tilde{\omega}_{hyb} = \omega_{hyb} + ig_{hyb}$ from Ω_{hyb} in good approximation by taking $\Omega_{hyb} - i\nu/2$ such that

$$\omega_{hyb} \approx \sqrt{\frac{1}{2}(\Omega_a^2+\Omega_b^2)}\,,\ \ g_{hyb}^{\pm} \approx \pm\frac{1}{2}\left(\frac{\Omega_{coup}\sqrt{|s(\Delta)|}}{\omega_{hyb}} \mp \nu\right) \tag{3.13}$$

  Consequently dependent on ν there are solutions possible where $\mathbf{d}(t) \propto \exp(g_{hyb}^{\pm}t)$ with $g_{hyb}^{\pm} > 0$ and therefore causing an instability which destroys the crystal.

3.2.3 Symmetric Growth for Both Wave Propagation Directions

In section 2.2.4 it was shown that a positive growth rate $g_{s,\mathbf{k}} > 0$ automatically induces a growth rate $g_{s,-\mathbf{k}} < 0$ for the inverted $\mathbf{k}$-vector. This reflects the asymmetric character of non-reciprocal interactions. However in the case of a 2 dimensional plasma crystal only the z-component of the force shows non-reciprocal character. Therefore the in plane directions $\mathbf{k}$ and $-\mathbf{k}$ should be physically equivalent since also the lattice is point symmetric. This is ensured by the up coming complex conjugated pairs of hybrid modes. To be exact if we have the three branches $s = a, b, c$ and a, b show coupling while c is well separated the complex frequencies ($\tilde{\omega}(\mathbf{k}) = \omega_s(\mathbf{k}) + ig_s(\mathbf{k})$) of the three branches are given by $\tilde{\omega}_c(\mathbf{k}) = \omega_c(\mathbf{k}) - i\nu/2$ and $\tilde{\omega}_b(\mathbf{k}) = \omega_{hyb}(\mathbf{k}) + ig_{hyb}^{+}$ or $\tilde{\omega}_a(\mathbf{k}) = \omega_{hyb}(\mathbf{k}) + ig_{hyb}^{-}$ respectively. Since we know that the eigenvalues for inverted $\mathbf{k}$-vectors are complex conjugated[4] (i.e. $\lambda_{a/b,\mathbf{k}} = \overline{\lambda_{a/b,-\mathbf{k}}}$)

[3] Standard linear algebra result see [1] for more information.
[4] See Sec. 2.2.4.

it directly follows from the definition of the complex frequency that $\tilde{\omega}_c(\mathbf{k}) = \tilde{\omega}_c(-\mathbf{k})$ and $\tilde{\omega}_b(\mathbf{k}) = \tilde{\omega}_a(-\mathbf{k})$ or $\tilde{\omega}_a(\mathbf{k}) = \tilde{\omega}_b(-\mathbf{k})$ respectively. This shows that for the two different wave propagation directions $\pm\mathbf{k}$ only the role of the two branches a, b is switched. However the resulting growth rates are identical thus that in any direction there is one growing and one decaying mode. In that sense one can consider both directions as physically equivalent.

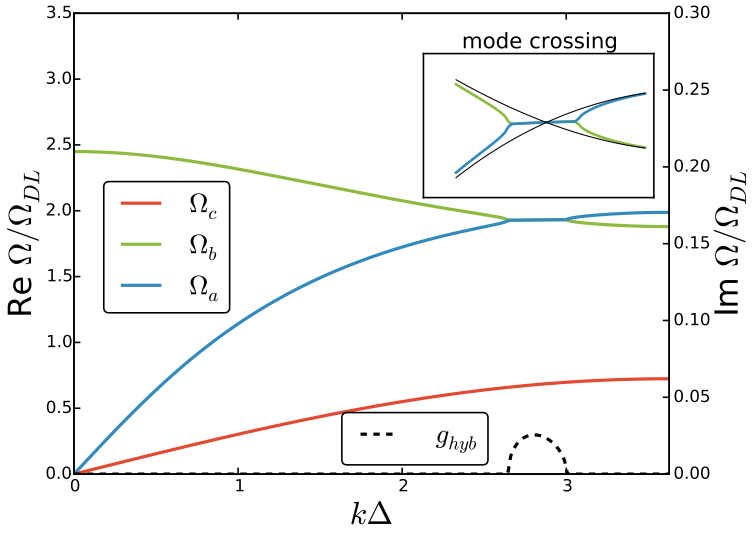

Figure 3.1: Example for the *mode-coupling instability*, the two branches Ω_a and Ω_b approach each other and form a branche of *hybrid modes* with positive growth rate g_{hyb} causing an instability. The magnification window displays the crossing situation. For comparison the uncoupled branches which cross are plotted as fine black lines. It is good to see that both branches lock together at the same hybrid frequency ω_{hyb} when they come close to each other. The positive growth rate is plotted as black dashed line. For all the other $\mathbf{k}$ vectors where the branches are separated the solutions are ordinary oscillations.

3.2.4 Selection of Growing Normal Modes

The described coupling mechanism of the mode coupling instability can be interpreted as selection of excited $\mathbf{k}$ vectors in the following way.

For some $\mathbf{k}$ vectors where two branches of the dispersion relation cross or become approximately identical the corresponding normal mode solution may show complex frequencies $\tilde{\omega} = \omega_{hyb} + i g_{hyb}$ causing exponential growth. In contrast for all other $\mathbf{k}$-vectors the normal modes remain stable. In this sense this can be interpreted as selection of exponentially growing $\mathbf{k}$ vectors.
Consequently the particle motion during the mode coupling induced melting process is naturally subjected the motion typical for the normal modes of the selected $\mathbf{k}$ vectors. A typical example is given in Figure 3.1.

3.3 Mode-Coupling for the Perfect Hexagonal Crystal

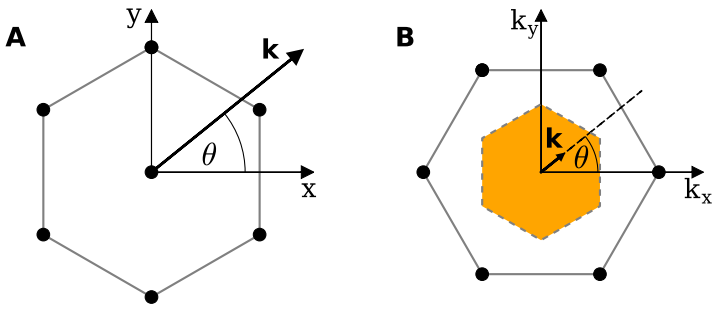

Figure 3.2: Elementary hexagonal lattice cell of the real lattice (A) and the corresponding reciprocal lattice (B) for the perfect hexagonal structure[5]. The 1st Brillouin zone is given as orange area in the **k**-space. The angle θ shall be measured anticlockwise with respect to the positive x-axis. It is used to denote the direction of **k**-vectors.

The mode-coupling properties for the 2 dimensional plasma crystal of perfect hexagonal structure as given in Figure 3.2 was first analysed by Zhdanov et al. in [35] and is described in great detail in [6].
In the following the aspects relevant for this thesis are summarized. $\Omega_{h\pm}$ denotes the pair of acoustic in-plain modes while Ω_v is the optical out-of-plain mode. (For definition look at page 23, Eq. 3.8.)

Control of coupling by variation of Ω_{conf}: Since the vertical out of plane branch is given by $\Omega_v = \sqrt{\Omega_{conf}^2 + \alpha_z}$ its magnitude can be controlled by variation of the confinement. In this way it is possible to determine the coupling behaviour, i.e. for which **k** vectors the branches approach each other. In Figure 3.3 the situation representing typical experimental situations [5, 24] is shown for the perfect crystal. For sufficient large confinement the crystal is stable and no mode-coupling occurs. If Ω_{conf} is lowered the branches approach each other and finally for the longitudinal in plane mode Ω_{h+} and the vertical out of plain mode Ω_v the branches cross and form a branch of hybrid modes. The coupling occurs first for $\theta = 0°$ near the edge of the 1st Brillouin zone. If the confinement is further lowered a hybrid mode is also formed for other directions (compare also Figure 3.4).

Relevance of longitudinal in-plane mode: From definition in 3.8 on page 23 it is clear that $\Omega_{h+} \geq \Omega_{h-}$. Furthermore for the stable crystal one has $\Omega_v > \Omega_{h+}$ for the stable crystal. Therefore the branches of the longitudinal in plane mode and transversal out of plain mode Ω_v approach always at first. Since they show positive coupling (i.e. $s(\Delta) > 0$) they form a hybrid mode. Hence the coupling between these two modes triggers the instability in experiments and simulations.

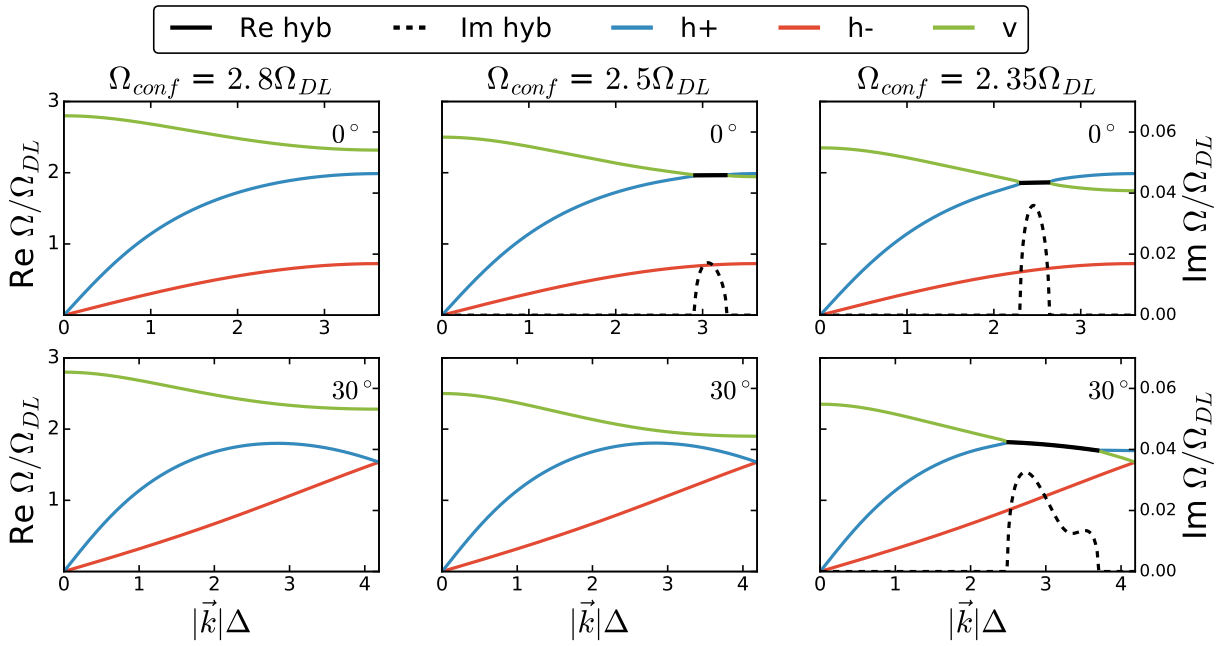

Figure 3.3: Dispersion relation of the perfect hexagonal crystal for the directions $\theta = 0°$, $30°$ and the 3 different confinement strengths $\Omega_{conf} = 2.8$, 2.5, 2.35 in units of Ω_{DL}. The used dimensionless parameters for calculation of the dynamical matrix are $\tilde{\delta} = 0.24$, $\kappa = 1.25$ and $\tilde{q} = 0.2$. It is good to see that mode-coupling occurs first for $\theta = 0°$ and that the branches $h+$ and v couple.

Polarization of the hybrid mode: The polarization of the hybrid mode is elliptical. The coupling occurs between the longitudinal in plane and the transversal out of plane mode. These modes describe motion parallel to the $\mathbf{k} = k(\cos\theta, \sin\theta, 0)^T$ vector and motion orthogonal to the crystal plan in z-direction respectively. Hence it seems to be the natural to assume the resulting motion taking place in the plane spanned by these two axes. Indeed this is true [35]. The in crystal plane motion orthogonal to $\mathbf{k}$ seems to be mostly decoupled and not affected by the instability[7]. To the best of my knowledge an exact solution of the polarization vectors for arbitrary directions is not available. However for the $\theta = 0$ direction is solvable because of the algebraic decoupling of the Ω_{h-} branch[25]. Taking these analytic solution as guiding picture the hybrid polarization vector for the exponentially growing solution can be assumed to be $\boldsymbol{\epsilon}^+_{hyb} = (\sin\theta e^{i\alpha_0}, \cos\theta e^{i\alpha_0}, 1)^T/\sqrt{2}$. Such that the local growing motion induced by the hybrid mode would be described as

$$\mathbf{d}_i(t) = 2\mathrm{Re}\left\{\boldsymbol{\epsilon}^+_{hyb} e^{-i\omega_{hyb}t + g_{hyb}t}\right\} = \sqrt{2}e^{g_{hyb}t}\begin{pmatrix} \cos\theta\cos(\omega t - \mathbf{k}\mathbf{X}_i - \alpha_0) \\ \sin\theta\cos(\omega t - \mathbf{k}\mathbf{X}_i - \alpha_0) \\ \cos(\omega t - \mathbf{k}\mathbf{X}_i) \end{pmatrix} \tag{3.14}$$

Most important is the qualitative insight that hybrid modes induce exponentially growing motion always parallel to the $\mathbf{k} = k(\cos\theta, \sin\theta, 0)^T$ vector.

Sixfold symmetry: Because the hexagonal lattice and the interaction forces are symmetric under rotations by angles which are multiples of 60° the same symmetry holds for the dispersion relation. In other words if $\mathbf{k}$ shows positive coupling the vector $\tilde{\mathbf{k}}$ which is rotated by a multiple of 60° shows the exact same positive growth rate [15]. This can be seen on Figure 3.4 where the positive imaginary parts for all branches of the dispersion relation is shown for the whole 1st Brillouin zone.

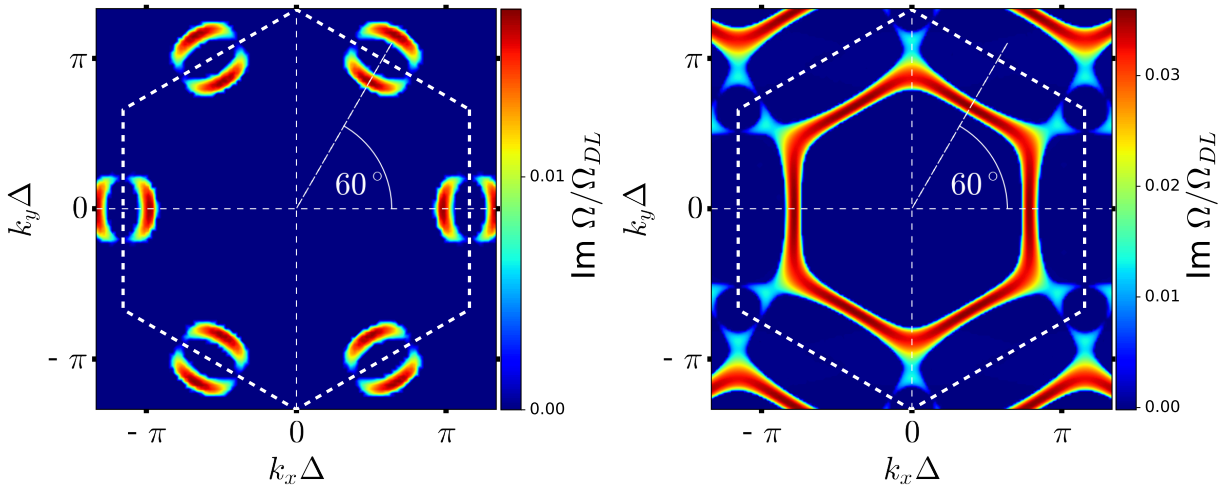

(i) $\Omega_{conf} = 2.5\Omega_{DL}$ (ii) $\Omega_{conf} = 2.35\Omega_{DL}$

Figure 3.4: Dispersion relation for the positive imaginary parts of the complex frequencies for the whole 1. Brillouin Zone. Its boundaries are plotted as dashed white hexagon. For $\Omega_{conf} = 2.5\Omega_{DL}$ it is good to see that the mode-coupling occurs first for $\theta = 0°$ and directions equivalent with respect to the sixfold symmetry of the crystal. For a further lowered confinement ($\Omega_{conf} = 2.35\Omega_{DL}$) all directions show mode-coupling for $\mathbf{k}$ vectors of approximately same modulus. The system is characterized by $\tilde{\delta} = 0.24$, $\kappa = 1.25$ and $\tilde{q} = 0.2$.

Hot spots: The typical situation considered in this thesis is shown in Figure 3.4(i) where the positive growth rates appear in small *hot spots* of the $\mathbf{k}$-space. These hot of the dispersion relation coincide with hot spots found in the so called *particle fluctuation spectra* of experimental or simulated data. It is calculated from the particle current [10] of the longitudinal in-plane motion which is defined as

$$V(\mathbf{k}, t) = \sum_j v_j^{\mathbf{k}} e^{-i\mathbf{k}\cdot\mathbf{x}_j} \tag{3.15}$$

where $v_j^{\mathbf{k}}$ is the component of the particle velocity parallel to $\mathbf{k} = (k_x, ky)^T$. The particle current fluctuation spectra is calculated by Fourier transforming the particle current, i.e. $V(\mathbf{k}, t) \rightarrow V(\mathbf{k}, \omega)$. To show the spectra in the $k_x k_y$-plane $V(\mathbf{k}, \omega)$ is integrated over a frequency range containing the hybrid frequency[19].

3.4 Mode-Coupling for the Deformed Hexagonal Crystal

The influence of deformation on the dispersion relation and the associated mode-coupling instability was described in great detail by Ivlev et al. in [15].
In principle the results are quite similar to the not deformed case. There is however one important modification which results in qualitative different system properties. Particularly, due to the deformation the lattice has lost its sixfold symmetry and one can ensure only point symmetry. In consequence also the dispersion relation has to be only point symmetric (i.e. under rotations by 180°). Hence it is now possible to observe the onset of mode coupling for only one direction of motion or with different growth rates along different symmetry axes. As rule of thumb the mode coupling occurs faster for directions which are contracted and show a higher density. In Figure 3.5 two examples are given. The corresponding lattices are shown in Figure 3.6.

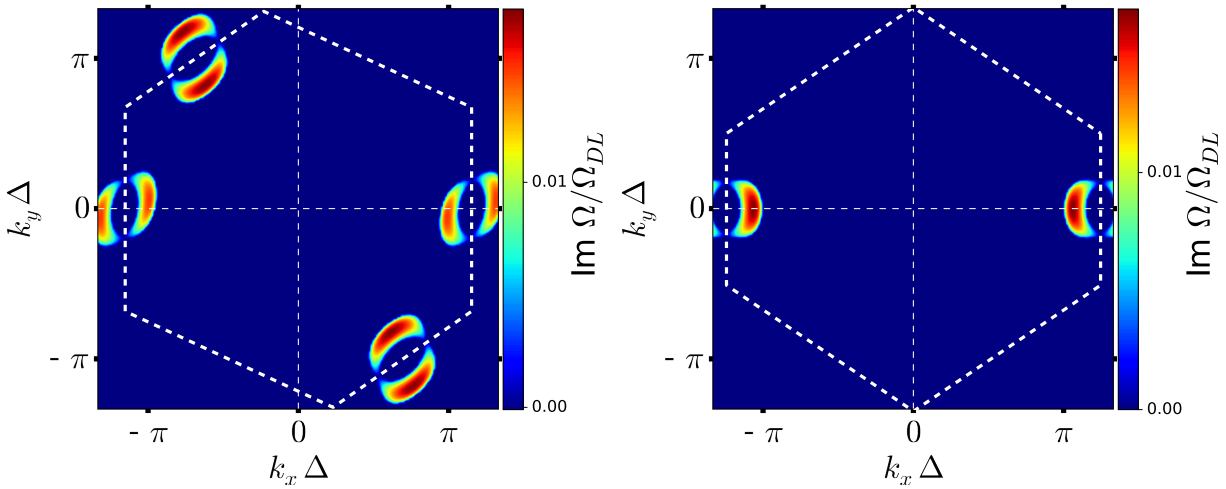

(i) $\Omega_{conf} = 2.5\Omega_{DL}$, $\tau = 0.1$ (ii) $\Omega_{conf} = 2.55\Omega_{DL}$, $\mu = 0.9$

Figure 3.5: Dispersion relation for the imaginary part of the complex frequency for the whole 1. Brillouin Zone in deformed case. The boundaries of the 1. BZ are plotted as dashed white hexagon in each case. For pure share (ii) only **k** vectors in x-direction show hybrid coupling. For simple share (i) one sees hybrid modes emerge for two directions with different growth rates. For the not deformed crystal the sixfold symmetry would not allow to obtain such direction dependent triggering of the MCI. The system is characterized by $\tilde{\delta} = 0.24$, $\kappa = 1.25$ and $\tilde{q} = 0.2$.

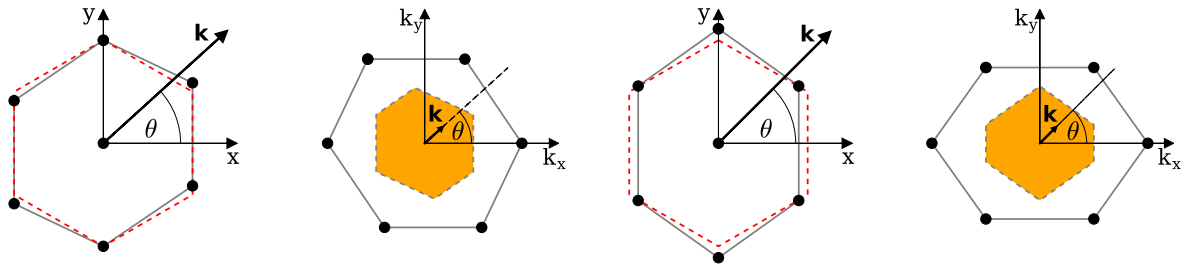

(i) Simple share for the strain $\tau = 0.1$. (ii) Pure share for the contraction factor $\mu = 0.9$.

Figure 3.6: Elementary deformed hexagonal lattice cells in real space and corresponding reciprocal lattice in **k**-space. The 1st Brillouin zones are given as orange area of the **k**-space. In (a) the lattice is deformed under simple share while in (b) it is deformed under pure share.[6] For comparison the perfect not deformed lattice is drawn in both cases as dashed red hexagon. The angle θ shall be measured anticlockwise with respect to the positive x-axis. It is used to denote the direction of **k**-vectors.

Chapter 4

Synchronization of Particle Motion During MCI

4.1 Experimental Observation

In [7] Couëdel et al. reported the experimental observation of synchronized particle motion during mode-coupling induced melting of a 2 dimensional plasma crystal. They observed alternating stripes of phase and frequency synchronized particle oscillations identical to those in Figure 4.1. It was shown that the orientation of the synchronization patterns correlates with the directions of maximal growing hybrid modes, indicated by hot-spots in the particle velocity fluctuation spectra. Therefore it was supposed that the synchronization patterns could be explained by properties of the dominant wave modes at the hybrid frequency, which have a positive growth rate while the others are suppressed by damping. Simultaneously a connection to the theory of nonlinear coupled limit-cycle oscillators was assumed since *"a two-dimensional plasma crystal can be seen as an ensemble of coupled nonlinear oscillators."*([7], page 1). Along these lines of thinking a nonlinear coupling between the particles shall be a second crucial ingredient for the synchronization which connects the problem to the theory of synchronizing phase oscillators[1].

4.2 MD-Simulations and Order Parameter

The Synchronization was further studied by Laut et al. in [19] where they presented molecular dynamic (MD) simulations which reproduced the experimental results very accurate. Further the role of the anisotropic confinement was clarified. It operates as symmetry breaking mechanism determining the orientation of the stripe pattern (see Figure 4.1). For the further investigation of the process during this thesis the results of this molecular dynamic simulations ([19]) are used as basis. They will be termed as *reference simulations*. Also the method for phase calculation and the order parameter presented in [19] were used.

[1] See Sec. 5

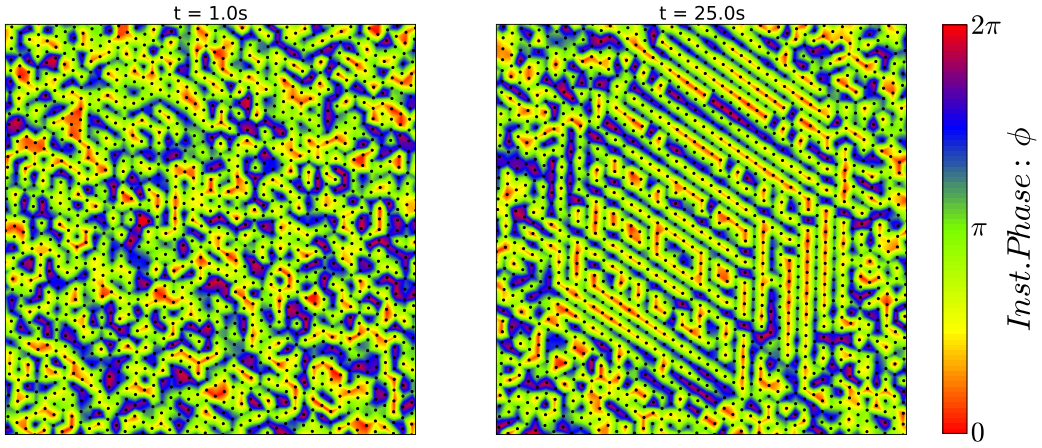

Figure 4.1: Typical synchronization pattern observed during MCI induced melting of a 2D plasma crystal. The case of compression under $\alpha = 30°$ is shown. Data taken from MD simulations published in [19], with kind permission of I.Laut. For $t = 1.0s$ we see randomly distributed phases. In contrast for $t = 25.0s$ the phases from a synchronized stripe pattern.

Hence in the following the relevant results and methods are summarized. At some points, also the data of the reference simulations [19] will be evaluated for comparison. This is done with kind permission of I.Laut. For clarification it shall be pointed out that these data was created by I.Laut.

The confinement

The reference Simulations were done based on the model system presented in Sec. 2 assuming a interaction according to the point-like wake model. Of special interest is the used anisotropic confinement ($\mathbf{C}(\mathbf{x}_i)$) which allows to study a plasma crystal under controlled deformation.

$$\frac{\mathbf{C}(\mathbf{x}_i)}{m} = \begin{pmatrix} \Omega_S^2 x_i \\ \Omega_S^2 y_i \\ \Omega_z^2 z_i \end{pmatrix} - \begin{pmatrix} \Omega_A^2 (x_i cos(2\alpha) + y_i sin(2\alpha)) \\ \Omega_A^2 (x_i sin(2\alpha) - y_i cos(2\alpha)) \\ 0 \end{pmatrix} \tag{4.1}$$

The angle α (measured anticlockwise from the x-axis) determines the orientation of deformation. $\Omega_{||}$ acting in the direction of α and $\Omega_\perp$ perpendicular to it determine the magnitude of deformation since the asymmetric part (A) and symmetric part (S) of the confinement are given by $\Omega_A^2 = (\Omega_{||}^2 - \Omega_\perp^2)/2$ and $\Omega_S^2 = (\Omega_{||}^2 + \Omega_\perp^2)/2$. The vertical confinement in z direction given by $\Omega_z = 2\pi f_z$ is crucial for the stability of the crystal and may trigger the mode-coupling-instability if lowered beneath some critical value.

Phase calculation

The phase of particle i denoted by $\phi_{i,\Theta}$ was calculated by projection of the particle position $\mathbf{x}_i(t) = (x, y, z)^T$ onto the direction denoted by the angle Θ measured anticlockwise from the positve x-axis. To be exact if $\mathbf{n}_\Theta = (\cos(\Theta), \sin(\Theta), 0)^T$ the projection was calculated as $p_{i,\Theta}(t) = \mathbf{n}_\Theta \cdot \mathbf{x}_i(t)$. After that $\phi_{i,\Theta}$ was assumed to grow linearly in time from 0 to 2π between two maxima of $p_{i,\Theta}(t)$. In [7] were the experimental observation was published the phases were calculated from a Hilbert transform of the particle displacement $r(t) = \sqrt{x^2(t) - y^2(t)}$. However both methods seem to produce comparable results. For convenience only the first "projection method" is used during this thesis.

For the moment this definition of phase shall be motivated by the well known physical picture of the 1 dimensional oscillating position variable [9] $x(t) \propto \sin(\phi(t)) = \sin(\omega t)$, with the frequency $\omega = 2\pi/T$ and period T. The phase for such kind of oscillations grows naturally linear in time form 0 to 2π between two maxima of $x(t)$. The issue of phase will be investigated in greater detail in Sec. 5.

Order parameter

To quantify the degree of synchronization the following local order parameter was proposed

$$R_{i,\theta}(t) = \frac{1}{6}\left(\sum_{j=1}^{6}[(-1)_j^k \cos(\phi_{j,\Theta} - \phi_{i,\Theta})]\right) \tag{4.2}$$

where $\phi_{i,\Theta}$ is the phase of particle i calculated by projection onto the direction Θ. The sum runs over all next neighbours j of the hexagonal lattice. $k_j = 0$ if particle j is on the line through particle i perpendicular to the direction given by θ and $k_j = 1$ otherwise[2] Such defined one has $R_{i,\theta} = 1$ for stripes of alternating oscillations aligned orthogonal to θ (i.e. for a phase difference of π between two adjacent stripes). The global order of the system is calculated by averaging $R_{i,\theta}(t)$ over all N particles i such that

$$R_\theta(t) = \sum_{i=1}^{N} R_{i,\theta}(t)/N \tag{4.3}$$

It should be pointed out that θ denotes the direction orthogonal the assumed stripes while Θ denotes the direction of projection for the phase calculation. In many cases both are chosen to be identical but not always.

[2]Two particles are considered to be on the same line if the angle between the i-j bond enclosed with the line through i perpendicular to θ is smaller than 30°[19].

Results of Reference Simulations

The influence of deformation on the observed synchronization pattern was studied in [19] for the two cases of compression under $\alpha = 30°$ and $\alpha = 0°$. In each case the simulations were separated in 3 stages.

- In a first step a stable crystal was formed for $f_z = 23\text{Hz}$ and $\Omega_{||} = \Omega_{\perp}$.
- In a second step the crystal was deformed by changing the confinement to be anisotropic i.e. $0.88\Omega_{||} = \Omega_{\perp}$ for the respective angles of $\alpha = 30°$ and $\alpha = 0°$. This causes the system to equilibrate in a new deformed lattice.
- Finally the confinement is reduced to $f_z = 20\text{Hz}$ what triggers the mode-coupling instability, this moment corresponds to $t = 0$. From now on the energy of the crystal motion grows until the crystal melts. During this process the synchronization patterns were observed.

The main results are shown in Figure 4.2. For the phase calculation in [19] the positions were always projected onto the direction orthogonal to the assumed stripes, i.e $\Theta = \theta$. As can be seen the order parameter for 0° and 60° has detected stripes in case $\alpha = 30°$ (i on Figure 4.2). This can be confirmed by visual inspection of Figure 4.1. For compression under $\alpha = 0°$ (ii on Figure 4.2) stripes are detected only by the order parameter for the 0° direction.
The integrated particle current fluctuation spectra[3] (Figure 4.2(c)) show a clear coincidence for both cases. To be exact stripes are always detected orthogonal to the hot spot directions in the particle fluctuation spectra.

[3] See page 29 for definition of particle fluctuation spectra.

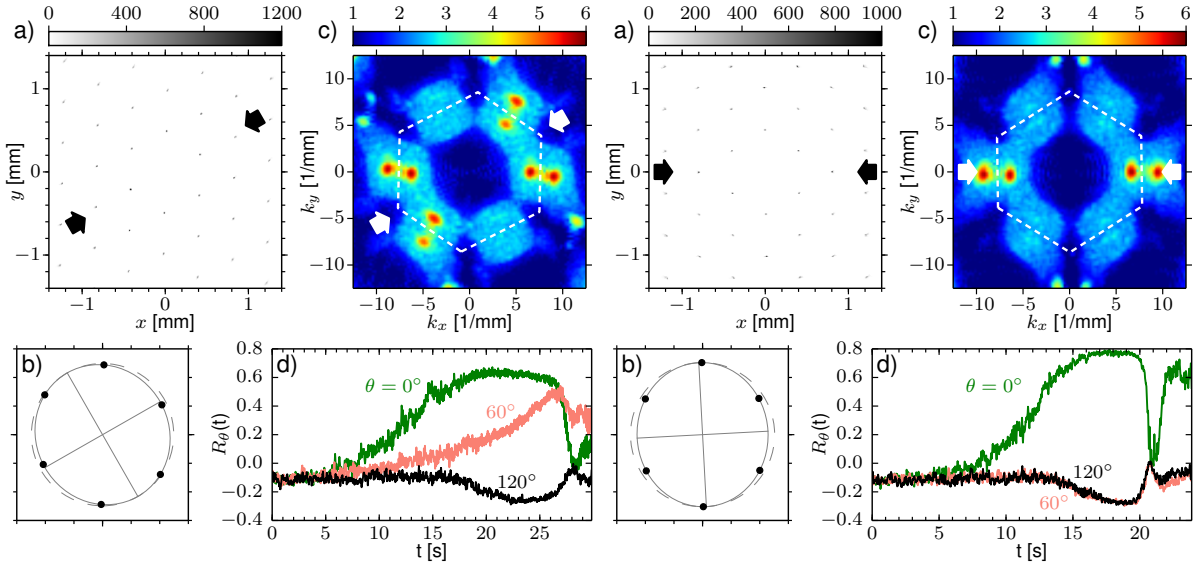

(i) $\alpha = 30$ (ii) $\alpha = 0$

Figure 4.2: Plots taken from [19] with kind permission of I.Laut. The direction of strongest compression is indicated by the arrows. For both cases the resulting deformed lattice[4] is shown in a), b). The integrated particle current fluctuation spectrum is given in c) and the order parameter defined in Eq. 4.2 is shown in d). For $\alpha = 0$ (ii) stripes are detected aligned orthogonal to the x-direction. For $\alpha = 30$ (i) stripes are detected for the 2 directions orthogonal to x-axis and orthogonal to the 60° direction. Both observations correlate well with the observed hot spots in the particle fluctuation spectra.

4.3 Qualitative Interpretation by Properties of MCI

As proposed in [7] the domination of hybrid modes could be a possible explanation for the observed synchronization. However the role of nonlinear influences of the interaction beyond the linear mode theory remains diffuse. In this section we motivate that by applying the purely linear theory of mode-coupling instability the observed synchronization may be explained. Using the properties of the mode-coupling instability presented in chapter 3 the reasoning is given in the following. Beforehand it shall be mentioned that it was tried to explain the necessary ideas in the most easiest way for the sake of readability. All of the used was presented in previous parts of the thesis.

Domination of motion by growing normal modes: In case of MCI only a small fraction of normal modes near the crossing of two branches (see page 26) shows a positive growth rate ($g > 0$) such that particle motion grows exponentially according to $\mathbf{d}(t) \propto \exp(gt)$. All the other $\mathbf{k}$-vectors are well suppressed by damping, i.e. $0 > g \approx -\nu/2$ such that $\mathbf{d}(t) \propto \exp(-\frac{\nu}{2}t)$. Consequently one may expect that the properties of the growing modes dominate the resulting motion of the crystal during mode-coupling induced melting.

Frequency synchronization: The observed synchronization occurs for a confinement strength not far below a stable configuration. In such situations mode coupling typically appears in regions near the edges of the 1st Brillouin zone where the crossing branches are comparable flat (compare page 28). Therefore the hybrid frequency is nearly identical for all hybrid modes and shall be denoted as ω_{hyb}. Hence the dominating motion can be expected as linear superposition of normal modes with identical real frequency $\omega = \omega_{hyb}$. This leads automatically to frequency synchronization.

Phase synchronization: In the same way for confinement strengths not far below a stable configuration the hybrid $\mathbf{k}$-vectors are located in small "hot spots" near the edge of the 1st Brillouin zone (see Figure 3.4 on page 29). Focusing on one "hot spot" we can approximate its $\mathbf{k}$-vectors with positive growth rate by the central one $\mathbf{k}_{hyb}$. For plane waves ($\mathbf{d}(t) \propto \exp(-\omega t + i\mathbf{k}\cdot\mathbf{X}_i)$) this wave vector induces a position dependent phase shift $\Phi(\mathbf{X}_i) = \mathbf{k}_{hyb}\cdot\mathbf{X}_i$ for particle i with equilibrium position $\mathbf{X}_i$. The properties of the dot product automatically lead to the formation of stripes with identical phase shift Φ orthogonal to the direction of $\mathbf{k}_{hyb}$. This coincides well with the observation of stripe formation always orthogonal to the hot spot directions. Since hot spots always appear as pairs for both wave propagation directions $\pm\mathbf{k}$, it shall be mentioned that both directions imply the same symmetry (alignment of stripes). Thus we can focus on "hot spot pairs" inducing the same stripe direction.

Destroyed symmetry by deformation: For the not deformed hexagonal crystal the sixfold symmetry leads to 3 pairs of hot spots with identical growth rates. Hence different directions of stripes overlap what prevents a visible pattern. However for a deformed lattice the sixfold symmetry of the dispersion relation is not given (see page 30) and stripes caused by only one hot spot pair are possible. And even for stripes in more than one direction the growth rates are not necessarily identical such that one direction may dominate.

This reasoning shows that the observed synchronization may be a purely linear phenomenon. Indeed this is the case as will be shown in the following parts. This motivating reasoning is intended to provide a simple guiding picture for interpretation of the following results. A detailed explanation of the synchronization aspects such as the phase difference between adjacent will be given step by step.

4.4 Comparison of Linear and Nonlinear Interactions

As motivated in the last section the synchronization process may be a purely linear phenomenon. However to ensure independence of the phase synchronization on nonlinear effects one has to find a way to verify the linearity. One way to address this question would be to compare the nonlinear system to its linear equivalent. In order to achieve such a comparison a stable crystal was assumed and the interaction force was linearized around the equilibrium configuration of the crystal in the same way as for the calculation the dispersion relation[5]. The linear and the nonlinear system were solved numerically in two separate integration runs for identical lattice and system configuration. Consequently all differences between both systems reflect the nonlinear character of the interaction.

4.4.1 Definitions an Method

Considered Cristal Symmetries

For the reference molecular dynamic simulation [6] a system of 16384 particles was simulated. However only a small region of nearly homogenous lattice structure in the center of the crystal showed the synchronization patter. As can be seen on Figure 4.1(on page 34) this region is about 40 lattice constants in diameter. Motivated by this observation a perfect crystal of comparable finite extend was assumed as model crystal to compare the linear with the nonlinear time evolution.
To obtain results comparable to the observed cases of synchronization in the reference simulations it is necessary to assume a Bravais lattice reflecting the correct symmetry. As presented in Sec. 2.3.2 a deformed hexagonal lattice can be characterized by the deformation matrix

$$\mathbf{T} = \begin{pmatrix} \mu & 0 \\ m & \mu^{-1} \end{pmatrix} \tag{4.4}$$

where μ is the contraction factor and m is the share slope. Consequently it is necessary to find m, μ and the lattice constant Δ from data of the reference simulations. For this purpose the first maxima of the particle pair correlation[7] (calculated for the homogenous central part of the simulated crystal) where assumed as next neighbours from which it is easy to derive the necessary parameters m, μ and Δ.

In that way the following parameters where derived for the two cases $\alpha = 0°$ and $\alpha = 30°$.

	m	μ	Δ
$\alpha = 0°$	0	1.0479	480 μm
$\alpha = 30°$	-0.0646	1.0142	480 μm

[5] Compare Sec. 2.2
[6] See Sec. 4.2.
[7] For more information it is referenced to [19]

It shall be mentioned that both situation lead to the same lattice constant what may be interpreted as hint that the description of the deformed lattice in terms of **T** and the derived parameters are quite accurate. The positive μ for both cases indicates that the lattice is compressed or contradicted along the x-axis and extended into the y-direction. The negative m for $\alpha = 30°$ shows that particle rows of identical x-position are shifted against each other. Both situation are shown in Figure 4.3.

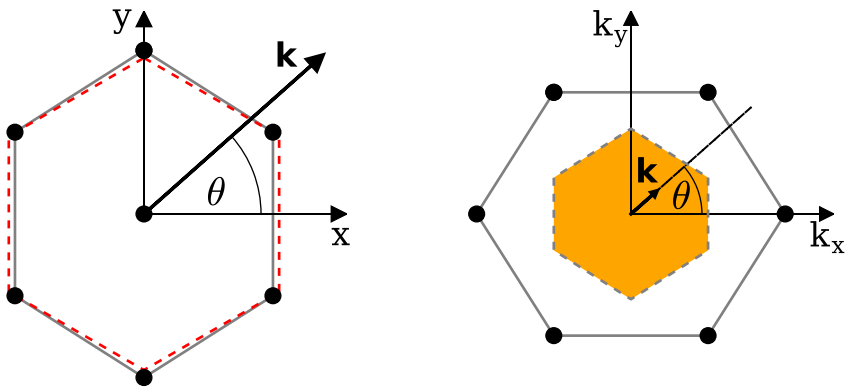

(i) Lattice for the case of deformation characterized by $\alpha = 0°$.

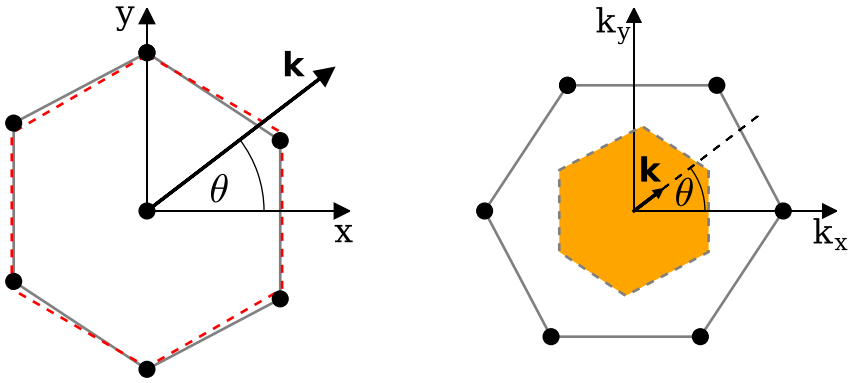

(ii) Lattice for the case of deformation characterized by $\alpha = 30°$.

Figure 4.3: Two resulting deformed hexagonal lattice structures. The not deformed hexagonal lattice is shown as dashed red hexagon in real space. The deformation is drawn to scale. All upcoming angles are measured in the same way as θ anticlockwise with respect to the x-axis.

Boundary Conditions

Probably the most common boundary conditions for considerations of crystals are periodic boundaries. However for the situation of interest periodicity of motion seem to be a wrong assumption. Since only a small homogenous and unstable region in the center of the crystal shows the synchronization. This region is surrounded by a much bigger slightly different stable crystal. Therefore a infinite crystal was assumed and a finite area of desired shape was picked out. In the following the set of all indices denoting particles inside this area is denoted as A. During the simulations it was assumed that only particles inside this area move (where $i \in A$), while all others are fixed to the equilibrium position. Further a finite interaction range was assumed such that the surrounding of the area of interest was limited and the system was solvable by numerical integration. For this thesis a circular and a quadratic system were considered. Both are represented in Figure 4.4 schematically.

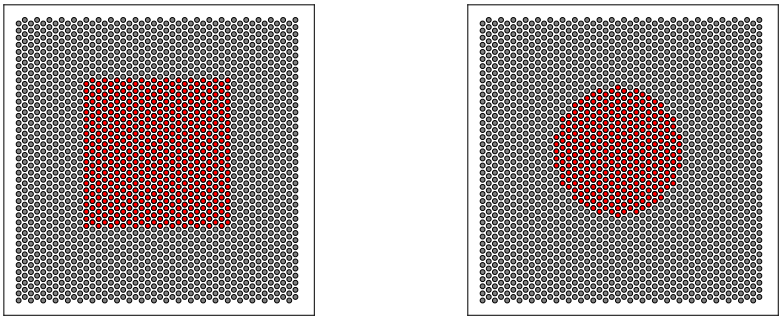

Figure 4.4: Schematic representation of used boundary constraints for the simulated systems. For this thesis a circular and a quadratic system was considered. Only for the red positions of the shown lattices motion is allowed. All other particles are fixed to its equilibrium position.

Number of particles: As already mentioned the system size was chosen to be comparable to the area of synchronized particle motion in the reference simulations. This area was approximately 40 lattice constants in diameter. For the quadratic system in case of $\alpha = 0°$ the system was containing $N = 2000$ moving particles and for the case $\alpha = 30°$ the system was containing $N = 1880$ particles. The circular system was only considered for $\alpha = 30°$ which was simulated for a moving particle number $N = 1476$

Formulation and Numerical aspects

System parameters: As already mentioned a perfect crystal was assumed. The equilibrium positions derived in the way described above shall be denoted as $\mathbf{X}_i$. Other system parameters were assumed to be identical to the reference simulations[19]. All parameters are listed in the following table.

lattice constant :	$\Delta = 480\mu m$	particle mass :	$m = 6.1 \times 10^{13} kg$
temperature :	$T = 300K$	screening length :	$\lambda = 380\mu m$
wake charge :	$Q = -19000e$	particle charge :	$q = 0.2\|Q\|$
wake distance :	$\delta = 0.3\lambda$	friction parameter :	$\nu = 1.26/s$

The synchronization patterns were observed for a vertical confinement in z-direction of $f_z = 20Hz$ or $\Omega_z = f_z 2\pi$. Consequently the same confinement was used.

Finite interaction range: For the simulations a finite interaction range of 10 lattice constants was assumed. For each particle i the set n_i contains all interacting particles j such that the equilibrium distance is smaller or equal the interaction range, i.e. $|\mathbf{X}_i - \mathbf{X}_j| \leq 10\Delta$.

Confinement: Since the in-plane stability is given by the assumption of an infinite crystal only a vertical confinement in z-direction is necessary, such that the confinement becomes $\mathbf{C}(\mathbf{x}_i) = -\mathbf{e_z} m\Omega_z^2 z_i$ where $\mathbf{e_z}$ is the unit vector in z-direction. However caused by attraction of the positive wake charges placed at constant distance δ below each particle the crystal equilibrium z-position would be a negative value $(-z_0)$ for this definition of the confinement. For convenience the confinement was therefore rescaled such that

$$\mathbf{C}(\mathbf{x}_i) = -\mathbf{e_z} m\Omega_z^2 (z_i - z_0) \text{ where } z_0 = \frac{\sum_{j \in n_i} \mathbf{F}(\mathbf{R}_{ji})}{m\Omega_z^2} \tag{4.5}$$

With this definition all particles would equilibrate in the $z = 0$ plane. The shift z_0 is the same for every particle. Since in "equilibrium" every particle experiences the same force for the used boundary conditions. ($\mathbf{R}_{ji}$ are the equilibrium distances.)

Equations of Motion: The position of each particle shall be denoted by $\mathbf{x}_i = \mathbf{X}_i + \mathbf{d}_i$ with the equilibrium position $\mathbf{X}_i$ and the deviation $\mathbf{d}_i$. As consequence distance of two particles can is written as $\mathbf{r}_{ji} = \mathbf{x}_i - \mathbf{x}_j = \mathbf{R}_{ji} + \mathbf{d}_i - \mathbf{d}_j$ with the equilibrium distance $\mathbf{R}_{ji}$. Using this representation the equations of motion for the full nonlinear interaction force and ints linearized version can be written as follows. For every particle $i \in A$ we have [8]

full nonlinear interaction model:

$$m\ddot{\mathbf{d}}_i + m\nu\dot{\mathbf{d}}_i = \mathbf{C}(\mathbf{d}_i) + \sum_{j \in n_i \cap A} \mathbf{F}(\mathbf{R}_{ji} + \mathbf{d}_i - \mathbf{d}_j) + \sum_{j \in n_i \cap A^C} \mathbf{F}(\mathbf{R}_{ji} + \mathbf{d}_i) + \mathbf{L}_i(t) \tag{4.6}$$

where $j \in n_i \cap A$ are all moving particles in the interaction range of particle i while $j \in n_i \cap A^C$ are the particles in the interaction range of particle i fixed to the equilibrium position. The linearized version of the equation of motion can be written as

[8] The point-like wake force $\mathbf{F}(\mathbf{r}_{ji})$ and its Jacobian $\mathbf{J}(\mathbf{R}_{ji})$ are defined in Sec. 2.1.1.

linearized interaction model:

$$m\ddot{\mathbf{d}}_i + m\nu\dot{\mathbf{d}}_i = \mathbf{C}(\mathbf{d}_i) + \mathbf{J_0}\mathbf{d}_i - \sum_{j\in n_i\cap A} \mathbf{J}(\mathbf{R}_{ji})\mathbf{d}_j + \mathbf{L}_i(t) \tag{4.7}$$

with $\mathbf{J_0} = \sum_{j\in n_i} \mathbf{J}(\mathbf{R}_{ji})$ which is identical for each particle because of the lattice symmetry. The friction parameter is denoted as ν and the Langevin force $\mathbf{L}_i(t)$ is a random force with the statistical properties of zero mean $\langle L_i^s(t)\rangle = 0$ and $\langle L_i^s(t)L_i^{\hat{s}}(t+\tau)\rangle = 2\nu m k_B T\delta(\tau)\delta_{s,\hat{s}}$. To make both simulations comparable in a deterministic view, the same random trajectory (i.e. the same random seed[9]) was used for the simulations of the linear and nonlinear system.

Algorithm: Probably the most commonly used scheme for numerical integration of Newton's equations of motion is the Verlet method. It is derived using a truncated Taylor expansion of the particle trajectories. However the non-analytic nature of the random forces make such a Taylor expansion formally invalid [11]. For that reason a stochastic version of the Verlet method proposed in [22] was used. If the equations of motion are written as

$$\begin{aligned}\dot{\mathbf{r}}_i(t) &= \mathbf{v}_i(t)\\ \dot{\mathbf{v}}_i(t) &= \mathbf{a}_i(t) - \nu\mathbf{v}_i(t) + \frac{1}{m}\mathbf{L}_i(t)\end{aligned} \tag{4.8}$$

Where $\mathbf{r}_i(t)$ and $\mathbf{v}_i(t)$ are the position and velocity of particle i. $\mathbf{a}_i(t)$ is the acceleration experienced by particle i including all influences except friction and random force. The numerical integration scheme is the following. In a first step one updates the position according to

$$\mathbf{r}_i(t+h) = \mathbf{r}_i(t) + \mathbf{v}(t)bh + \frac{bh^2}{2}\mathbf{a}_i(t) + \frac{bh}{2}C\mathbf{G}(t) \tag{4.9}$$

and in a second the velocities

$$\mathbf{v}_i(t+h) = \mathbf{v}_i(t) + \frac{h}{2}\left[\mathbf{a}_i(t) + \mathbf{a}_i(t+h)\right] - \nu\left[\mathbf{r}_i(t+h) - \mathbf{r}_i(t)\right] + C\mathbf{G}(t) \tag{4.10}$$

h is the time step of the numerical integration, $b = (1+\frac{\nu h}{2})^{-1}$ and C is some kind of noise factor given as $C = \sqrt{(2\nu k_B T h)/m}$ with the Boltzmann constant k_B and the temperature T. $\mathbf{G} = (g_x(t), g_y(t), g_z(t))^T$ is a vector of Gaussian random numbers each independently drawn according to $p(g) = 1/\sqrt{2\pi}\exp(-g^2/2)$ for each step of integration.

[9] A random seed is a number initialising the generation of pseudo random numbers. Identical random seeds lead to an identical sequence of generated pseudo random numbers.

4.4.2 Effective Linearity of the Synchronization Process

In this part it is shown that the observed synchronization patterns are completely captured by the linearized version of the system. Consequently the nonlinear characteristics of the interaction force are not necessary to observe the synchronization pattern.
If not otherwise stated the phases are calculated from the projection orthogonal to the assumed stripes, i.e. $\Theta = \theta$. Identical to the reference simulations of the realistic crystal presented in Sec. 4.2 the order parameter is calculated for $\theta = 0°, 60°, 120°$ such that the findings can be checked against the reference results in Figure 4.2 on page 37. To make the the linear and nonlinear simulation really comparable the same random seed was used for both simulations. This means that the random forces experienced by the particles were absolutely identical for the same time step. Thus differences in the temporal evolution of both systems are purely caused by the nonlinear features of the interaction force. It shall also be mentioned that if not otherwise stated the allowed region of motion for the perfect crystal was of quadratic shape.

Compression for $\alpha = 0°$

For the anisotropic confinement characterized by $\alpha = 0°$ in the reference simulations alternating stripes were detected purely aligned orthogonal to the x-direction such that only the order parameter for $\theta = 0°$ was indicating synchronization (compare Figure 4.2 on page 37). This result was very well captured by simulating the comparable perfect crystal. In Figure 4.5 the evolution of the linear and the nonlinear system are compared. As can be seen both systems behave absolutely identical until the nonlinear system loses its order because it is "melting". Remarkable is also that the order parameter saturates for the same values as in the reference simulations, i.e. for 0.8 in case $\theta = 0°$.

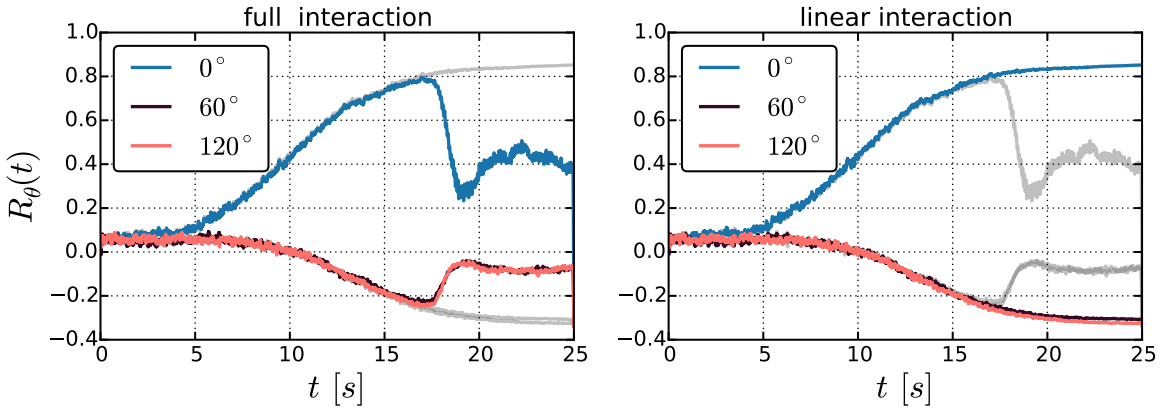

Figure 4.5: Order parameter for the perfect crystal corresponding to $\alpha = 0°$ for the full nonlinear interaction model an the linearized version. Both systems show absolute identical development until the nonlinear system looses its order. In each case the development of the other system is given as gray shadow plot.

Order from dominant hybrid motion

As mentioned in chapter 3 the growing hybrid modes induce always a mixture of longitudinal in plane motion and z-motion. If interpreting the synchronization pattern as dominant motion of the hybrid modes only the x-motion and z-motion should be affected for the case $\alpha = 0°$. This should be true since the hot spots in the particle fluctuation spectra only contain **k**-vectors aligned approximately parallel to the k_x-axis of the **k**-space. Consequently the y-motion should be mainly orthogonal to the hybrid **k**-vectors and therefore neither showing exponential growth nor shall it developing order. Indeed this is true as can be seen on Figure 4.6. To check for order, phases were calculated from the projection on the three orthogonal dimensions x,y,z. To be exact $\phi_{i,x} = \phi_{i,0°}$, $\phi_{i,y} = \phi_{i,90°}$ and $\phi_{i,z}$ was calculated using the z-component of the trajectory $\mathbf{x}_i = (x_i, y_i, z_i)^T$. For every phase the global order parameter $R_\theta(t)$ was calculated for $\theta = 0°$, i.e. assuming stripes orthogonal to the x-direction. To check the growth the kinetic energy for each of the x,y,z components of the velocity ($\mathbf{v} = (v_x, v_y, v_z)^T$) were calculated separately. As can be seen the x an z-dimension are affected by the hybrid modes the y-dimension not. As consequence only the average kinetic energy of the motion in x and z-direction grows while the y-motion saturates at the thermal equilibrium value[10] $k_BT/2$. This correlates well with the formation of stripes. The phases calculated from the x and z dimension form the same stripe pattern while the phase for the y dimension does not. This shows that the observed synchronization is induced by dominant motion of the growing hybrid modes.
For later times the nonlinear system loses the order while for the linear system also the y-dimension is dominated by the hybrid motion. This can be explained by the fact, that most hybrid **k**-vectors are only approximately orthogonal to the y-direction.

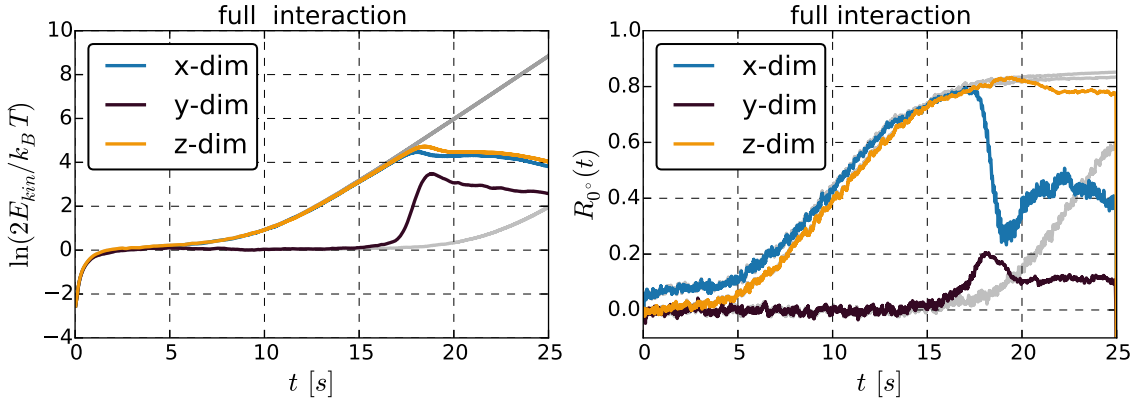

Figure 4.6: Kinetic energy and order parameter for the three orthogonal dimensions x,y,z. Kinetic energy/phases are calculated from projections of the velocities/positions onto the directions x,y,z. The order parameter is in any case calculated for $\theta = 0°$ (assuming stripes orthogonal to the x-direction). A clear coincidence of energy growth and synchronization is visible what verifies the picture of synchronization by domination of growing modes. The evolution of the linear system is shown as gray shadow plot.

[10] According to the equipartition theorem in thermal equilibrium the average kinetic energy for each dimension is given by $\frac{1}{2}k_BT$ where T is the temperature of the system in Kelvin. [9].

Compression for $\alpha = 30°$

For the anisotropic confinement characterized by $\alpha = 30°$ in the reference simulations alternating stripes were detected for 2 directions (compare Figure 4.2 on page 37). On the one hand for $\theta = 0°$ the order parameter reaches 0.6 quiet fast and approximately saturates at this value. On the other hand for $\theta = 60°$ the order parameter grows slower and reaches about 0.6 just before the crystal melts. The evolution of the corresponding perfect crystal is shown in Figure 4.7(i). Again the linear and the nonlinear system develop the absolute identical order until the nonlinear system loses its order. However the evolution of the order parameters compared to the reference simulation show some differences. For the perfect crystal the direction $\theta = 60°$ seem to dominate from beginning and the order parameter for $\theta = 0°$ never reaches a comparable value. This difference can be explained if comparing the evolution of the kinetic energy for the reference simulations and the corresponding simulation of the perfect crystal shown in Figure 4.7 (ii). As can be seen for the reference simulations the energy growth of the y-motion sets in delayed. If we now assume two competing directions of hybrid modes with longitudinal in plane motion in the two directions of $\theta = 0°$ and $\theta = 60°$ the y-motion can be seen as indicator of hybrid motion into the $\theta = 60°$ direction. (Since $x \leftrightarrow 0°$ the y-direction is orthogonal to the 0°-direction.) Consequently in the reference simulations the hybrid modes inducing a positive order parameter for 60° set in delayed. However they show the bigger growth rate compared to the hybrid modes inducing a positive order parameter for 0°. (Since the kinetic energy of the y-motion shows the bigger slope as the x-motion.) Thus first order for 0° is visible and after that order for 60° catches up more an more because of the bigger growth rates. In the reference simulations the crystal melts if the kinetic energy for both directions of hybrid modes is comparable. Otherwise for later times the order for 0° would decrease because of the dominating 60° direction. For the perfect crystal both direction of hybrid modes set in simultaneous what leads to domination of 60° order right from the beginning.

Circular shape of Synchronization Region

To check if the delayed onset of energy growth in y-motion is maybe caused by the more circular shape of the mode-coupling instability region in the reference system, the simulations were also done for a perfect crystal with a circular region of allowed motion. The result is presented in Figure 4.8. As can be seen the changed shape has no qualitative influence of the temporal evolution of the observed order. Identical to the perfect crystal with a quadratic region of motion the growth sets in form the beginning for both directions of hybrid modes. Further the result of the circular system shows that the random difference between two runs are negligible since for this simulation another random seed and thus other random forces were used.

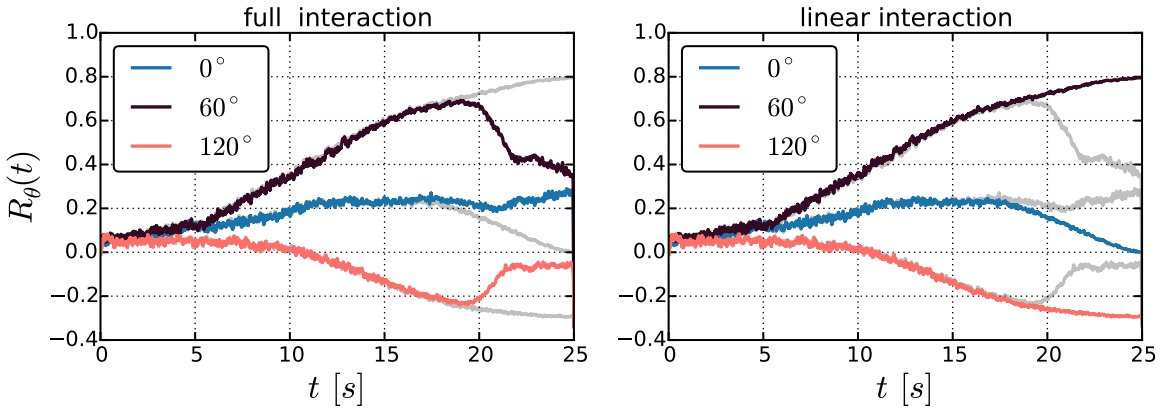

(i) Order parameter for linear and full nonlinear simulation of the perfect crystal.

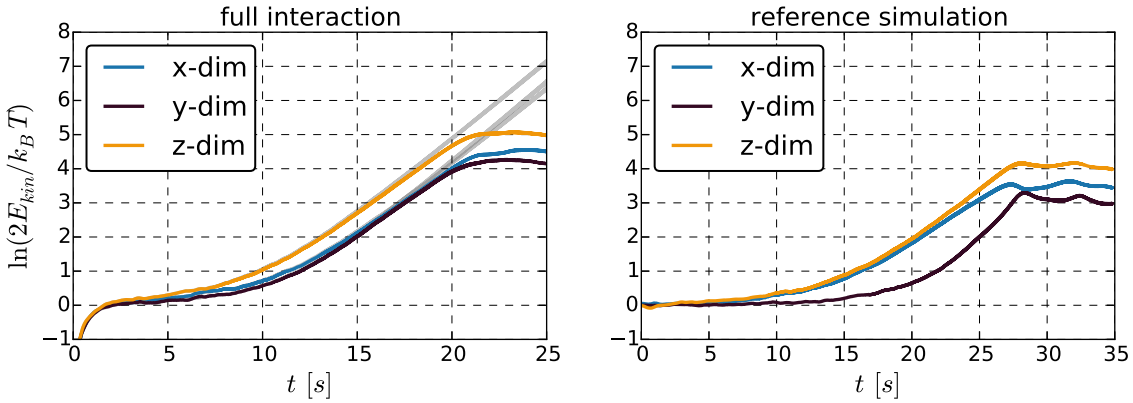

(ii) Comparison of energy growth for the simulated perfect crystal and the reference simulations.

Figure 4.7: (i) Order parameter for the perfect crystal corresponding to $\alpha = 30°$ for the full nonlinear interaction model an the linearized version. Both systems show absolute identical development until the nonlinear system looses its order. In each case the development of the other system is given as gray shadow plot. (ii) Growth of kinetic energy for the different dimensions x,y,z. The evolution reference simulations and the simulation of the perfect crystal are compared. For the reference simulation the growth of the y-dimension sets in delayed compared to the perfect crystal. This explains the difference in observed order of reference simulations and perfect crystal simulations. The data of the reference simulations was evaluated with kind permission of I.Laut.

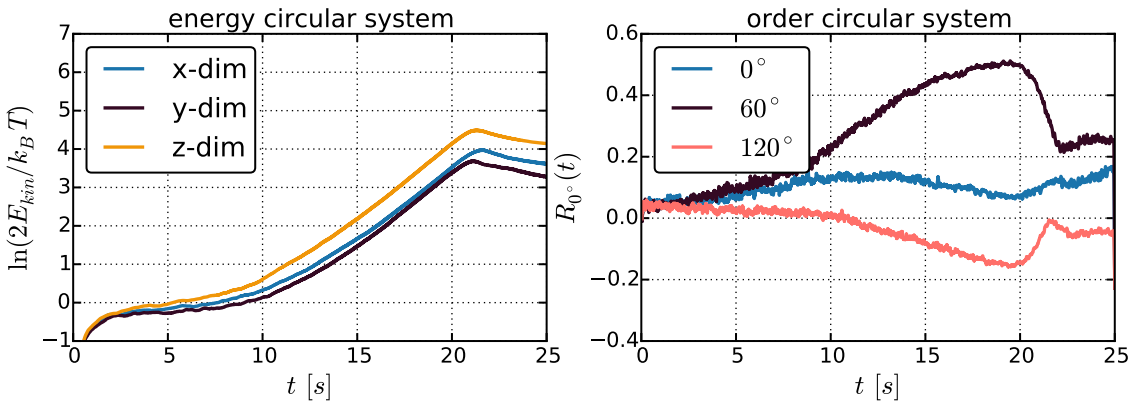

Figure 4.8: Results for simulations of circular shaped perfect crystal corresponding to $\alpha = 30°$. Compared to the quadratic system presented in Figure 4.7 both geometries behave qualitatively identical. This shows that the delayed onset of y-motion growth observed in the reference simulations can not be explained by the circular shape of synchronization area.

Summary

All in all the observed synchronization can be seen as purely linear phenomenon. The temporal evolution of a finite perfect crystal system was simulated for two interaction models. On the one hand for the nonlinear interaction of the point-like wake model. On the other hand for the corresponding linearized version. With respect to the observed synchronization both systems develop absolute identical and only the nonlinear system loses its synchronization order. Therefore we can conclude that the nonlinear characteristics of the interaction even destroys the synchronized state instead of being a crucial ingredient. Further it was shown that synchronized motion is connected to the exponential growth typical for hybrid modes what confirms the assumption of synchronization by domination of hybrid motion.

4.4.3 Difference Between Linear and Nonlinear System

In the last part we have seen that the nonlinear characteristics of the interaction force are not relevant for the synchronization process. This was shown by comparison of the corresponding order parameters which only depend on the calculated phases. In this part the evolution of the linear and the nonlinear interaction model are compared in a more general way. Again the simulations of both interaction models for exact identical random forces and initial conditions were compared. (Only the quadratic system is considered.) However this time it was investigated where the two systems differ in order to understand why this differences are such irrelevant for the observed synchronization. Two parameters are calculated which have proven to be useful for this purpose. The first can be seen as some kind of correlation and is given by

$$C_x(t) = \frac{2}{N} \sum_i \frac{x_i^l(t) x_i^f(t)}{(x_i^l(t))^2 + (x_i^f(t))^2} \tag{4.11}$$

For perfectly identical trajectories it gives trivially 1. While for uncorrelated oscillations it will tend to 0. The second measures the mean relative scale of both interaction models. It is defined to be

$$S_x(t) = \frac{2}{N} \sum_i \frac{(x_i^f(t))^2}{(x_i^l(t))^2 + (x_i^f(t))^2} \tag{4.12}$$

It compares the scale of $x_i^f(t)$ to the mean scale of both oscillations. The variable x may be any of the position variables $\mathbf{d} = (x, y, z)^T$ or any of the velocity variables $\dot{\mathbf{d}} = (v_x, v_y, v_z)^T$. Where $\mathbf{d}_i$ is the deviation form the equilibrium position $\mathbf{X}_i$ of each particle. $x_i^l(t)$ denotes the trajectory of particle i for the linearized interaction model and $x_i^f(t)$ its (full) nonlinear interaction counterpart. The sum runs over all particles[11] $i = 1, ..., N$.

Expected Results

The investigation of the order parameters has shown that up to $t \approx 15s$ the systems were not to distinguish. Accordingly it is tempting to assume both systems to evolve identical up to this point. Afterwards the linear system remains ordered and oscillates with a more and more growing amplitude and kinetic energy. In contrast the nonlinear system loses its order and stops to grow.

From definition of both parameters we can therefore expect 2 stages

- $C_x(t) \approx 1$ and $S_x(t) \approx 1$ for $t < 15s$ because the linear and the nonlinear systems are synchronized in the same way.
- For $t > 15s$ if the nonlinear system loses its order and energy growth while the linear system grows further one may expect $C_x(t) \to 0$ and $S_x(t) \to 0$.

[11] Because of the assumed perfect crystal structure each linear particle i has a exact defined nonlinear counterpart with same equilibrium positions $\mathbf{X}_i$.

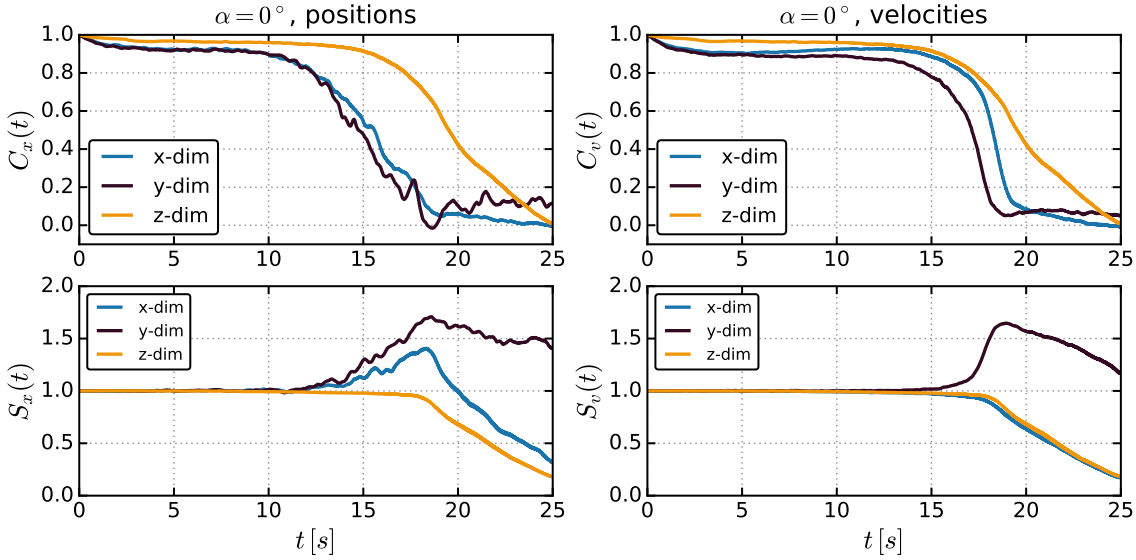

(i) $C_{x/v}(t)$ and $S_{x/v}(t)$ for the simulations of the $\alpha = 0°$ lattice.

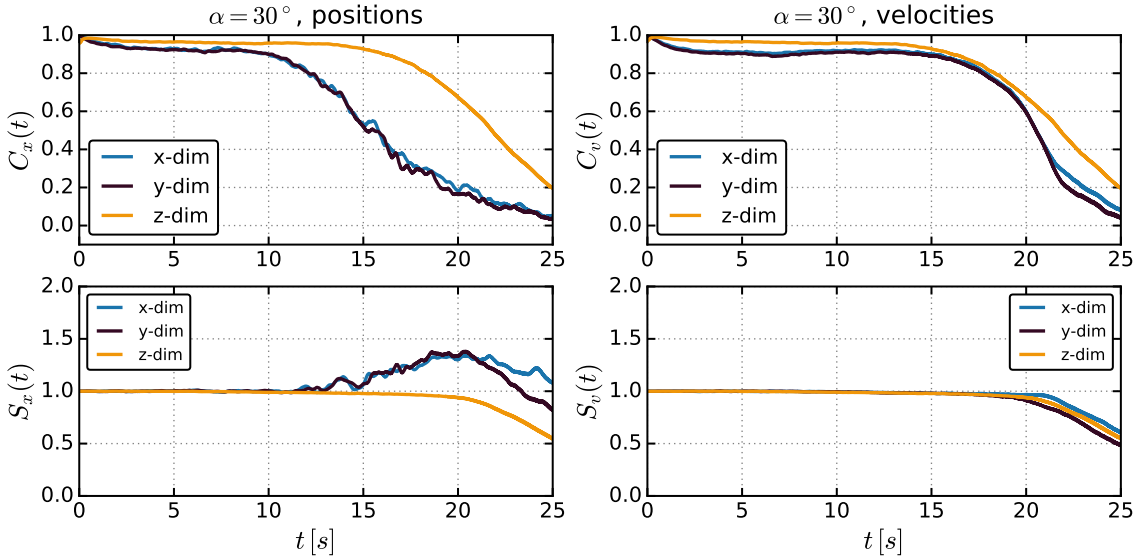

(ii) $C(t)_{x/v}$ and $S(t)_{x/v}$ for the simulations of the $\alpha = 30°$ lattice.

Figure 4.9: For $t \leq 15s$ the order parameter for both systems was developing absolutely identical (compare the last section 4.4.2). Thus one may expect perfectly identical trajectories for the linear and nonlinear simulations. However this expectations is only fulfilled by the velocity trajectories, while the position trajectories already start to differ for $t \approx 10s$. Contrary to the expected the nonlinear elongations are bigger than the linear ones at this point. This can be explained by a slow shift of the equilibrium positions for the nonlinear system. This slow shift has no influence on the oscillatory character as long as the crystal order approximately given.

In Figrue 4.9 the temporal evolution of $C_{x/v}(t)$ and $S_{x/v}(t)$ is plotted for the $\alpha = 0°$ lattice and the $\alpha = 30°$ lattice. The qualitative result is identical for both cases. The parameters calculated from velocities behaves exactly as expected. Up to $t = 15\,s$ the velocity trajectories of the linear and nonlinear interaction model seem to be nearly identical. However the parameters for the position trajectories differ from our expectations. The trajectories start to differ already for $t = 10\,s$. Remarkably the parameter $S_{x/v}(t) > 1$ indicates that the elongations of the nonlinear system are bigger than the elongations of the linear system. However for later times ($t > 20s$) $S_{x/v}(t)$ decreases as expected. (Since the linear system should grow exponentially and the nonlinear not.) This unexpected result can be explained by the observation that for the nonlinear interaction system the particles drift apart from the equilibrium positions as can be seen on Figure 4.10. On the long run this destroys the ordered lattice such that the mode-coupling instability and the synchronization stops. On the short run however the system oscillates around the drifting positions in the same synchronized manner as the linear system. Since the drift is negligible slow on the typical velocity scale of the oscillations it is not affecting the parameters for the velocities.

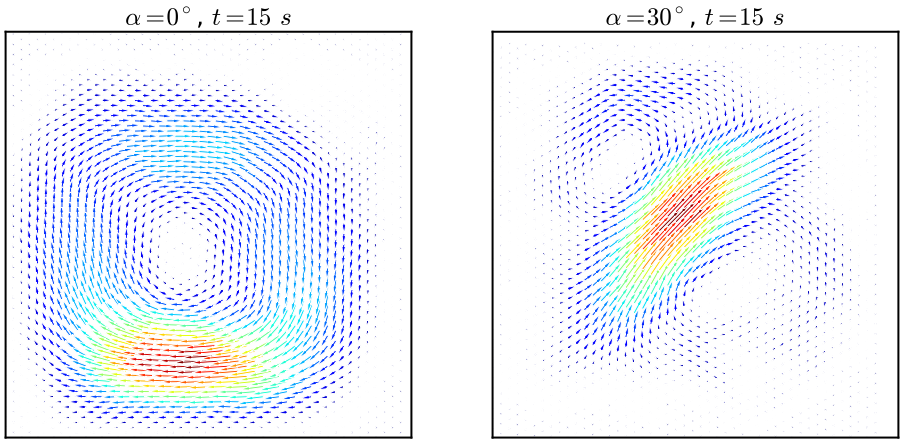

Figure 4.10: Deviation of the average positions from the equilibrium lattice configuration in the crystal plane. Calculated for the nonlinear simulation after $t = 15\,s$ for both deformed crystals symmetries $\alpha = 0°$ and $\alpha = 30°$. The average position was calculated from a time window of 1 second symmetrically arranged around $t = 15\,s$. The comparable linear simulations remain fixed at the equilibrium positions and show no drift. The scale of the vector plots is arbitrary but identical for both cases.

Summary

Also the investigation of the temporal evolution aside from the order parameter confirms the effective linearity of the synchronization process. The detailed comparison of the velocity and position trajectories of the linear and nonlinear interaction model revealed that during the synchronization process both systems only differ by the drifting average positions of the nonlinear system. In that sense the oscillatory properties of both systems are identical until the lattice of the nonlinear system is such deformed that the linearization around the equilibrium positions becomes inappropriate.

4.5 Interpretation in Terms of Linear Theory

In the last part it was shown that the synchronization process is completely determined by linear properties of the point-like wake model. The particle motion seems to be dominated by the properties of the growing hybrid modes. Consequently it should be possible to interpret some aspects of the synchronization process in terms of the linear theory of the plasma crystal presented Chapter 3. The straight forward way to get information about the hybrid modes of the system is the consideration of the dispersion relation of the plasma crystal what is done in the following:

4.5.1 Dispersion Relation for the Observed Situations

To calculate the dispersion relation the same Bravais lattice was assumed as for the simulation of the perfect crystal systems (see Sec. 4.4.1 on page 39). The best overview about the emerging hybrid modes can be achieved by considering the growth rate for the whole 1st Brillouin zone of the **k**-space.

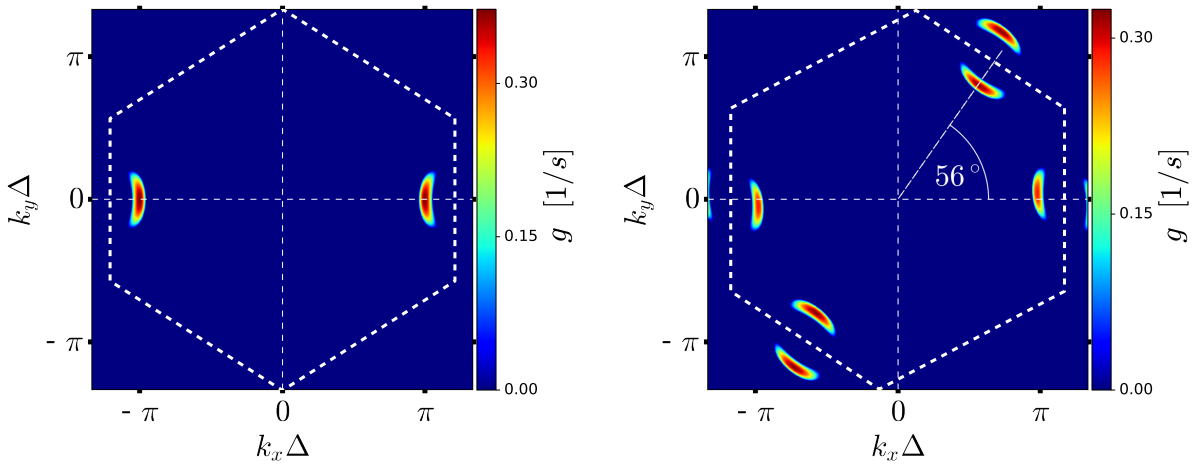

(i) Growth rates for the $\alpha = 0°$ lattice.

(ii) Growth rates for the $\alpha = 30°$ lattice.

Figure 4.11: Growth rates for the both investigated systems $\alpha = 0°$ and $\alpha = 30°$. The friction coefficient $\nu = 1.26/s$ was already taken into account for the calculation. However all values $g < 0$ are set to the same blue color in order to focus on the growing modes. As can be seen the number of growing modes is strongly limited for both cases of deformation.

By considering Figure 4.11 the following conclusions can be made.

- For $\alpha = 0°$ only stripes aligned orthogonal to x or $\theta = 0°$ directions were observed in the simulations. This correlates well with the growth rates for this case. Since $g > 0$ only for **k**-vectors approximately parallel to the k_x-axis one can expect identical phases for positions with identical projection onto the x-direction. What leads to stripes orthogonal to the x-direction.

- For $\alpha = 30°$ a competition between stripes aligned orthogonal to the x and the $60°$ direction were observed in simulations. Again this correlates well with the observed growth rates which predict a competition between stripes in these directions using the same arguing as for the $\alpha = 0°$ case.

- The maximum growth rate for the $\alpha = 0°$ case seems to be slightly bigger than for the $\alpha = 30°$. This can be read of the relative position of the 0.3 tick on the color bar of both plots (also in Figure 4.12 it is shown exactly). It agrees with the observation that in any of the simulations the crystal was melting faster for the deformation characterized by $\alpha = 0°$ compared to $\alpha = 30°$.

- Considering only the $\alpha = 30°$ case the $56° \approx 60°$ direction shows the bigger growth rate. For the simulations of the perfect crystal made for this thesis this explains perfectly the domination of the stripes aligned orthogonal to this direction. However it contradicts the particle fluctuation spectra and evolution of order for the reference simulations. This is however explainable due to the fact that energy and amplitude growth for this direction was starting delayed compared to the simulations of the perfect crystal. This point is already addressed in Sec. 4.4.2 in detail.

All in all the synchronization seem to show qualitative conformity with the distribution of the growth rates in **k**-space. However to gain quantitative information about the dominating modes it is helpful to consider the full dispersion relation along directions of interest in **k**-space. In Figure 4.12 the directions of interest are shown. For the two compressed lattices each pair of point symmetric "hot spots" gives a typical hybrid frequency ω_{hyb} and a typical modulus of hybrid wave vector k_{hyb}. To define a typical direction for the hybrid **k**-vectors of each hot spot pair the directions $0°, 3°, 56°$ are used and shall be denoted as **k**-direction. The values for ω_{hyb}, k_{hyb} and the maximum growth rate (g_{max}) for each case are shown in the following table

α	**k**-direction	k_{hyb}	ω_{hyb}	g_{max}
$30°$	$3°$	$3.07/\Delta$	$98.6/s$	0.292
$30°$	$56°$	$3.09/\Delta$	$98.3/s$	0.321
$0°$	$0°$	$3.13/\Delta$	$97.5/s$	0.379

Apparently all values are quite similar. Whether this values match the observed synchronization will be adressed in the next section.

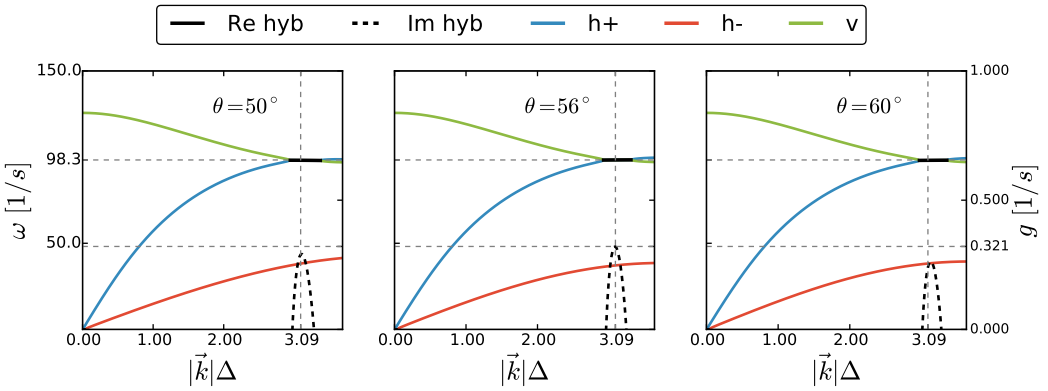

(i) Dispersion relation for $\alpha = 30°$ considering the "hot spot" in the 56° direction.

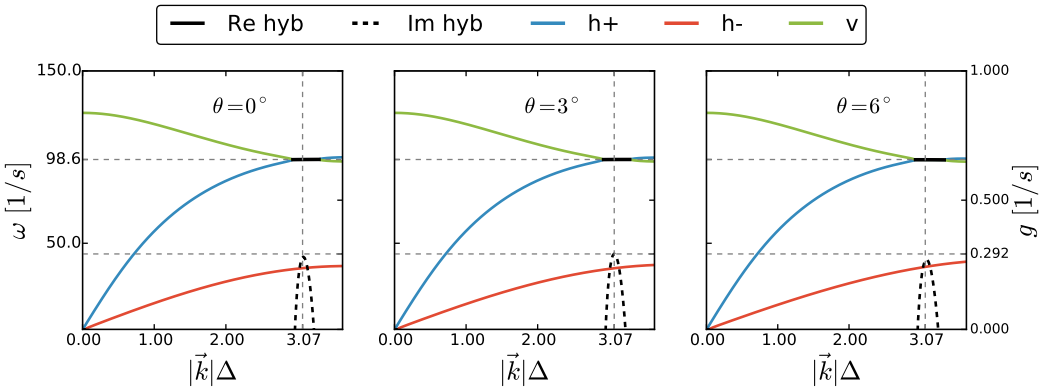

(ii) Dispersion relation for $\alpha = 30°$ considering the "hot spot" in the 3° direction.

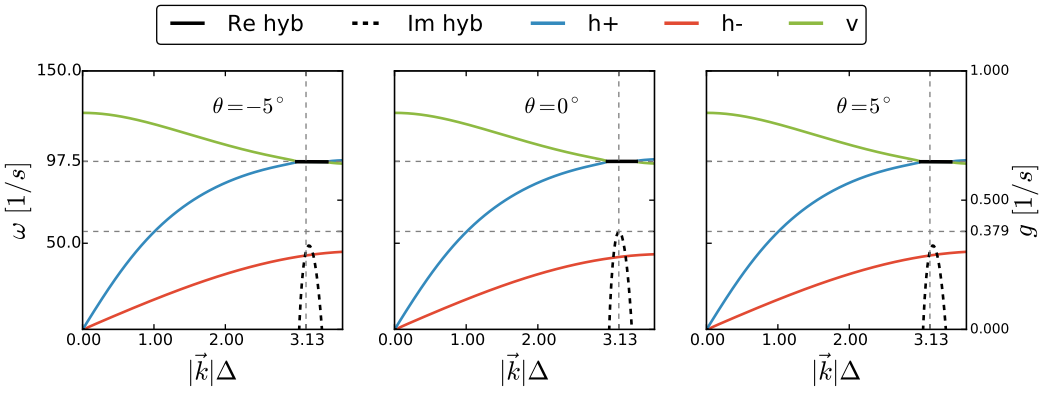

(iii) Dispersion relation for $\alpha = 0°$ considering the "hot spot" in the 0° direction.

Figure 4.12: (i) For $\alpha = 30°$ and the hot spot for 56° all dominating hybrid modes have the approximately same frequency ($\omega_{hyb} = 98.3/s$) and modulus of **k**-vector ($k_{hyb} = 3.09/\Delta$). (ii) For $\alpha = 30°$ and the hot spot for 3° all dominating hybrid modes have the approximately same frequency ($\omega_{hyb} = 98.6/s$) and modulus of **k**-vector ($k_{hyb} = 3.07/\Delta$). (ii) For $\alpha = 0°$ all dominating hybrid modes have the approximately same frequency ($\omega_{hyb} = 97.5/s$) and modulus of **k**-vector ($k_{hyb} = 3.13/\Delta$).

4.5.2 Frequency Synchronization

In this part the frequency synchronization is investigated in a quantitative manner. Using the guiding picture of dominating hybrid modes the observed synchronization frequencies should be given by the hybrid frequencies ω_{hyb} calculated for each of the hot spots in the last section.

Calculation of Frequency and Characteristics

As presented in Sec. 4.2 the phase was assumed to grow linearly from 0 to 2π between two maxima of $p_{i,\Theta}(t)$, which is the projection of the particle position onto the direction Θ measured anticlockwise from the positive x-axis. Naturally the time between two maxima of $p_{i,\Theta}(t)$ is the current period $T_{i,\Theta}(t)$ of the oscillation[9]. The period was assumed to jump discontinuous from one value to the next, because it is not relevant for the time scales of interest. In this way we get a current *frequency* for the projection of particle i on the Θ-direction, given as

$$\omega_{i,\Theta}(t) = \frac{2\pi}{T_{i,\Theta}(t)} \tag{4.13}$$

Since the dominating hybrid modes induce the hybrid frequency ω_{hyb} independent from the particle position it is straight forward to calculate the frequency sample mean and standard deviation[3] from the values realized by the ensemble of all particles for each time step in order to characterize the frequency synchronization. Hence the sample mean frequency was calculated according to

$$\overline{\omega}_{\Theta}(t) = \frac{1}{N}\sum_{i=1}^{N}\omega_{i,\Theta}(t) \tag{4.14}$$

and the uncorrected sample standard deviation for each time step was calculated using

$$\sigma_{\Theta}(t) = \sqrt{\frac{1}{N}\sum_{i=1}^{N}\left(\omega_{i,\Theta}(t) - \overline{\omega}_{\Theta}(t)\right)^2} \tag{4.15}$$

For a perfectly synchronizing system we expect a vanishing standard deviation $\sigma_{\Theta} \to 0$ while the sample mean approaches the dominant hybrid frequency $\overline{\omega}_{\Theta} \to \omega_{hyb}$.

The $\alpha = 0°$ Deformation

The deformed lattice for the case $\alpha = 0°$ shows only one pair of "hot spots" with the identical hybrid frequency $\omega_{hyb} = 97.5/s$. As already mentioned before the growing **k**-vectors are all aligned approximately parallel to the k_x-axis of the **k**-space. Using that hybrid modes typically only induce longitudinal in-plane motion[12] we can expect that only the motion of the x-dimension is affected since all hybrid **k**-vectors are parallel or anti-parallel to the x-direction. It is therefore convenient to investigate the frequency from the projection onto the two orthogonal directions x and y in order to verify the independence of the y-dimension. Thus $\sigma_x = \sigma_{0°}$, $\overline{\omega}_x = \overline{\omega}_{0°}$ and $\sigma_y = \sigma_{90°}$, $\overline{\omega}_y = \overline{\omega}_{90°}$ were calculated for the linear and the full nonlinear interaction model of the perfect crystal. Furthermore it was also possible to analyse the results of the reference simulations where the crystal was simulated in a quite realistic way.

Simulations of the perfect crystal: On Figure 4.13 the situation is shown for the perfect crystal simulations. As a first general observation we see that again the linear and nonlinear interactions produce exact identical results until the nonlinear system loses the order while the linear system remains ordered.

Focusing on the *x-components* we see the following. The linear system shows a permanent decrease in standard deviation til it reaches $\sigma_x \approx 0$ for $t = 20s$. Simultaneously $\overline{\omega}_x$ approaches the hybrid frequency more and more and for $t = 20s$ we have exactly $\overline{\omega}_x = \omega_{hyb} = 97.5/s$. For later times $t > 20s$ the system remains in this perfectly synchronized state $\sigma_x \approx 0$ and $\overline{\omega}_x = \omega_{hyb}$. The nonlinear system shows the exact same behaviour for $t < 17s$. The standard deviation (σ_x) constantly decreases while the mean frequency approaches the hybrid frequency ($\overline{\omega}_x \to \omega_{hyb}$) in the same way as for the linear system. However for $t = 17s$ the synchronization stops and the nonlinear system loses its order compared to the linear one, especially the mean frequency takes an qualitative different value.

The *y-components* reveal the following evolution. For times $t < 17s$ we see that σ_y as well as $\overline{\omega}_y$ fluctuate around stable values what indicates a stable distribution but no frequency synchronization. For $t > 17s$ the linear system seems to develop the same order also for the y-dimension. The reason is probably the not complete independence of the y-dimension since the hybrid **k**-vectors are not really perfectly parallel to the x-axis. Much more interesting is the nonlinear system where especially the standard deviation σ_y shows a sharp drop for $t \approx 17s$. This shows that while on the one hand the linear order is destroyed by the nonlinear effects for $t \approx 17s$ (compare the x-component), on the other hand a kind of nonlinear order is induced in terms of a narrower distribution of frequencies.

[12] Longitudinal in-plane motion means that the motion in the x-y-plane induced by this mode is purely parallel to the **k**-vector of the mode. Compare Chapter 3.

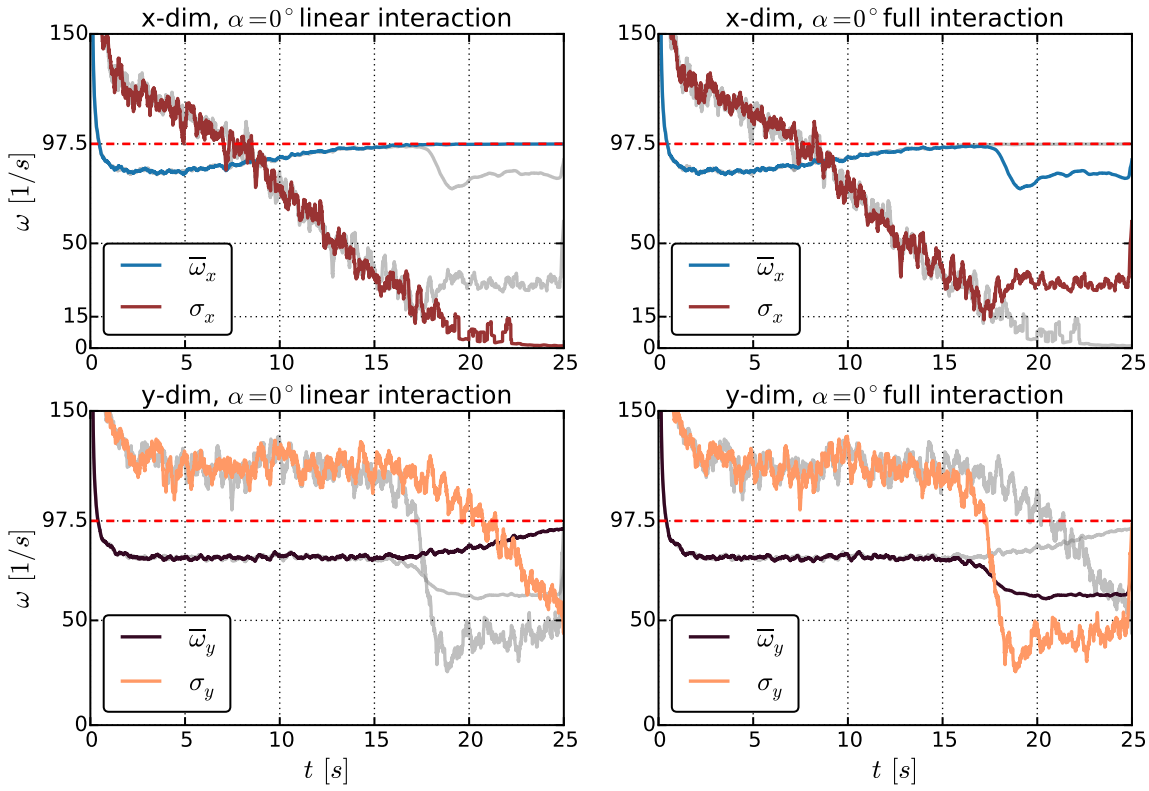

Figure 4.13: Frequency synchronization of the perfect crystal for the $\alpha = 0°$ lattice. For the x-motion we see a clear synchronization. The standard deviation (σ_x) constantly decreases while the average frequency approaches the predicted value $\overline{\omega_x} = \omega_{hyb} = 97.5/s$. As correctly predicted the y-motion shows no synchronization. For $t \approx 17s$ the nonlinear system loses the order. Remarkably for the y-motion this coincides with a sharp decrease in standard deviation (σ_y).

Comparison with reference simulations: The simulation data of the reference simulations [19] were evaluated in the same way. For this purpose only a small central region showing the synchronizaton pattern was picked out and analyzed. The results are shown on Figure 4.14. At a first glance the results match the simulations of the perfect crystal very well.

For the *x-components* the standard deviation decreases constantly til it reaches $\sigma_x \approx 4/s$ for $t = 15s$. At the same time the mean frequency approaches the hybrid frequency and for $t = 15s$ we have $\overline{\omega}_x = \omega_{hyb} = 97.5/s$ as predicted by the dispersion relation. This synchronized state remains stable for $t \approx 15s - 20s$ until a nonlinear perturbation is visible. Notably the synchronization seems to be developed even more exact as compared with the nonlinear simulation of the perfect crystal.

Also the investigation of the *y-components* confirm the results obtained for the perfect crystal. In the qualitative same way for times $t < 19s$ we see that σ_y as well as $\overline{\omega}_y$ fluctuate around approximately stable values what indicates a stable distribution but no frequency synchronization. For $t \approx 19s$ the standard deviation σ_y shows a sharp drop. For the investigation of the perfect crystal this drop was indicating the point where the nonlinear characteristics of the interaction became dominant (compare Figure 4.13). Also for the reference simulations the drop for the y-components and the visible nonlinear perturbation for the x-components at $t \approx 20s$ coincide quite good.

Remarkable is also that the standard deviation of the reference simulations seems to be generally lower. This can be seen by comparing the σ_y of the reference and nonlinear/linear simulations.

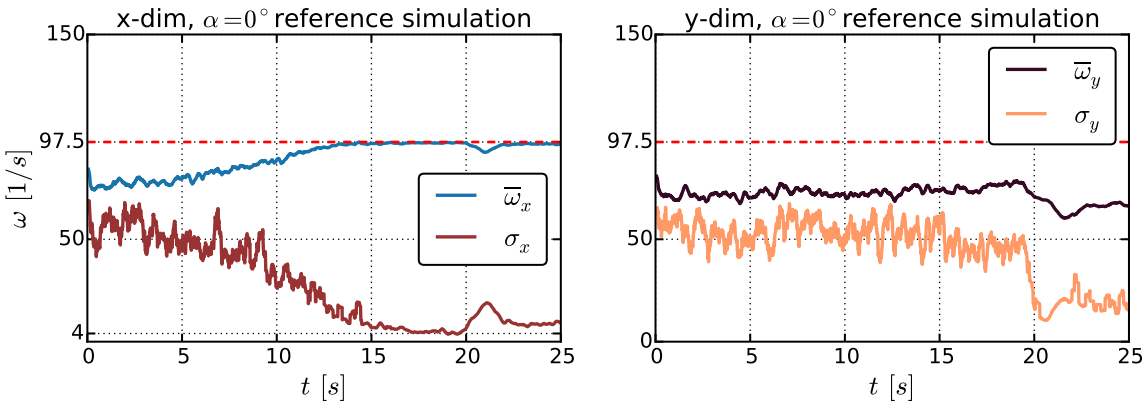

Figure 4.14: Frequency synchronization of the reference simulations for the $\alpha = 0°$ deformation. The results obtained for the simulations of the perfect crystal are also verified by the more realistic reference simulations. We see for the x-motion $\sigma_x \to 4/s$ while $\overline{\omega_x} \to \omega_{hyb} = 97.5/s$. The y-motion shows no synchronization as predicted. Also the sharp drop in σ_y for "melting" point is visible. Remarkably the synchronization of the reference simulation seem to develop even more accurate as for the nonlinear simulations of the perfect crystal. The data of the reference simulations was evaluated with kind permission of I.Laut.

The $\alpha = 30°$ Deformation

The deformed lattice for the case $\alpha = 30°$ shows two pairs of "hot spots". One for the **k**-direction 3° with a hybrid frequency $\omega_{hyb} = 98.6/s$ and the second for the **k**-direction 56° with a hybrid frequency $\omega_{hyb} = 98.3/s$. According to the dispersion relation the 56° direction should be the dominant direction with the bigger growth rate. For this case both the x and the y-component of motion are expected to show motion dominated by hybrid modes since longitudinal hybrid motion should be induced into the two linear independent **k**-directions. Nevertheless one may assume the y-component of motion mainly dominated by the hybrid motion into the 56° direction using the same arguing as for the independence of y in the $\alpha = 0°$ case. While the x-component represents a superposition of both **k**-directions (56° and 3°). Consequently it is again convenient to calculate the frequency again for two the orthogonal directions x and y. Thus again $\sigma_x = \sigma_{0°}$, $\overline{\omega}_x = \overline{\omega}_{0°}$ and $\sigma_y = \sigma_{90°}$, $\overline{\omega}_y = \overline{\omega}_{90°}$ were calculated for the linear and the full nonlinear interaction model of the perfect crystal. Also the reference simulations are again evaluated for comparison.

Simulations of the perfect crystal: On Figure 4.15(i) the situation is shown for the perfect crystal simulations in case $\alpha = 0°$. The x and y-component behave nearly identical for this deformation. For the linear system the standard deviations σ_x, σ_y permanently decrease while the mean frequencies $\overline{\omega}_x, \overline{\omega}_y$ approach the predicted hybrid frequencies. For the y-motion this is given by $\overline{\omega}_y = 98.3/s$ because it purely represents the 56°-direction hybrid motion. For the x-motion we have influence of both **k**-direction, 56° and 3° with $\omega_{hyb} = 98.3/s$ and $\omega_{hyb} = 98.6/s$ respectively. Since the 56°-direction should dominate we can also expect $\overline{\omega}_x = 98.3/s$. What seems to be true if looking at the magnification window of Figure 4.15(i). The nonlinear system again behaves exactly equivalent until the nonlinear influences destroy the frequency synchronization. This happens for $t \approx 20s$. It shall be mentioned that this moment was found independently in any other investigations of the $\alpha = 30°$ case as onset of nonlinear dominance corrupting the order.

Comparison with reference simulations: For comparison with the reference simulation in the same way as for the former case a small central region showing the synchronization was picked out and analyzed. It is shown in Figure 4.15(ii). Again at a first glance the synchronization seem to develop even more exact as compared with nonlinear simulation of the perfect crystal. For the x-motion we see σ_x decreasing again til it reaches $\sigma_x = 4/s$ while the mean frequency approaches $\overline{\omega}_x = 98.6/s$. As already mentioned in former parts (see Sec. 4.4.2) during the reference simulations for the $\alpha = 30°$ deformation, the exponential growth of the y-motion sets in delayed. Consequently the frequency synchronization of the y-motion develops delayed. Thus different from the simulations of the perfect crystal, for the reference simulations the x-motion is not dominated by the 56° direction and settles down at $\overline{\omega}_x = 98.6/s$ while the y-motion approaches $\overline{\omega}_y = 98.3/s$. This can be seen on the magnification window on Figure 4.15(ii).

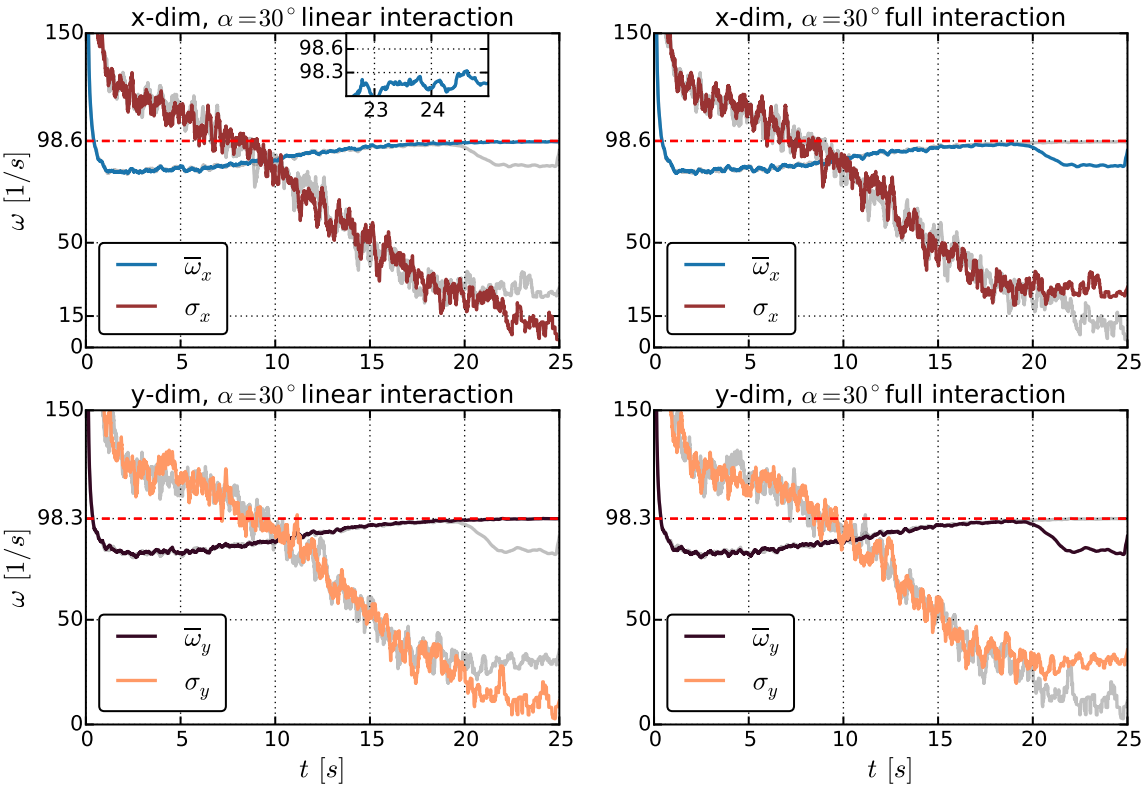

(i) Frequency synchronization of the perfect crystal for the $\alpha = 30°$ lattice.

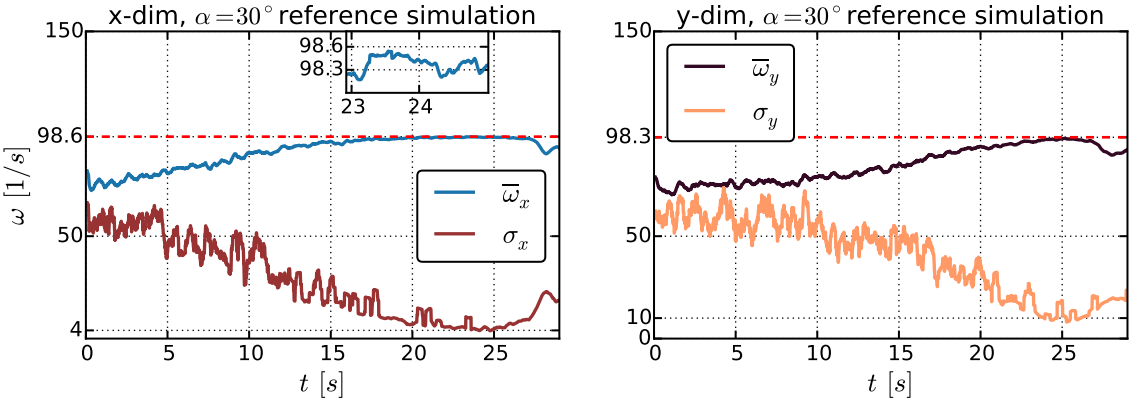

(ii) Frequency synchronization of the reference simulations for the $\alpha = 30°$ deformation.

Figure 4.15: Also for the case = 0° the x and y-motion synchronize in perfect agreement with the predicted values. In any case the standard deviation $\sigma_{x/y}$ decreases constantly while the mean frequency approaches the predicted hybrid frequency $\overline{\omega}_{x/y} \to \omega_{hyb}$. Remarkable the synchronization seem to develop again even more accurate for the reference simulations. The data of the reference simulations was evaluated with kind permission of I.Laut. (For more information see text.)

4.5.3 Phase Synchronization

In the last part we have seen that the observed frequency synchronization agrees perfectly with the hybrid frequencies predicted by the dispersion relation. Even the realistic reference simulations match the predicted hybrid frequencies perfectly. Hence the guiding picture of synchronization by dominant hybrid motion seems to be correct.

As last step the observed synchronization phase pattern of alternating stripes has to be explained from linear properties. For this purpose the distribution of phases for the nonlinear, full interaction model of the perfect crystal is investigated in detail. Similar to the frequency synchronization the results are compared to key properties of the dispersion relation. We focus on simulations of the nonlinear interaction model of the perfect crystal since the results have shown to be comparable to the reference simulations. However the fixed particle order[13] of the assumed perfect crystal reduces the numerical effort for the evaluation drastically.

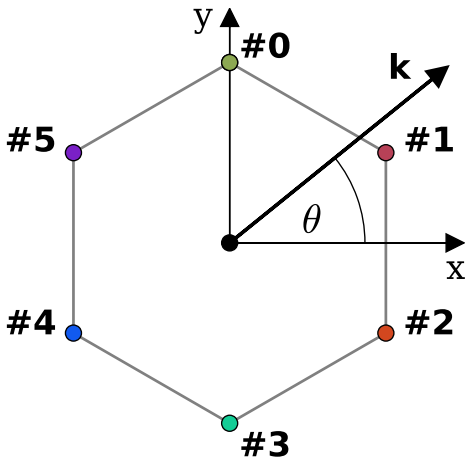

Figure 4.16: Used next neighbour indices for the hexagonal structure. Each particle of the investigated system has next neighbours at the same relative positions as the central black particle on this figure. (The same color code is used in the following histogram figures.)

In the picture of dominating hybrid modes, the phase of particle i induced by a growing hybrid mode (plane wave, $\mathbf{d}(t) \propto \exp(-i\omega t + i\mathbf{k}\cdot\mathbf{X}_i)$) of wave vector $\mathbf{k}$ is given by $\Phi_i = \mathbf{k}\cdot\mathbf{X}_i$. Consequently the particle position has to be considered and the resulting synchronization value can not be expected to be position independent as for the case of frequency. However if we focus on the phase differences of two particles $\Delta\Phi_{ji} = \Phi_i - \Phi_j = \mathbf{k}\cdot(\mathbf{X}_i - \mathbf{X}_j)$ the result is only dependent on the relative position of both particles. In this case we can exploit the lattice symmetry. Since every particle has the exact same number of next neighbours at the exact same relative positions it seems to make sense to look at the distribution of phase differences for the 6 possible relative positions of next neighbours.
To be exact the next neighbours shall be characterized by the index n where $n \in \{\#0, \#1, \#2, \#3, \#4, \#5\}$ as defined in Figure 4.16. In that way each particle i has "the same" neighbour at position $\mathbf{X}_j = \mathbf{X}_i + \mathbf{R}_n$ where $\mathbf{R}_n$ denotes the relative position of the next neighbour with index n. It is obvious that for the the hypothetical situation of motion induced by on single hybrid mode ($\mathbf{d}(t) \propto \exp(-i\omega_{hyb}t + i\mathbf{k}_{hyb}\cdot\mathbf{X}_i)$) with $\mathbf{k}$-vector $\mathbf{k}_{hyb}$ the

[13] Each particle has a defined equilibrium lattice position $\mathbf{X}_i$ such that the neighbours of each particle are exactly defined.

phase difference for the neighbour n of particle i is given by the fixed value $\Delta\Phi_{ni} = \mathbf{k}_{hyb}\cdot\mathbf{R}_n$. It is therefore identical for each particle (for the infinite spreading plane wave). Assuming for the moment that each hot spot pair is characterized by the two point symmetric central hybrid vectors of the two hot spots, we can calculate an expected phase shift $\Delta\Phi_n$ for each relative next neighbour position and hot spot pair. The results are listed in the following table

α	**k**-direction	k_{hyb}	$\Delta\Phi_0$	$\Delta\Phi_1$	$\Delta\Phi_2$	$\Delta\Phi_3$	$\Delta\Phi_4$	$\Delta\Phi_5$
30°	3°	$3.07/\Delta$	∓ 0.16	∓ 2.69	∓ 2.53	± 0.16	± 2.69	± 2.53
30°	56°	$3.09/\Delta$	∓ 2.59	∓ 2.77	∓ 0.17	± 2.59	± 2.77	± 0.17
0°	0°	$3.13/\Delta$	0	∓ 2.59	∓ 2.59	0.0	± 2.59	± 2.59

The values are calculated for the corresponding deformed Bravais lattices of the cases $\alpha = 0°$ and $\alpha = 30°$. The central $\mathbf{k}_{hyb}$-vector of each hot spot was assumed to point in the particular **k**-direction with length k_{hyb} of the table. In the table only one **k**-directions for each hot spot pair is given since the inverted direction is implied as ($3° \to 183°$, $56° \to 236°$, $0° \to 180°$). For explanation of the observed patterns naturally both propagation directions have to be considered since both directions are physically equivalent. For the inverted propagation directions only the sign of $\Delta\Phi_n$ switches. Therefore in the table both signs are shown since the signs are in principle irrelevant or both possible.

The Calculated Distributions

The calculated phases $\phi_{i,\Theta}(t)$ of particle i from projection onto direction Θ grow in time with the current frequency $\omega_{i,\Theta}(t)$ considered in the previous section. As direct consequence it is only possible for two particles two show a defined phase difference which is constant in time, if they oscillate with the same frequency. Thus it is reasonable to consider the distribution of phase differences for the time of most accurate frequency synchronization in any of the two cases $\alpha = 0°$ and $\alpha = 30°$. Since they should contain the structure of the observed patterns in a well developed manifestation.

For every particle i the phase difference was now calculated for each of the next neighbours $n \in \{\#0, \#1, \#2, \#3, \#4, \#5\}$ with the relative position $\mathbf{R}_n$ according to

$$\Delta\Phi_{n,i,\Theta}(t) = \phi_{l,\Theta}(t) - \phi_{i,\Theta}(t) \text{ such that } \mathbf{X}_l = \mathbf{X}_i + \mathbf{R}_n \tag{4.16}$$

where $\mathbf{X}_i, \mathbf{X}_l$ denote the equilibrium positions of the particles. For the time of maximum synchronization ($t = t_{sync}$) the distributions over all particles i for fixed Θ and n are shown as histograms. For boundary particles the phase difference with respect to next next neighbours which are not allowed to move have been neglected. Since for the evaluation of frequency synchronization the separate investigation of the orthogonal x and y direction has shown to be convenient the same was done for the evaluation of phase synchronization. To be exact phase differences were calculated for the two cases $\phi_{i,\Theta} = \phi_{i,0°} = \phi_{i,x}$ and $\phi_{i,\Theta} = \phi_{i,90°} = \phi_{i,y}$ separately. Thus each histogram is once shown for the distribution of

x-phase differences $\Delta\Phi_x$ and once for the distribution of y-phase differences $\Delta\Phi_y$ for each n. Because the calculated phases $\phi_{i,\Theta}$ take values between 0 and 2π the range of possible phase differences goes from -2π to 2π such that $\Delta\Phi_{x,y} \in (-2\pi, 2\pi)$.

The $\alpha = 0°$ Deformation

For $\alpha = 0°$ we have again the one hot spot pair for the **k**-direction $\theta = 0°$. As already explained before, for this hybrid **k**-direction the longitudinal in-plain hybrid motion primarily affects the x-motion while the y-motion is independent.

If focusing for the moment on the ***x-phase differences*** ($\Delta\Phi_x$) the $\mathbf{k}_{hyb}$ orientation parallel to the x-axis should lead to stripes of identical phase differences for particles of same x-position. From the specific calculated values of the table on page 62 one therefore identifies three pairs of identical phases

$$(\#0, \#3) = 0, \qquad (\#1, \#2) = \mp 2.59, \qquad (\#4, \#5) = \pm 2.59 \tag{4.17}$$

We see that the pair (#0, #3) and the central particle should show the exact same phase while the other pairs of identical x-position (#1, #2) and (#4, #5) should form stripes with phases somehow connected to the values ± 2.59.

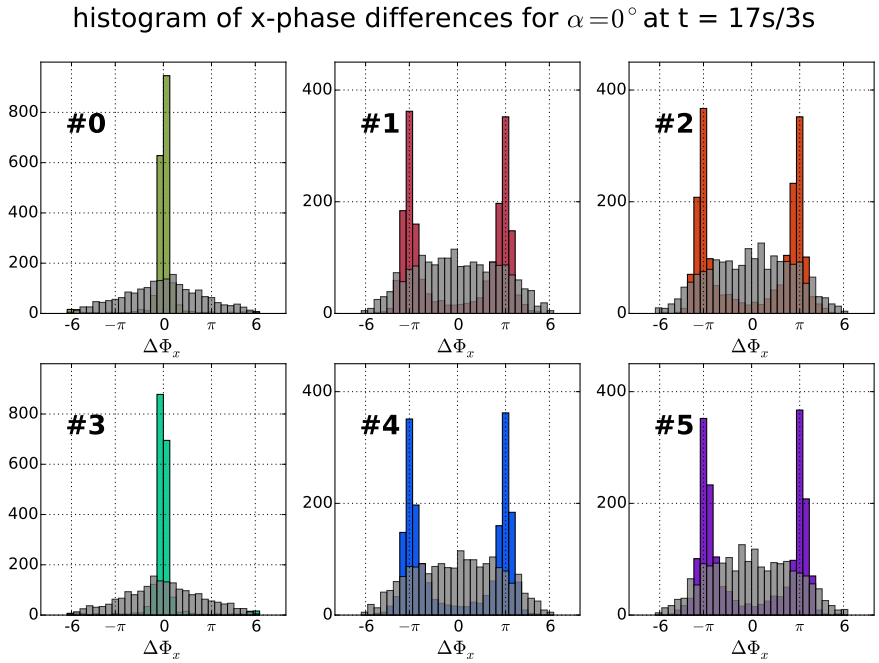

Figure 4.17: Phase distribution of the x-motion for all next neighbours for $t_{sync} = 17s$ (colored) and $t = 3s$ (gray). As predicted by assumption of one dominant hybrid mode in case $\alpha = 0°$ we have nearly no phase difference for (#0, #3). The alignment of stripes and the similarity of distributions of (#1, #2, #4, #5) is also correctly predicted. However the dominant phase difference of $\Delta\Phi_x = \pm\pi$ for this neighbours varies from the predicted $\Delta\Phi_x = \pm 2.59$.

If looking at Figure 4.17 the distribution of x-phase differences $\Delta\Phi_x$ is shown for the time of maximum frequency synchronization $t_{sync} = 17s$ (in case $\alpha = 0°$). For comparison also the distribution for $t = 3s$ are plotted as gray shadow plot. It represent the not synchronized situation. At a first glance the observed matches the expectations quite good. The central particle forms nearly identical phases with the pair (#0, #3) what corresponds to the $\Delta\Phi_x = 0$ peak for these distributions. Also the other pairs $(\#1, \#2) = \mp 2.59$ and $(\#4, \#5) = \pm 2.59$ show very similar distributions as may expected from the identical values of phase differences. In that sense the alignment of stripes orthogonal to the $\mathbf{k}_{hyb}$-direction is perfectly verified. However the distribution of these neighbours peak in any case for $\Delta\Phi_x = \pm\pi$. The positive maximum bin of the histogram samples values in the range $\Delta\Phi_x = \pi \pm 0.2$ and is therefore clearly to distinguish from $\Delta\Phi_x = 2.59$. This shows that the system tends to synchronize in anti-phase stripes ($\Delta\Phi_x = \pm\pi$) and not in the phase difference directly induced by the dominant hybrid vector $\mathbf{k}_{hyb}$. As will be shown in Sec. 4.6 this mismatch can be lifted by the finding that the superposition of both wave propagation directions leads to the formation of standing waves.

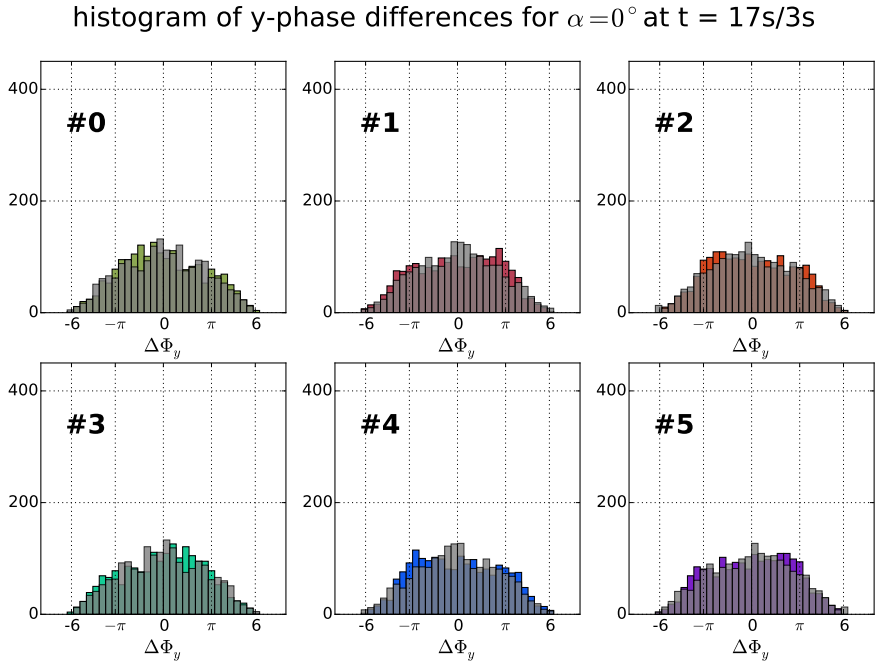

Figure 4.18: Phase distribution of the y-motion for all next neighbours for $t_{sync} = 17s$ (colored) and $t = 3s$ (gray). As predicted by assumption of dominant hybrid motion in case $\alpha = 0°$ the distributions of y-phases remains unchanged by the synchronization.

For the frequency synchronization in case $\alpha = 0°$ the hybrid motion has shown to affect only the x-motion. (Because all hybrid vectors are effectively parallel to the x-axis.) Consequently also the ***y-phase differences*** ($\Delta\Phi_y$) should be not affected by the synchronization. On Figure 4.20 we see that this is indeed true. For the time of maximal

frequency synchronization in x-motion $t_{sync} = 17s$ the distribution of y-phases is qualitative identical to $t = 3s$. This shows that in contrast to the x-phases the y-phases show no synchronization.

The $\alpha = 30°$ Deformation

For $\alpha = 30°$ we have the situation of two hot spot pairs for the **k**-directions $\theta = 3°$ and $\theta = 56°$ (compare Sec. 4.5.1 on page 52). If one assumes $\theta = 3° \approx 0°$ and $= 56° \approx 60°$ one may argue that in this situation the $\theta \approx 0°$ hot spot pair leads to the same stripe formation as during the $\alpha = 0°$ case while the $\theta \approx 60°$ hot spot pair induces a second competing stripe pattern rotated anticlockwise by the angle 60°. With this logic we can identify the following pairs from the table on page 62. The $\theta \approx 0°$ hot spot pair gives

$$(\#0, \#3) \approx 0, \quad (\#1, \#2) \approx \mp 2.6, \quad (\#4, \#5) \approx \pm 2.6 \tag{4.18}$$

and the $\theta \approx 60°$ hot spot pair gives a competing pattern with

$$(\#0, \#1) \approx \mp 2.6, \quad (\#5, \#2) \approx 0, \quad (\#4, \#3) \approx \pm 2.6 \tag{4.19}$$

Focusing on the ***x-phase differences*** ($\Delta\Phi_x$) we expect a competition between both stripes patterns for the phases of the x-motion. (Since both hybrid **k**-directions induce x-motion.) This competition makes a prediction difficult. However if we look on the predicted values for both cases we see that only the neighbour indices #1 and #4 show the same predicted magnitude of phase difference ($\approx \pm 2.6$) for both competing hybrid **k**-directions. Thus one may expect these two neighbours to behave similar compared to the $\alpha = 0°$ case while the other next neighbours do not. On Figure 4.19 the results are shown for the time of maximum frequency synchronization $t_{sync} = 19s$ (in case $\alpha = 30°$). For comparison also the distributions for $t = 3s$ are plotted as gray shadow plot. It represent the not synchronized situation. As motivated only for the #1 and #4 next neighbour position the anti-phase synchronization is visible in contrast for all other next neighbours no clear peak is visible.

For the ***y-phase differences*** ($\Delta\Phi_y$) we can again assume an approximately independence of the y-motion on the 3°-direction hot spot pair. Since the longitudinal hybrid motion of this hybrid direction is approximately orthogonal to the y-direction. Consequently only the $56° \approx 60°$ hybrid direction is affecting the y-motion and y-phases such that only the order predicted by the $\theta \approx 60°$ direction is important. Hence one can expect the similar distributions as for the $\alpha = 0°$ case. Only the pairs of identical phase should rotated anticlockwise by $\approx 60°$. Looking again on Figure 4.19 we see that indeed this is true. The anti-phase pairings are in good agreement with the prediction for $\theta \approx 60°$ hot spot pair (compare 4.19).

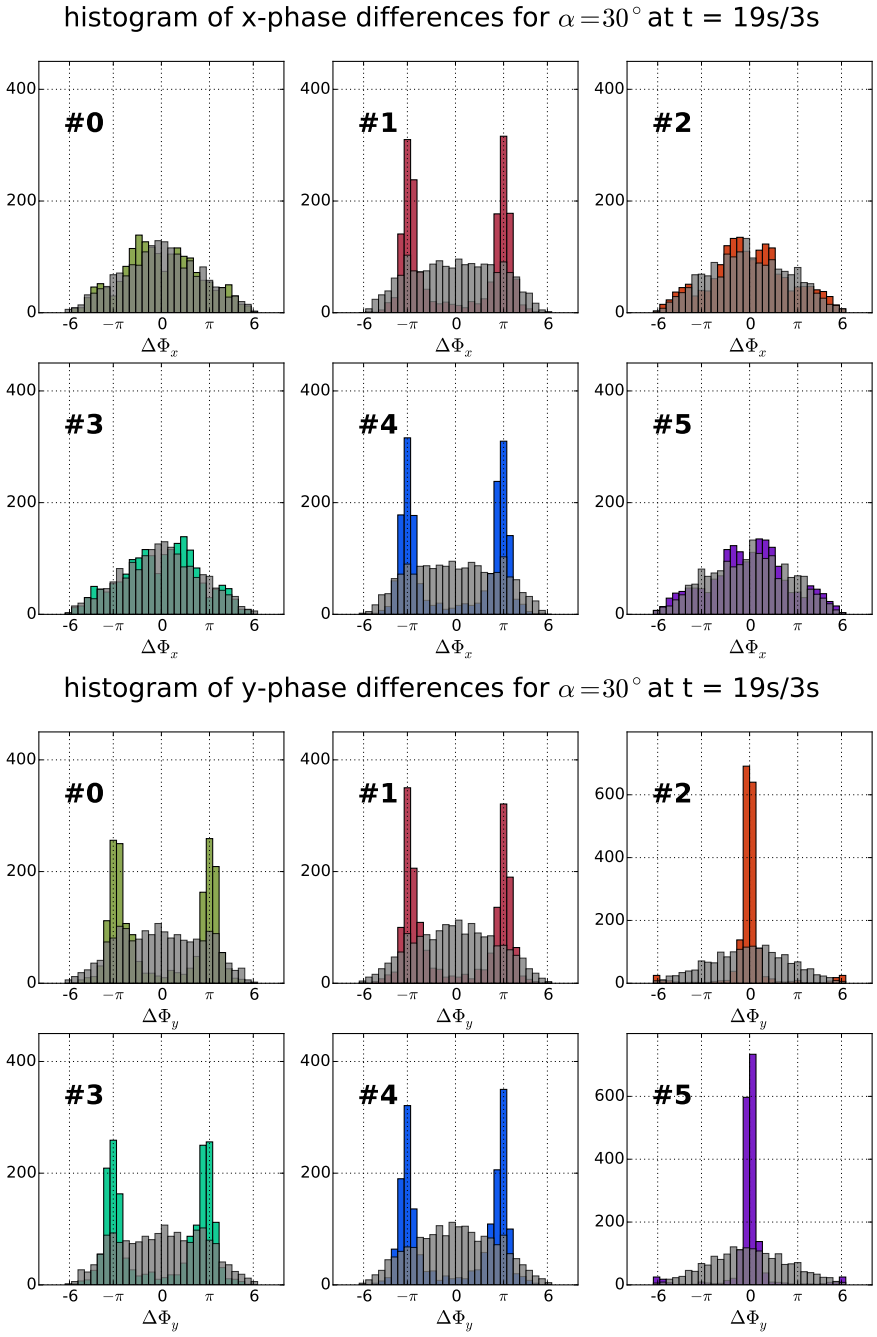

Figure 4.19: Phase distribution of the x-motion and y-motion for all next neighbours for $t_{sync} = 19s$ (colored) and $t = 3s$ (gray). The observed distributions are in good agreement with the assumption of dominating hybrid motion. For the y-phases the structure of a anti-phase stripe pattern is visible. For the x-phases the competition of two stripe directions leads to anti-phase peaks only for the neighbour indices (#1, #4) where both competing patterns induce the same phase difference.

4.6 Formation of Standing Waves

In the last part it was stated that the pattern of adjacent anti-phase stripes (i.e. a phase difference $\Delta\Phi = \pi$) can be explained by the formation of standing waves. In the following this is exemplified for the case $\alpha = 0°$. Since for this case there is only one hot spot pair the orientation of stripes is clearly defined. In that sense this situation can be seen as prototypical example. In a first step the appearance of standing waves is motivated followed by the verification of the occurrence in the simulations of the perfect crystal as well as in the reference simulations.

Motivation of Standing Wave Formation

As shown in Sec. 2.2.4 one may think about the crystal motion as linear superposition of all normal modes given as

$$\mathbf{d}(\mathbf{X}_i, t) = \sum_{\mathbf{k}\in 1.BZ} \sum_{s=1}^{3} |A_{s,\mathbf{k}}| \begin{pmatrix} |\epsilon^x_{s,\mathbf{k}}| \cos(\omega_{s,\mathbf{k}} t - \mathbf{k}\cdot\mathbf{X}_i - \beta^x_{s,\mathbf{k}})) \\ |\epsilon^y_{s,\mathbf{k}}| \cos(\omega_{s,\mathbf{k}} t - \mathbf{k}\cdot\mathbf{X}_i - \beta^y_{s,\mathbf{k}})) \\ |\epsilon^z_{s,\mathbf{k}}| \cos(\omega_{s,\mathbf{k}} t - \mathbf{k}\cdot\mathbf{X}_i - \beta^z_{s,\mathbf{k}})) \end{pmatrix} \exp(g_{s,\mathbf{k}} t) \tag{4.20}$$

Where $\boldsymbol{\epsilon}_{s,\mathbf{k}} = (\epsilon^x_{s,\mathbf{k}}, \epsilon^y_{s,\mathbf{k}}, \epsilon^z_{s,\mathbf{k}})^T = (|\epsilon_x| e^{i\gamma^x_{s,\mathbf{k}}}, |\epsilon^y_{s,\mathbf{k}}| e^{i\gamma^y_{s,\mathbf{k}}}, |\epsilon^z_{s,\mathbf{k}}| e^{i\gamma^z_{s,\mathbf{k}}})^T$ is the polarization vector and $A_{s,\mathbf{k}} = |A_{s,\mathbf{k}}| e^{i\alpha_{s,\mathbf{k}}}$ are complex constants dependent on the initial conditions. For convenience it was $\beta^{x/y/z}_{s,\mathbf{k}} = \gamma^{x/y/z}_{s,\mathbf{k}} + \alpha_{s,\mathbf{k}}$ defined.

For the case $\alpha = 0°$ we have one pair of hot spots with the two central wave vectors $\pm\mathbf{k}_{hyb}$ of both propagation directions of the hybrid mode. The corresponding growth rate and the hybrid frequency are denoted as $g_{hyb} = g_h$ and $\omega_{hyb} = \omega_h$. To avoid confusing notation this time only the subscript h instead of hyb is used. The central hybrid vectors in case $\alpha = 0°$ are parallel to the x-axis and can be written as $\pm\mathbf{k}_{hyb} = (k_x, k_y)^T = (\pm k_{hyb}, 0)^T$. Since the hybrid motion in the x,y-plane is typically parallel to $\mathbf{k}_{hyb}$ one can assume $|\epsilon^y_{s,\mathbf{k}}| = 0$ for the maximum growing mode corresponding to $\mathbf{k}_{hyb}$. With this in mind one can separate the particle motion into dominant motion of the maximum growing mode on the one hand and all other modes at the other hand denoted as noise $\mathbf{n}(t)$. Such that we can write

$$\mathbf{d}(\mathbf{X}_i, t) = \mathbf{n}(t) + \begin{pmatrix} a^x_+ \cos(\omega_h t - \Phi_{h,i} - \beta^x_+)) + a^x_- \cos(\omega_h t + \Phi_{h,i} - \beta^x_-) \\ 0 \\ a^z_+ \cos(\omega_h t - \Phi_{h,i} - \beta^z_+)) + a^z_- \cos(\omega_h t + \Phi_{h,i} - \beta^z_-) \end{pmatrix} \exp(g_h t) \tag{4.21}$$

$\Phi_{h,i} = \mathbf{k}_{hyb} \cdot \mathbf{X}_i$ is the position dependent phase shift of particle i. The resulting amplitude and constant phase shift for the two wave propagation directions $\pm\mathbf{k}_{hyb}$ are denoted as $a^{x/z}_{+/-}$ and $\beta^{x/z}_{+/-}$. Focusing on the x-component of $\mathbf{d}(\mathbf{X}_i, t) = \mathbf{d}_i(t) = (x_i(t), y_i(t), z_i(t))^T$ we

can rewrite[14] the sum of two cosine waves as

$$x_i(t) \propto 2a_+^x \cos(\omega_h t - \frac{\beta_+^x + \beta_-^x)}{2}) \cos(\Phi_{h,i} + \frac{\beta_+^x - \beta_-^x)}{2}) + (a_-^x - a_+^x) \cos(\omega_h t + \Phi_{h,i} - \beta_-^x) \quad (4.22)$$

The first part of the sum has the typical shape of a standing wave $d(x,t) \propto \cos(\omega t)\cos(kx)$ [9]. The second part represents a propagating wave $d(x,t) \propto \cos(\omega t) - kx)$. Obviously the character of the resulting oscillation is dominated by the first standing wave part if $(a_-^x \approx a_+^x)$. Since the two parameters reflect the amplitude of both wave propagation directions there seems to be no reason why one direction should be preferred such that one may assume $(a_-^x = a_+^x)$ what would correspond to the formation of a pure standing wave. The phase shifts $(\beta_+^x \pm \beta_-^x)/2$ are identical for each particle and cause no qualitative important effect. In that sense they may be neglected such that qualitative characteristics of the most dominating wave should be given by

$$x_i(t) \propto \cos(\omega_h t)\cos(\Phi_{h,i}) \quad (4.23)$$

This is a standing wave where locally each particle oscillates at the same hybrid frequency (ω_h) with the position dependent amplitude $a_i = \cos(\Phi_{i,h})$. In that sense all particles are perfectly phase synchronized showing the same phase $\phi_i(t) = \omega_h t$. The position dependent phase shift induced by the $\mathbf{k}_{hyb}$-vector $(\Phi_i = \mathbf{k}_{hyb} \cdot \mathbf{X}_i)$ has no influence on the time dependence it only affects the local amplitude. The only effect what can be interpreted as effect on $\phi_i(t)$ is a negative sign in amplitude what can be expressed as a phase shift of π.

$$x_i(t) \propto a_i \cos(\omega_h t) = -|a_i| \cos(\omega_h t) = |a_i| \cos(\omega_h t \pm \pi) \quad (4.24)$$

With the method used for phase calculation in this thesis (assuming a linear growth between two maxima of the local oscillation) one measures therefore the above described anti-phase relation for adjacent stripes of switched sign in amplitude. With this insight it should now be possible to explain the dominant anti-phase synchronization from the predicted phase shifts for $\alpha = 0°$. If we recapitulate for this situation particles of identical x-position should be perfectly in phase (i.e. $\Delta\Phi = 0$) and for two particles of adjacent stripes of identical x-position a phase difference $\Delta\Phi = \pm 2.59$ was predicted by $\mathbf{k}_{hyb}$.

[14] Using $\cos(\alpha) + \cos(\beta) = 2\cos((\alpha+\beta)/2)\cos((\alpha-\beta)/2)$[4].

Expected Characteristics

To exemplify the different characteristic of a propagating and a standing wave it was focused on hypothetical central particle with $X_0 = 0$. This particle has naturally no position dependent phase shift $\Phi_0 = k_{hyb} X_0 = 0$. It oscillates with the period $T = 2\pi/\omega_h$. For t_0^{max} it shall be reach the maximum positive value of oscillation, then for $t = T/4$ it reaches a point of zero elongation. Particles of neighbouring rows with same equilibrium x-position (X_i) have the phase shift $\Phi_i = 2.59 \times i$. For this situation we can compare the propagating wave $a(t, X_i) = \cos(\omega_h t - 2.59 \times i)$ and the standing wave $a(t, X_i) = \cos(\omega_h t)\cos(2.59 \times i)$. For the standing wave for $t = t_0^{max}$, independent on the particle index, all particles show a maximum of oscillation. Or in case of a negative amplitude a minimum. Likewise for $t = T/4$ all particles show zero elongation. For the propagating wave simultaneous occurrence of extrema for all particles is not given. In Figure 4.20 the typical characteristics for both situations is shown. Obviously the typical phase difference $\Delta\Phi = 2.59$ for $\alpha = 0°$ leads to approximately alternating signs of amplitude for a standing wave. This is evaluated by local phase calculation as anti-phase synchronization $\Delta\Phi = \pi$.

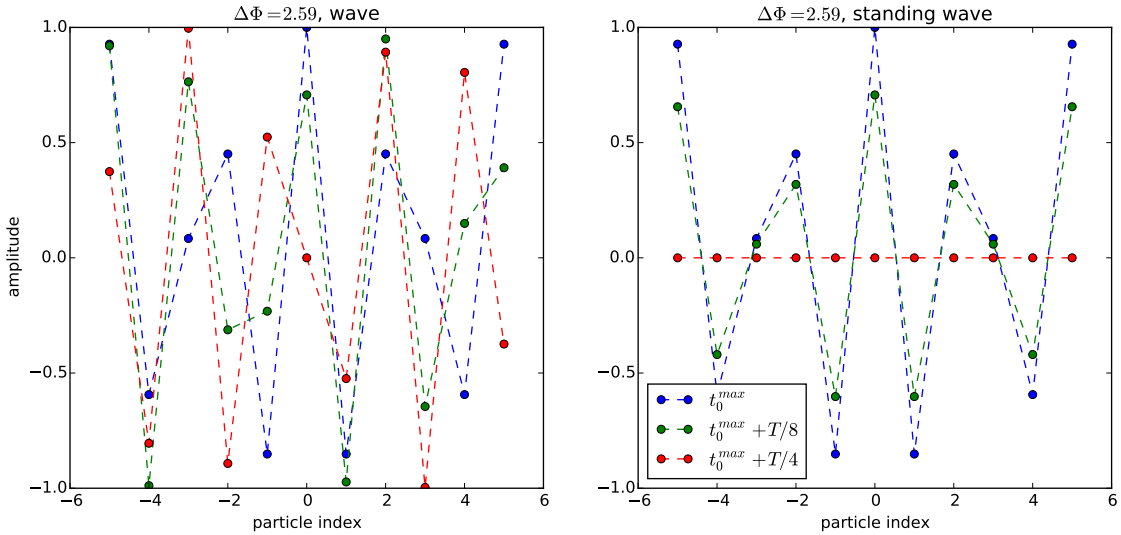

Figure 4.20: Typical characteristics of a standing wave and a propagating wave for the phase difference $\Delta\Phi = 2.59 \times i$. For t_0^{max} all particles of the standing wave show a extrema and approach zero elongation for $t = T/4$. For the propagating wave the extrema occur not such simultaneously. If evaluating the phases of oscillation locally the standing wave will produce a anti-phase pattern $\Delta\Phi = \pi$ instead of $\Delta\Phi = 2.59$.

Standing Waves in Simulations

To check if the typical characteristics of the standing wave formation can be found in the simulations it was focused on 1 dimensional rows picked out of the 2 dimensional synchronization area. An x-row contains all possible equilibrium x-positions of nearly identical y-position. An y-row contains all possible equilibrium y-positions for identical x-position. The chosen rows are shown in Figure 4.21

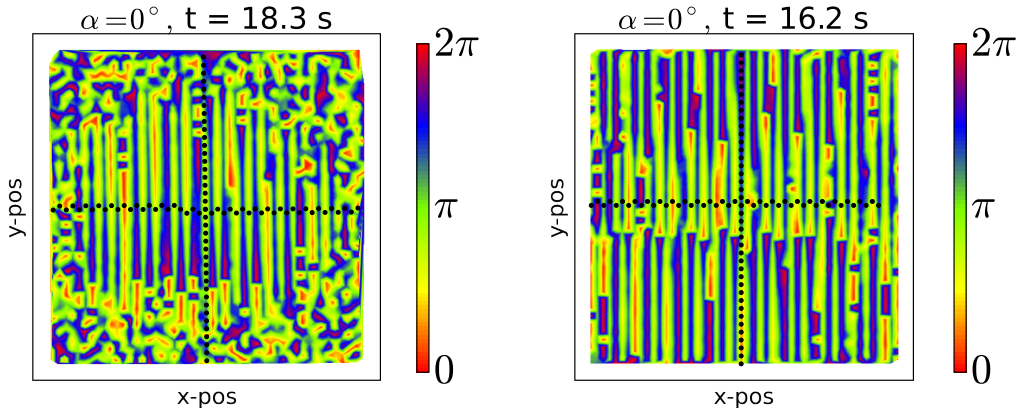

(i) reference simulations (ii) quadratic perfect crystal

Figure 4.21: Resulting phase patterns for the reference simulations and the nonlinear simulations of the perfect crystal for = 0°. To check for standing waves the x-rows and y-rows shown as black dots were used. The black dots indicate the equilibrium positions of the oscillating particles. The data of the reference simulations was evaluated with kind permission of I.Laut.

As shown in Sec. 4.4.3 for nonlinear interacting systems one may expect a drift of the positions additional to the oscillations. However the drift is slow on the velocity scale of the oscillations an therefore the velocity trajectories show nearly pure oscillatory character. In consequence it makes sense to look at the velocity wave pattern to identify the standing waves. To be exact $\dot{\mathbf{d}}(\mathbf{X}_i, t) = (v_x(\mathbf{X}_i, t), v_y(\mathbf{X}_i, t), v_z(\mathbf{X}_i, t),)$ was considered. Since the in plane hybrid motion is parallel to $\mathbf{k}_{hyb} = (k_x, 0)^T$ we can focus on the v_x component. The reference simulations was evaluated for $t \approx 18.3s$ and the nonlinear simulations of the perfect crystal for $t \approx 16.2s$. In any case for a central particle a time of maximum positive elongation (t_{max}) was found from visual inspection of the data. After that whole particle rows are plotted for the three times $\{t_{max}, t_{max} + T/8, t_{max} + T/4\}$. The period is known form the frequency evaluation. In case of $\alpha = 0°$ we have $\omega_{hyb} = 97.5/s$ and therefore $T = 2\pi/\omega_{hyb} = 0.0644s$. The results are shown in Figure 4.22. In the central region the typical standing wave characteristics of simultaneously occurring extrema is clearly dominant, what explains the peak in phase shift distributions for $\Delta\Phi = \pm\pi$.

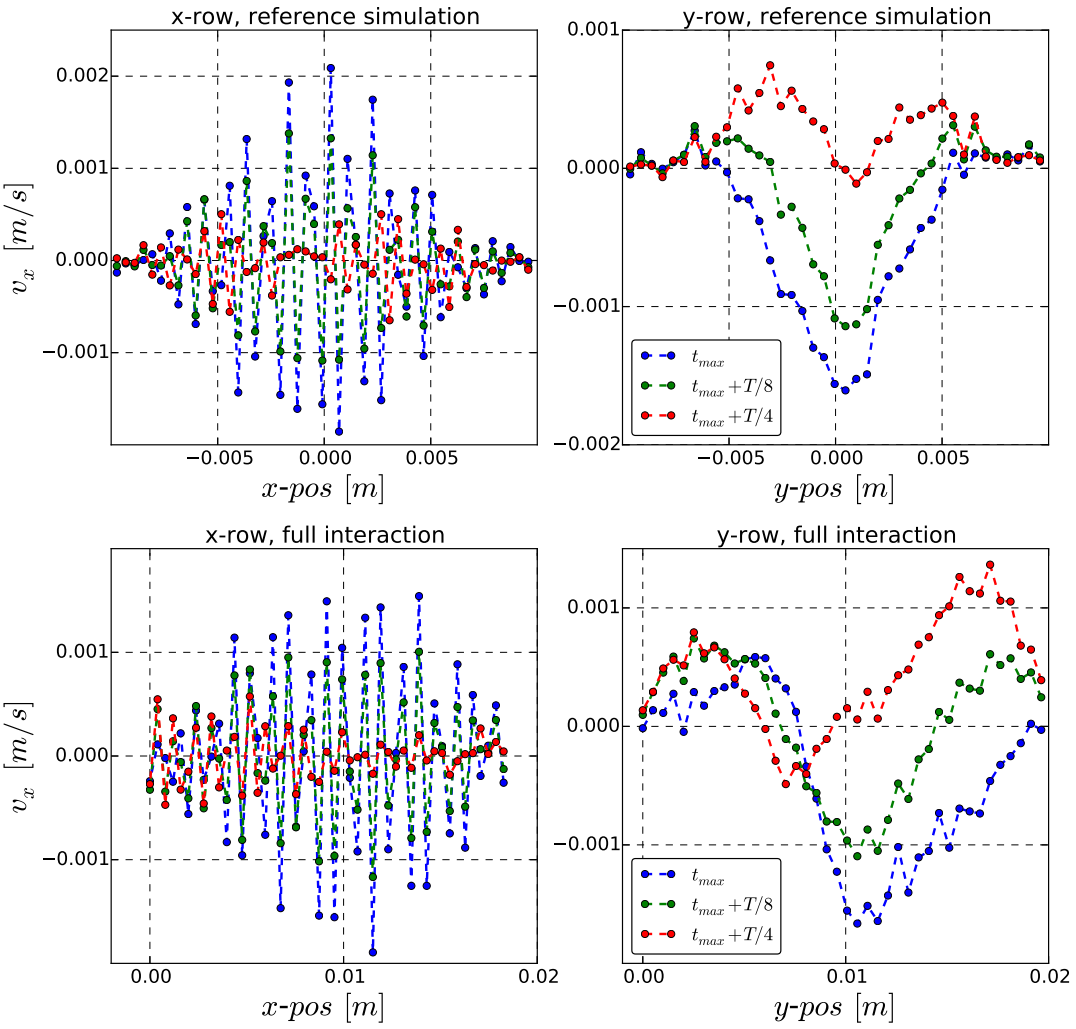

Figure 4.22: Formation of standing waves for the simulations. In any case t^{max} was chosen to be the time of maximal positive elongation for a central particle. The period is given by $T = 2\pi/\omega_{hyb} = 0.0644s$. With this information the elongation for all particles was plotted. Especially in the central region the typical standing wave characteristics of simultaneously occurring extrema is dominant. A pattern of in phase synchronization with mostly alternating amplitude signs develops. If evaluated in terms of phases, calculated from local oscillation, this can be interpreted as anti-phase pattern $\Delta\Phi = \pi$. The data of the reference simulations was evaluated with kind permission of I.Laut.

Chapter 5

Distinction to Nonlinear Synchronization Theory

As already mentioned, many synchronization phenomena are connected to a nonlinear theory of phase oscillators proposed by Y.Kuramoto in 1984 [17]. After the synchronization during mode-coupling instability was observed it was assumed to be also connected ([7], compare also Sec. 4.1) to this theory of "phase oscillators." However this theory describes nonlinear systems which synchronize. Since in the last parts it was shown that the synchronization during MCI is a purely linear phenomenon this seems not to be the case. In this chapter a short qualitative distinction of the observed synchronization to the theory of nonlinear phase oscillators is given.

5.1 Kuramoto Model

Probably the most common system of phase oscillators is a system investigated first by Y.Kuramoto in [17]. It is often denoted as "Kuramoto model" and given by

$$\frac{d\phi_\alpha}{dt} = \omega_\alpha - \frac{K}{N} \sum_{\alpha' \neq \alpha} sin(\phi_\alpha - \phi'_\alpha) \tag{5.1}$$

where ϕ_α is the phase of subsystem α, ω_α is the frequency of the uncoupled nonlinear oscillator and K is a constant determinig the coupling of the N subsystems. This model has proven to be very useful in many situations.

Significance of the Concept

The concept presented above has proven to be connected to real nonlinear synchronization phenomena in many situations. Following a view examples are given:

- In a paper published 1998 Wiesenfeld et al. [32] have shown that a series array of nonidentical Josephson junctions undergoes two synchronization transitions. Further

they showed that the in limit of weak coupling the system can be mapped onto the Kuramoto model (5.1) which predicts the transition points accurately.

- A second impressive example is the synchronization of metronomes which was already observed by Huygens during the 17th century [12]. Pantaleone published a paper in 2002 [23] where he has shown that the dynamics of N coupled metronomes in the limit of weak coupling can be reduced to a phase equation essentially given by the Kuramoto model (5.1). Also numerical simulations [31] have proven that coupled metronomes exhibit a so called Kuramoto transition predicted by (5.1) in the correct parameter regime of weak coupling. It should be mentioned here that metronomes are highly nonlinear oscillators due to their mechanisms ensuring a constant amplitude under energy consumption. In numerical and analytical treatments the individual subunits of metronomes can be modeled by Van-der-Pol oscillators[23, 20] which is one of the standard model systems of nonlinear oscillation satisfying a limit cycle solution.

In that sense it would be interesting if this synchronization theory would also be connected to the presented system.

5.2 Nonlinear Phase Oscillators

The exact definition of the phase for nonlinear phase oscillators is given in appendix B. Here only the qualitative idea is given. Phases in nonlinear synchronization theory are not always identical to the physical picture of sinusodial oscillations ($x(t) \propto \sin(\phi(t))$ where $\phi(t)$ is the time dependent phase).

In nonlinear synchronization theory synchronizing subunits show stable limit cycle solutions (see appendix B). This means that each subunit shows a stable periodic solution $\mathbf{X}(t) = \mathbf{X}(t+T)$ with period T. Stable means that if the system is disturbed it will come back on this limit cycle trajectory. This limit cycle property makes it possible to think about the subunits only moving on their limit cycles. With this picture the dynamic can be reduced to one single variable which parametrizes the limit cycle, the phase ϕ_α of subsystem α. In that sense nonlinear phase oscillators describe the interactions of complex nonlinear subsystem only by its position on the limit cycle.

This picture of synchronization is not given for the observed synchronization during MCI, presented in this thesis. Obviously the dynamic can not be reduced to a limit cycle. In that sense the concept of dominant synchronization by the most growing hybrid modes is clearly to distinguish from the nonlinear theory of phase oscillators.

Chapter 6

Conclusion

Lets recapitulate what we have found. It was shown that a linearized version of the interaction model exhibits the exact same synchronization patterns as the complete nonlinear interaction model. To be exact the nonlinear characteristics of the interaction even destroys the order. Such that we can conclude that the whole process can be interpreted using a linear description of the plasma crystal. This leads to the picture of dominating hybrid modes. It trivially explains the alignment of stripes with identical phases, since dominating plane waves inducing a constant phase shift orthogonal to the direction of wave propagation. The perfect frequency synchronization is explained by the fact that for the observed situation mode-coupling takes place for flat regions of the dispersion relation near the edges of the 1st Brillouin zone. This leads to approximately identical hybrid frequencies ($\omega = \omega_{hyb}$) for all hybrid modes with positive growth rate corresponding to the same hot spot pair. A superposition of growing oscillations with identical frequency (ω_{hyb}) leads trivially to a synchronized dominant motion with ω_{hyb}. Finally the observed anti-phase synchronization can be understood as formation of standing waves with nearly alternating sign of amplitude. This leads to a calculated phase shift of $\Delta\Phi = \pi$ for particles of opposite sign in amplitude since the local phase calculation neglects the varying magnitude in amplitude. In that sense all aspects of the synchronization are in perfect agreement with the predictions made from linear theory of the plasma crystal.

In case of reciprocal intearactions a synchronization for a linear system can be seen as not possible. Since a linear superposition of different solutions with comparable influence/amplitude for initial times, will be of comparable influence for all times. Consequently one may argue that nonlinearities are necessary to enable synchronized motion for reciprocal systems. However in case of noreciprocal interactions it is possible to obtain oscillations with exponential growing amplitudes. For this situation naturally the most growing solutions will dominate a linear superposition of different solutions for later times. To be exact, for the observed synchronization the mode-coupling instability provides an insight in the mechanism selecting dominant wave modes in terms of maximum growth rates.

Appendix A

Further Definitions

A.1 Bravais Lattice

The Bravais lattice is an infinite lattice of discrete points generated by the linear independent *primitive vectors* $\mathbf{a}_i\,,\ i = 1, 2, 3$ such that every point $\mathbf{x}$ of the Bravais lattice can be represented as $\mathbf{x} = \mathbf{a}_1 n_1 + \mathbf{a}_2 n_2 + \mathbf{a}_3 n_3$ where $n_i \in \mathbb{Z}$. It is perfectly symmetric in a sense that for any choice of $\mathbf{x}$ the surrounding lattice looks exactly the same. For more information the reference is made to standard solid state physics literature [2].

A.2 Reciprocal Lattice, Real-Space and K-Space

Identifying the points of a Bravais lattice with the positions of particles forming a crystal, this lattice is often denoted as *direct lattice* which lives in the *real-space*. This means that the lattice points denote locations in the real physical space. The *reciprocal lattice* is now the Fourier transform of the direct lattice which lives in the mathematical $\mathbf{k}$-*space*. The reciprocal lattice itself is again a Bravais lattice. For the 3 dimensional case defined through [2]

$$\mathbf{b}_1 = 2\pi \frac{\mathbf{a}_2 \times \mathbf{a}_3}{\mathbf{a}_1 \cdot (\mathbf{a}_2 \times \mathbf{a}_3)}\,,\ \mathbf{b}_2 = 2\pi \frac{\mathbf{a}_3 \times \mathbf{a}_1}{\mathbf{a}_2 \cdot (\mathbf{a}_3 \times \mathbf{a}_1)}\,,\ \mathbf{b}_3 = 2\pi \frac{\mathbf{a}_1 \times \mathbf{a}_2}{\mathbf{a}_3 \cdot (\mathbf{a}_1 \times \mathbf{a}_2)} \tag{A.1}$$

where $\mathbf{a}_1$, $\mathbf{a}_2$, $\mathbf{a}_3$ are the primitive basis vectors of the real space and $\mathbf{b}_1$, $\mathbf{b}_2$, $\mathbf{b}_3$ is the primitive basis of the reciprocal space.
For the 2 dimensional case the it reduces to the relation [34]

$$\mathbf{b}_1 = 2\pi \frac{\mathbf{R}\,\mathbf{a}_2}{\mathbf{a}_1 \cdot \mathbf{R}\,\mathbf{a}_2}\,,\ \mathbf{b}_2 = 2\pi \frac{\mathbf{R}\,\mathbf{a}_1}{\mathbf{a}_2 \cdot \mathbf{R}\,\mathbf{a}_1} \tag{A.2}$$

where $\mathbf{R}$ is a 90 degree rotation matrix. Obviously one has in any case the relation $\mathbf{a}_i \cdot \mathbf{b}_j = 2\pi\delta_{ij}$ where $\delta_{ij} = 1$ if $i = j$ and $\delta_{ij} = 0$ if $i \neq j$.

A.3 Plane Waves and 1st Brillouin Zone

If $\mathbf{d}(t, \mathbf{x})$ describes a filed of elongations $\mathbf{d}$ at the positions x, a plane wave is an oscillating elongation filed given as [9]

$$\mathbf{d}(t, x) \propto \mathrm{Re}(\exp(-i\omega t + i\mathbf{k} \cdot x)) = \cos(\omega t - \mathbf{k} \cdot x) \tag{A.3}$$

where ω describes the frequency of local oscillations at fixed positions x. The wave vector $\mathbf{k}$ characterizes the direction wave propagation. If defining $\Phi(t) = \omega t - \mathbf{k} \cdot \mathbf{x}$ as phase of the plane wave wee see that the a constant phase value travels according to

$$\frac{\mathbf{x}(t) \cdot \mathbf{k}}{|\mathbf{k}|} = \frac{\omega t - \Phi_{const}}{|\mathbf{k}|} \tag{A.4}$$

what shows that if ω and $\mathbf{k}$ have opposite sign the "plane" of constant phase is traveling in the direction of $\mathbf{k}$ and vice versa. In that sense a plane wave has a propagation direction.

The 1st Brillouin Zone

Describing plane waves on a (2 dimensional) Bravais lattice each possible position can be expressed as $\mathbf{X}_i = \mathbf{a}_1 n_1 + \mathbf{a}_2 n_2$ with $n_1, n_2 \in \mathbb{Z}$. The wave vector $\mathbf{k}$ of the plane wave may be expressed using the corresponding basis of the reciprocal $\mathbf{k}$-space according to $\mathbf{k} = \mathbf{b}_1 k_1 + \mathbf{b}_2 k_2$ where $k_1, k_2 \in \mathbb{R}$. Such that the phase of position $\mathbf{X}_i$ is given as $\Phi(\mathbf{X}_i) = 2\pi(n_1 k_1 + n_2 k_2)$. If we now replace the used vector $\mathbf{k}$ by $\mathbf{k} \to \mathbf{k} + \mathbf{K}$ with $\mathbf{K} = \mathbf{b}_1 l_1 + \mathbf{b}_2 l_2$ where $l_1, l_2 \in \mathbb{Z}$. The phase of position $\mathbf{X}_i$ changes only by a integral multiple of 2π. Consequently the resulting wave pattern is identical to the one induced by $\mathbf{k}$. In that way one can characterize all possible wave patterns already by a small part of the $\mathbf{k}$-space. The 1st Brillouin zone is the most common way of defining such an finite area characterizing all possible wave patterns. It is defined as first primitive Wigner Seitz cell of the reciprocal lattice [2].

A.4 Periodic Boundaries and Properties

A.4.1 Periodic Boundaries

To model a finite system, periodic boundaries can be introduced in the following way [2]. Given a 2 dimensional finite lattice consisting from the points

$$\{\mathbf{X}_{n_1,n_2} = n_1 \mathbf{a}_1 + n_2 \mathbf{a}_2 \mid n_1 \in \{0, ..., N_1 - 1\},\ n_2 \in \{0, ..., N_2 - 1\}\} \tag{A.5}$$

where $\mathbf{a}_1$, $\mathbf{a}_2$ are the primitive lattice vectors. Defining $\mathbf{L}_1 = N_1 \mathbf{a}_1$ and $\mathbf{L}_2 = N_2 \mathbf{a}_2$, periodic boundaries now demand $f(\mathbf{X}_{n_1,n_2}) = f(\mathbf{X}_{n_1,n_2} + \mathbf{L}_1) = f(\mathbf{X}_{n_1,n_2} + \mathbf{L}_2)$ for the position dependence of any solution.
For the plane wave ansatz, which solves the linearized lattice system, one has

$$\mathbf{d}(\mathbf{X}_{n_1,n_2}, t) \propto \exp(i\mathbf{k} \cdot \mathbf{X}_{n_1,n_2}) \tag{A.6}$$

this means that only $\mathbf{k}$-vectors are allowed which fulfill $\exp(i\mathbf{k}\cdot\mathbf{X}_{n_1,n_2})\exp(i\mathbf{k}\cdot\mathbf{L}_1) = \exp(i\mathbf{k}\cdot\mathbf{X}_{n_1,n_2})\exp(i\mathbf{k}\cdot\mathbf{L}_2) = \exp(i\mathbf{k}\cdot\mathbf{X}_{n_1,n_2})$. This is only true if

$$\mathbf{k}\cdot\mathbf{L}_1 = 2\pi m_1, \quad \mathbf{k}\cdot\mathbf{L}_2 = 2\pi m_2 \tag{A.7}$$

Using the corresponding primitive basis of the reciprocal space to express any allowed vector of the $\mathbf{k}$-space one can write $\mathbf{k} = k_1\mathbf{b}_1 + k_2\mathbf{b}_2$. Inserting this definition of $\mathbf{k}$ into Eq. A.7 one finds that allowed values for k_1, k_2 are given by $k_1 = m_1/N_1$ where $m_1 \in 0, 1, ..., N_1 - 1$ and $k_2 = m_2/N_2$ where $m_1 \in 0, 1, ..., N_2 - 1$ what leads to following allowed set of $\mathbf{k}$-vectors.

$$\left\{\mathbf{k}_{m_1,m_2} = \frac{m_1}{N_1}\mathbf{b}_1 + \frac{m_2}{N_2}\mathbf{b}_2 \mid m_1 \in \{0, ..., N_1 - 1\},\ m_2 \in \{0, ..., N_2 - 1\}\right\} \tag{A.8}$$

Therefore one has for a system of $N = N_1N_2$ particles always the same number of allowed $\mathbf{k}$-vectors.

A.4.2 Special Properties of the Periodic Solutions

From the spacial waves ($\propto \exp(i\mathbf{k}_{m_1,m_2}\cdot\mathbf{X})$) one can construct a orthogonal basis of the vector space $\mathbb{C}^N$ where $N = N_1N_2$. This is shown in the following.
If defining $l = n_1N_2 + n_2$ it is possible to list all positions of the lattice by one index l (i.e. $\mathbf{X}_{n_1,n_2} = \mathbf{X}_l$ where $l = n_1N_2 + n_2$). Now $\mathbf{v}_{m_1,m_2} \in \mathbb{C}^N$ shall be defined component wise by

$$[\mathbf{v}_{m_1,m_2}]_l = \exp(i\mathbf{k}_{m_1,m_2}\cdot\mathbf{X}_i) \tag{A.9}$$

with respect to the (standard) complex dot product[1] the different $\mathbf{v}_{m_1,m_2}$ are mutually orthogonal, i.e. $\mathbf{v}_{m_1,m_2}\cdot\overline{\mathbf{v}_{\hat{m}_1,\hat{m}_2}} = \delta_{m_1,\hat{m}_1}\delta_{m_2,\hat{m}_2}N$.
This can be seen by straightforward calculation

$$\begin{aligned}
\mathbf{v}_{m_1,m_2}\cdot\mathbf{v}_{\hat{m}_1,\hat{m}_2} &= \sum_{l=0}^{N-1}[\mathbf{v}_{m_1,m_2}]_l\overline{[\mathbf{v}_{\hat{m}_1,\hat{m}_2}]_l} \\
&= \sum_{l=0}^{N-1}\exp(i(\mathbf{k}_{m_1,m_2} - \mathbf{k}_{\hat{m}_1,\hat{m}_2})\cdot\mathbf{X}_l) \\
&= \sum_{n_1=0}^{N_1-1}\sum_{n_2=0}^{N_2-1}\exp(i(\frac{m_1-\hat{m}_1}{N_1})2\pi n_1)\exp(i(\frac{m_2-\hat{m}_2}{N_2})2\pi n_2) \\
&= \sum_{n_1=0}^{N_1-1}\left[\exp(i(\frac{m_1-\hat{m}_1}{N_1})2\pi)\right]^{n_1}\sum_{n_2=0}^{N_2-1}\left[\exp(i(\frac{m_2-\hat{m}_2}{N_2})2\pi)\right]^{n_2} \\
&= N_1\delta_{m_1,\hat{m}_1}N_2\delta_{m_2,\hat{m}_2} = N\delta_{m_1,\hat{m}_1}\delta_{m_2,\hat{m}_2}
\end{aligned} \tag{A.10}$$

[1]For two vectors $\mathbf{a}, \mathbf{b} \in \mathbb{C}^N$ the dot product is usually defined as $\sum_{s=1}^{N} a_s\overline{b_s}$. Where $\overline{b_s}$ is the complex conjugate of b_s [1]

The last step leading to the Kronecker deltas δ_{ij} can be understood by considering partial sum of the geometric row [1]

$$S_N = \sum_{l=0}^{N-1} (e^{iz})^l = \frac{(e^{iz})^N - 1}{e^{iz} - 1} \tag{A.11}$$

which is valid as long as $z \neq 2\pi n$, $n \in \mathbb{Z}$. Since we have $z = (m - \hat{m})2\pi/N$, $m, \hat{m} \in \mathbb{Z}$ we get automatically $S_N = 0$. And in case $m = \hat{m}$ we have $z = 0$ what simply gives $S_N = N$. This shows that the different $\mathbf{v}_{m_1,m_2}$ are orthogonal. And since there is a total number of N orthogonal vectors $\mathbf{v}_{m_1,m_2}$ we have basis of $\mathbb{C}^N$ [1].

With this information it is straight forward to define a discrete Fourier transform $\tilde{s}(\mathbf{k})$ for a discrete signal $s(\mathbf{X}_i)$ defined at all positions of the lattice $\mathbf{X}_i$. Such that we get the two valid relations

$$s(\mathbf{X}_i) = \sum_{\mathbf{k}} \tilde{s}(\mathbf{k}) \exp(i\mathbf{k}\mathbf{X}_i) \quad \text{and} \quad \tilde{s}(\mathbf{k}) = \frac{1}{N} \sum_{\mathbf{X}_i} s(\mathbf{X}_i) \exp(-i\mathbf{k}\mathbf{X}_i) \tag{A.12}$$

The sum over $\mathbf{k}$ runs over all allowed periodic boundary vectors $\mathbf{k}_{m_1,m_2}$. The sum over $\mathbf{X}_i$ includes all positions of the lattice.

Appendix B

Phase of Nonlinear Oscillations

B.1 Systems of Weakly Coupled Limit-Cycle-Oscillators

The concept of phase oscillators was supposed by Kuramoto in [17]. The definition of a phase oscillator is summarized in the following. However it is pointed out that everything is taken from [17].

B.1.1 Limit Cycle Oscillators and their Phase

Let each subunit be characterized by an n-dimensional system of ordinary differential equations

$$\frac{d\mathbf{X}}{dt} = \mathbf{F}(\mathbf{X}), \quad \mathbf{X} \in R^n, \ \mathbf{F} : R^n \to R^n \tag{B.1}$$

and let $\mathbf{X_0}(t)$ be a linearly stable T-periodic solution of this system such that

$$\frac{d\mathbf{X_0}}{dt} = \mathbf{F}(\mathbf{X_0}), \quad \mathbf{X_0}(t+T) = \mathbf{X_0}(t) \tag{B.2}$$

Let C denote the closed orbit corresponding to $\mathbf{X_0}(t)$ such that for all t, $\mathbf{X_0}(t) \in C \subset R^n$. Now lets define a scalar ϕ in such a way that motion on C produces a constant increase in ϕ or specifically,

$$\frac{d\phi(\mathbf{X})}{dt} = 1, \quad \mathbf{X} \in C \tag{B.3}$$

The quantity ϕ may be called phase and is only determined to an multiple integer of T. This definition of ϕ can now be extended to the region G which contains the direct neighborhood of C such that $C \subset G \subset R^n$. The domain of attraction of C is assumed to contain G inside. Now let P denote a point such that $P \in G$, $P \notin C$ and let Q denote a point lying on C. One may apply the definition of ϕ on C (B.3) to associate some value ϕ_Q to Q. We now sample two trajectories of the system (B.1) using P and Q as initial condition at $t = 0$ and denote the trajectories by $P(t)$, $Q(t)$. Then $P(t)$ will approach C as $t \to \infty$. If now $P(t)$ ends separated from $Q(t)$ on C we say that ϕ_P, i.e., the initial

phase of $P(t)$ differs from ϕ_Q, i.e., the initial phase of $Q(t)$. However if $P(t)$ and $Q(t)$ come infinitely close to each other as $t \to \infty$ we say that $\phi_P = \phi_Q$. In this way G is completely filled with a one-parameter family of hypersurfaces of constant phase, each which is (n-1) dimensional. It is obvious that each point of the trajectory $P(t)$ used as initial condition will be end on C infinitely close together with the initial condition $Q(t)$ what gives the relation $\phi_{P(t)} = \phi_{Q(t)}$ for all times t. This implies

$$\frac{d\phi(\mathbf{X})}{dt} = 1, \quad \mathbf{X} \in G \tag{B.4}$$

On the other hand, we have the obvious identity

$$\frac{d\phi(\mathbf{X})}{dt} = \nabla\phi \, \frac{d\mathbf{X}}{dt} \tag{B.5}$$

where ∇ denotes the gradient with respect to $\mathbf{X}$. Using now (B.4) together with (B.1) gives

$$1 = \nabla\phi \, \mathbf{F}(\mathbf{X}), \quad \mathbf{X} \in G \tag{B.6}$$

B.1.2 Weakly Coupled Limit Cycle Oscillators

Now lets consider a system of N coupled identical limit cycle oscillators given by

$$\frac{d\mathbf{X}_\alpha}{dt} = \mathbf{F}(\mathbf{X}_\alpha) + \sum_{\alpha' \neq \alpha} \mathbf{V}_{\alpha\alpha'}(\mathbf{X}_\alpha, \mathbf{X}_{\alpha'}), \qquad \alpha = 1, 2, ..., N \tag{B.7}$$

inserting (B.7) into (B.5) and using (B.6) gives a phase equation for the coupled system

$$\frac{d\phi_\alpha}{dt} = 1 + \sum_{\alpha' \neq \alpha} \nabla\phi_\alpha \mathbf{V}_{\alpha\alpha'}(\mathbf{X}_\alpha, \mathbf{X}_{\alpha'}) \tag{B.8}$$

which however still depends on the exact positions in phase space $\mathbf{X}_\alpha$. If one now assumes only weak coupling one could argue that the dynamic in phase space could be approximated to lowest order by the limit cycle solution $\mathbf{X} \to \mathbf{X}_0(\phi)$. What is well defined if one replaces $\mathbf{X}$ by the one point of the limit cycle C which is part of the corresponding hypersurface containing $\mathbf{X}$. What is important here is that this perturbation idea brings the phase equations into closed form given by

$$\frac{d\phi_\alpha}{dt} = 1 + \sum_{\alpha' \neq \alpha} \nabla\phi_\alpha \mathbf{V}_{\alpha\alpha'}(\phi_\alpha, \phi_{\alpha'}) = 1 + \sum_{\alpha' \neq \alpha} \Gamma_{\alpha\alpha'}(\phi_\alpha, \phi_{\alpha'}) \tag{B.9}$$

which now only depend on the one scalar phase variable per subunit. The general properties of the coupling term $\Gamma_{\alpha,\alpha'}$ are examined by Kuramoto in his book [17] and will be of no importance in this thesis.

Finally the connection to the famous *Kuramoto model* will briefly be given. If one assumes slightly different limit cycles what leads to a slightly different frequency of the uncoupled limit cycles ($1 \rightarrow \omega_\alpha$) [17] and assumes a coupling function $\Gamma_{\alpha\alpha'}(\phi_\alpha, \phi_{\alpha'}) = -\frac{K}{N} sin(\phi_\alpha - \phi'_\alpha)$, where K is an arbitrary real constant and N the number of interacting limit cycles, the resulting phase equations are given by

$$\frac{d\phi_\alpha}{dt} = \omega_\alpha - \frac{K}{N} \sum_{\alpha' \neq \alpha} sin(\phi_\alpha - \phi'_\alpha) \tag{B.10}$$

This is the *Kuramoto model* which can be solved analytically for the limit $N \rightarrow \infty$.

Bibliography

[1] T. Arens, F. Hettlich, C. Karpfinger, U. Kockelkorn, K. Lichtenegger und H. Stachel: *Mathematik*. Springer-Verlag, 2015.

[2] N.W. Ashcroft, N.D. Mermin und J. Gress: *Festkörperphysik*, Band 3. Oldenbourg, 2013.

[3] C.M. Bishop, *Machine Learning* **128** (2006).

[4] I.N. Bronstein und K.A. Semendjajew, *Auflage, Verlag Harri Deutsch, Thun und Frankfurt/Main* (1981).

[5] L. Couëdel, V. Nosenko, A. Ivlev, S. Zhdanov, H. Thomas und G. Morfill, *Physical review letters* **104** (2010), 195001.

[6] L. Couëdel, S. Zhdanov, A. Ivlev, V. Nosenko, H. Thomas und G. Morfill, *Physics of Plasmas (1994-present)* **18** (2011), 083707.

[7] L. Couëdel, S. Zhdanov, V. Nosenko, A.V. Ivlev, H.M. Thomas und G.E. Morfill, *Phys. Rev. E* **89** (2014), 053108.

[8] S. Danø, P.G. Sørensen und F. Hynne, *Nature* **402** (1999), 320.

[9] W. Demtröder. *Experimentalphysik 1–Mechanik und Wärme. 5. neu bearbeitete und aktualisierte Auflage*, 2008.

[10] Z. Donkó, G.J. Kalman und P. Hartmann, *Journal of Physics: Condensed Matter* **20** (2008), 413101.

[11] C. Gardiner: *Stochastic methods*. Springer Berlin, 2009.

[12] C. Hugenii, H. Oscilatorium und A.F. Muquet. *Parisiis, 1673, english translation: The pendulum clock*, 1986.

[13] A. Ivlev und G. Morfill, *Physical Review E* **63** (2000), 016409.

[14] A.V. Ivlev, J. Bartnick, M. Heinen, C.R. Du, V. Nosenko und H. Löwen, *Phys. Rev. X* **5** (2015), 011035.

[15] A.V. Ivlev, T.B. Röcker, L. Couëdel, V. Nosenko und C.R. Du, *Phys. Rev. E* **91** (2015), 063108.

[16] I.Z. Kiss, Y. Zhai und J.L. Hudson, *Science* **296** (2002), 1676.

[17] Y. Kuramoto: *Chemical Oscillations, Waves, and Turbulence*. Courier Corporation, 2003.

[18] L.D. Landau, A. Kosevich, L.P. Pitaevskii und E.M. Lifshitz: *Theory of elasticity*. Butterworth, 1986.

[19] I. Laut, C. Räth, S. Zhdanov, V. Nosenko, L. Couëdel und H.M. Thomas, *EPL (Europhysics Letters)* **110** (2015), 65001.

[20] E.A. Martens, S. Thutupalli, A. Fourrière und O. Hallatschek, *Proceedings of the National Academy of Sciences* **110** (2013), 10563.

[21] A. Melzer, V.A. Schweigert und A. Piel, *Phys. Rev. Lett.* **83** (1999), 3194.

[22] G.J. Niels und F. Oded, *Molecular Physics* **111** (2013), 983. Doi: 10.1080/00268976.2012.760055.

[23] J. Pantaleone, *American Journal of Physics* **70** (2002), 992.

[24] T. Röcker, L. Couëdel, S.K. Zhdanov, V. Nosenko, A. Ivlev, H. Thomas und G.E. Morfill, *EPL (Europhysics Letters)* **106** (2014), 45001.

[25] T.B. Röcker: *Mode-coupling regimes in 2D plasma crystals*. lmu, Dissertation, 2014.

[26] T.B. Röcker, A.V. Ivlev, S.K. Zhdanov und G.E. Morfill, *Phys. Rev. E* **89** (2014), 013104.

[27] J.W. Shuai und D.M. Durand, *Physics Letters A* **264** (1999), 289 .

[28] S.H. Strogatz, D.M. Abrams, A. McRobie, B. Eckhardt und E. Ott, *Nature* **438** (2005), 43.

[29] M. Thoma, M. Kretschmer, H. Rothermel, H. Thomas und G. Morfill, *American journal of physics* **73** (2005), 420.

[30] H. Thomas, G.E. Morfill, V. Demmel, J. Goree, B. Feuerbacher und D. Möhlmann, *Phys. Rev. Lett.* **73** (1994), 652.

[31] H. Ulrichs, A. Mann und U. Parlitz, *Chaos: An Interdisciplinary Journal of Nonlinear Science* **19** (2009), 043120.

[32] K. Wiesenfeld, P. Colet und S.H. Strogatz, *Phys. Rev. E* **57** (1998), 1563.

[33] Wikipedia. *Elliptical polarization — Wikipedia, The Free Encyclopedia*, 2016. [Online; accessed 29-September-2016].

[34] Wikipedia. *Reciprocal lattice — Wikipedia, The Free Encyclopedia*, 2016. [Online; accessed 11-September-2016].

[35] S. Zhdanov, A. Ivlev und G. Morfill, *Physics of Plasmas (1994-present)* **16** (2009), 083706.

Erklärung:

Hiermit erkläre ich, die vorliegende Arbeit selbständig verfasst zu haben und keine anderen als die in der Arbeit angegebenen Quellen und Hilfsmittel benutzt zu haben.

München, den 4.10.2016
Ort, Datum

Unterschrift